Ε Θ Ν Ι Κ Ο Μ Ε Τ Σ Ο Β Ι Ο Π Ο Λ Υ Τ Ε Χ Ν Ε Ι Ο
ΣΧΟΛΗ ΠΟΛΙΤΙΚΩΝ ΜΗΧΑΝΙΚΩΝ - ΤΟΜΕΑΣ ΓΕΩΤΕΧΝΙΚΗΣ
Ηρώων Πολυτεχνείου 9, Πολυτεχνειούπολη Ζωγράφου 157 80
Τηλ: 210 772 3780, Fax: 210 772 3428, e-mail: gbouck@central.ntua.gr
www.georgebouckovalas.com

ΠΡΑΞΗ:

«ΘΑΛΗΣ- ΕΜΠ: ΠΡΩΤΟΤΥΠΟΣ ΣΧΕΔΙΑΣΜΟΣ ΒΑΘΡΩΝ ΓΕΦΥΡΩΝ ΣΕ ΡΕΥΣΤΟΠΟΙΗΣΙΜΟ ΕΔΑΦΟΣ ΜΕ ΧΡΗΣΗ ΦΥΣΙΚΗΣ ΣΕΙΣΜΙΚΗΣ ΜΟΝΩΣΗΣ»

MIS 380043

Επιστημονικός Υπέυθυνος: Καθ. Γ. ΜΠΟΥΚΟΒΑΛΑΣ

ΔΡΑΣΗ 2

Ανάπτυξη Λογισμικού για την αριθμητική ανάλυση της συζευγμένης σεισμικής απόκρισης ρευστοποιημένου εδάφους-θεμελίου-βάθρου γέφυρας

ΠΑΡΑΔΟΤΕΑ:

Τεχνική Έκθεση Πεπραγμένων (Π1) & Λογισμικό (Π2)

Νοέμβριος 2012

Ευρωπαϊκή Ένωση
Ευρωπαϊκό Κοινωνικό Ταμείο
ΕΠΙΧΕΙΡΗΣΙΑΚΟ ΠΡΟΓΡΑΜΜΑ
ΕΚΠΑΙΔΕΥΣΗ ΚΑΙ ΔΙΑ ΒΙΟΥ ΜΑΘΗΣΗ
επένδυση στην κοινωνία της γνώσης
ΥΠΟΥΡΓΕΙΟ ΠΑΙΔΕΙΑΣ & ΘΡΗΣΚΕΥΜΑΤΩΝ, ΠΟΛΙΤΙΣΜΟΥ & ΑΘΛΗΤΙΣΜΟΥ
ΕΙΔΙΚΗ ΥΠΗΡΕΣΙΑ ΔΙΑΧΕΙΡΙΣΗΣ
ΕΣΠΑ 2007-2013
πρόγραμμα για την ανάπτυξη
ΕΥΡΩΠΑΪΚΟ ΚΟΙΝΩΝΙΚΟ ΤΑΜΕΙΟ
Με τη συγχρηματοδότηση της Ελλάδας και της Ευρωπαϊκής Ένωσης

Εκτενής Περίληψη

[Οι βιβλιογραφικές αναφορές καθώς και οι αναφορές σε Σχήματα και Πίνακες παραπέμπουν στην πλήρη Τεχνική Έκθεση η οποία ακολουθεί]

ΕΙΣΑΓΩΓΗ

Η παρούσα Τεχνική Έκθεση αποτελεί το **1ο Παραδοτέο (Π1)** του Ερευνητικού Προγράμματος με τίτλο:

ΘΑΛΗΣ-ΕΜΠ (MIS 380043)

Πρωτότυπο Σχεδιασμός Βάθρων Γεφυρών σε Ρευστοποιήσιμο Έδαφος με Φυσική Σεισμική Μόνωση

με Συντονιστή (Ερευνητικό Υπεύθυνο) τον **Γεώργιο Μπουκοβάλα** Καθηγητή ΕΜΠ.

Συγκεκριμένα, παρουσιάζονται τα αποτελέσματα της **Δράσης Δ2**, η οποία αποσκοπεί στην:

"*Ανάπτυξη λογισμικού για την αριθμητική ανάλυση της συζευγμένης απόκρισης Βάθρου - Θεμελίωσης - Ρευστοποιημένου Εδάφους*".

Στην παρούσα Τεχνική Έκθεση, επισυνάπτεται επιπλέον το **2ο Παραδοτέο (Π2)** του ερευνητικού προγράμματος, το οποίο συνίσταται στην υπο-ρουτίνα (σε γλώσσα προγραμματισμού C++) η οποία είναι απαραίτητη για την εφαρμογή της νέας αριθμητικής μεθοδολογίας, με την Μη Γραμμική Μέθοδο Πεπερασμένων Διαφορών.

ΙΣΤΟΡΙΚΟ

Η ποιοτικά και ποσοτικά ακριβής προσομοίωση της συμπεριφοράς επιφανειακών θεμελιώσεων υπό καθεστώς ρευστοποίησης απαιτεί την πραγματοποίηση πλήρως συζευγμένων αναλύσεων ενεργών τάσεων και ροής του νερού των πόρων, με χρήση ενός καταστατικού προσομοιώματος ικανού να προβλέψει τη συμπεριφορά άμμων υπό μονοτονική και ανακυκλική φόρτιση. Το προσομοίωμα που υιοθετήθηκε για το σκοπό αυτό, στο παρόν ερευνητικό πρόγραμμα, είναι το προσομοίωμα οριακής επιφάνειας που προτάθηκε από τους Papadimitriou et al. (1999, 2001, 2002), όπως αυτό τροποποιήθηκε από τους Andrianopoulos (2010a,b).

Το εν λόγω προσομοίωμα βασίζεται στη θεωρία γενικευμένης πλαστικότητας, ενώ διαθέτει μηδενική ελαστική περιοχή, με αποτέλεσμα οι παραμορφώσεις να είναι σε κάθε βήμα ελαστοπλαστικές. Σε ό,τι αφορά στις ελαστικές παραμορφώσεις, αρχικά υπολογίζεται το μέγιστο ελαστικό μέτρο διάτμησης G_{max}, σύμφωνα τον τύπο του Hardin (1978), και στη συνέχεια υπολογίζεται το απομειωμένο εφαπτομενικό μέτρο διάτμησης G, σύμφωνα με το υστερητικό προσομοίωμα Ramberg-Osgood (1943). Η χρήση του εν λόγω προσομοιώματος επιτρέπει την ακριβή προσομοίωση της απομείωσης του μέτρου διάτμησης και της αύξησης της υστερητικής απόσβεσης με την αυξανόμενη επιβαλλόμενη ανακυκλική διατμητική παραμόρφωση (π.χ. Vucetic & Dobry, 1991, Ishibashi & Zhang, 1993). Η προκύπτουσα μορφή της σχέσης διατμητικών τάσεων – διατμητικών παραμορφώσεων, και της αντίστοιχης απομείωσης του εφαπτομεντικού μέτρου διάτμησης, παρουσιάζονται στα Σχήματα 2.1 και 2.2 της πλήρους Τεχνικής Έκθεσης που ακολουθεί.

Σε ό,τι αφορά στις πλαστικές παραμορφώσεις, το μέτρο πλαστικότητας K_p δίνεται συναρτήσει της απόστασης της τρέχουσας εντατικής κατάστασης r, στο χώρο των αποκλινουσών τάσεων, από ενα συζυγές σημείο r^{IP}, πάνω σε μία επιφάνεια που ονομάζεται οριακή επιφάνεια. Για τη διεύθυνση των πλαστικών παραμορφώσεων, οι διατμητικές παραμορφώσεις ακολουθούν συζευγμένο νόμος ροής, ενώ οι ογκομετρικές παραμορφώσεις υπολογίζονται συναρτήσει της απόστασης του τρέχοντος τασικού σημείου από μία δεύτερη επιφάνεια, που ονομάζεται επιφάνεια διαστολικότητας. Τόσο η οριακή επιφάνεια, όσο και η επιφάνεια διαστολικότητας ορίζονται συναρτήσει της παραμέτρου κατάστασης ψ (Been & Jefferies, 1985), βάσει μίας τρίτης επιφάνειας, που ονομάζεται επιφάνεια κρίσιμης κατάστασης. Με τον τρόπο αυτό, ενσωματώντεται στο προσομοίωμα η Θεωρία Κρίσιμης Κατάστασης (Schofield & Wroth, 1968), που επιτρέπει την προσομοίωση της συμπεριφοράς εδαφών με διαφορετική αρχική κατάσταση (διαφορετική μέση ενεργό τάση και σχετική πυκνόητα), χρησιμοποιώντας τις ίδιες παραμέτρους.

Η μορφή των τριών επιφανειών του προσομοιώματος στο χώρο των τριαξονικών τάσεων p΄-q και στο επίπεδο π του λόγου αποκλινουσών τάσεων, παρουσιάζεται στα Σχήματα 2.3 και 2.5. Στο Σχήμα 2.5 παρουσιάζεται επίσης ο νόμος προβολής της τρέχουσας εντατικής κατάστασης r, στο συζυγές σημείο r^{IP} πάνω στην οριακή επιφάνεια. Όπως φαίνεται στο σχήμα, ο νόμος προβολής ορίζεται συναρτήσει της εντατικής κατάστασης r^{LR} στην τελευταία αντιστροφή φόρτισης.

Τέλος, στο πλαστικό μέτρο K_p εισάγεται, μέσω ενός εμπειρικού συντελεστή h_f, η επίδραση της εξέλιξης της δομής του εδαφικού στοιχείου. Η θεώρηση αυτή επιτρέπει την ακριβή προσομοίωση του ρυθμού αύξησης των υπερπιέσεων πόρων, σε ανακυκλική φόρτιση, μέχρι τη ρευστοποίηση.

ΑΡΙΘΜΗΤΙΚΗ ΜΕΘΟΔΟΛΟΓΙΑ

Το ανωτέρω καταστατικό προσομοίωμα είχε ενσωματωθεί στον κώδικα Πεπερασμένων Διαφορών FLAC από τους Andrianopoulos et al (2010a,b), χρησιμοποιώντας τη γλώσσα προγραμματισμού FISH. Το FLAC εφαρμόζει μία μη-πεπλεγμένη διαδικασία επίλυσης, η οποία συνοψίζεται στο Σχήμα 2.6. Παρά τη δυνατότητα του FLAC για την πραγματοποίηση πλήρως συζευγμένων δυναμικών αναλύσεων ενεργών τάσεων με ροή του υγρού των πόρων, η χρήση της ενσωματωμένης γλώσσας προγραμματισμού FISH συνεπάγεται υπερβολικά αυξημένο υπολογιστικό κόστος, με αποτέλεσμα η εφαρμογή της εν λόγω αριθμητικής μεθοδολογίας σε τρεις διαστάσεις να είναι πρακτικώς αδύνατη. Δεδομένης της τρισδιάστασης φύσης της συμπεριφοράς επιφανειακών θεμελιώσεων βάθρων γεφυρών επί ρευστοποιήσιμου εδάφους, ο αλγόριθμος ολοκλήρωσης του καταστατικού προσομοιώματος επαναπρογραμματίστηκε, στα πλαίσια του παρόντος ερευνητικού προγράμματος, χρησιμοποιώντας τη γλώσσα C++, με αποτέλεσμα τη μείωση του χρόνου των αναλύσεων σε περίπου 1/3 του αρχικού χρόνου. Εν συνεχεία, πραγματοποιήθηκε βελτιστοποίηση του κώδικα, περαιτέρω μειώνοντας το χρόνο ανάλυσης κατά 10%. Σημαντικό ρόλο σε αυτή τη διαδικασία είχε η βελτιστοποίηση του αλγορίθμου εφαρμογής του νόμου προβολής του προσομοιώματος και προσδιορισμού του συζυγούς σημείου στην οριακή επιφάνεια. Τέλος, ο αλγόριθμος επεκτάθηκε στις τρεις διαστάσεις και ενσωματώθηκε στον κώδικα FLAC3D.

Ιδιαίτερα σημαντική, για τον καθορισμό του τελικού χρόνου αναλύσεων, ήταν η επιλογή της μεθόδου ολοκλήρωσης των καταστατικών σχέσεων. Για το σκοπό αυτό, εξετάστηκαν τρεις διαφορετικοί αλγόριθμοι ολοκλήρωσης, και συγκεκριμένα η απλή ολοκλήρωση Euler, η τροποποιημένη ολοκλήρωση Euler και η τροποποιημένη ολοκλήρωση Euler με αυτόματη υποδιαίρεση του βήματος ολοκλήρωσης και έλεγχο σφάλματος, που προτάθηκε από τους Sloan et al (2001). Οι ανωτέρω αλγόριθμοι ολοκλήρωσης παρουσιάζονται γραφικά στα Σχήματα 2.9 έως 2.11.

Για την αξιολόγηση των μεθόδων αυτών, κατασκευάστηκαν, για τριαξονική φόρτιση και για απλή διάτμηση, οι ισοκαμπύλες σφάλματος που παρουσιάζονται στα Σχήματα 3.1 και 3.2, αντίστοιχα. Παρατηρήθηκε ότι η τροποποιημένη ολοκλήρωση Euler με αυτόματη υποδιαίρεση του βήματος ολοκλήρωσης και έλεγχο σφάλματος, επιτρέπει την ακριβή ολοκλήρωση των καταστατικών σχέσεων, ακόμη και για μεγάλα βήματα επιβαλλόμενων παραμορφώσεων. Παρόλα αυτά, διαπιστώθηκε ότι για μικρές επιβαλλόμενες παραμορφώσεις, ικανοποιητική ακρίβεια μπορεί να επιτευχθεί ακόμα και με απλή ολοκλήρωση Euler. Τελικά, υιοθετήθηκε ένα σύνθετο σχήμα ολοκλήρωσης, που χρησιμοποιεί απλή ολοκλήρωση Euler για μικρές επιβαλλόμενες παραμορφώσεις, ενώ για μεγαλύτερες παραμορφώσεις επιτρέπει την αυτόματη επιλογή μεταξύ της απλής ολοκλήρωσης Euler και του αυτόματου αλγορίθμου των Sloan et al, συναρτήσει της τοπικής μη-γραμμικότητας της σχέσης τάσεων παραμορφώσεων.

Για την αξιολόγηση του επιλεγμένου αλγορίθμου ολοκλήρωσης, εξετάστηκε η τασική όδευση του Σχήματος 3.5. Τα αποτελέσματα που προέκυψαν με την εφαρμογή των διαφόρων μεθόδων ολοκλήρωσης, για διαφορετικά βήματα επιβαλλόμενων παραμορφώσεων, παρουσιάζονται στα Σχήματα 3.6 και 3.7. Στα Σχήματα 3.8 και 3.9 παρουσιάζεται το σχετικό σφάλμα από την εφαρμογή του κάθε αλγόριθμου ολοκλήρωσης, ενώ οι αντίστοιχοι απαιτούμενοι υπολογιστικοί χρόνοι συνοψίζονται στον Πίνακα 3.3. Όπως φαίνεται στον πινακα αυτό, η μη εφαρμογή ελέγχου σφάλματος και αυτόματης υποδιαίρεσης του βήματος, επιτρέπει τη σημαντική μείωση του χρόνου ανάλυσης, αλλά οδηγεί σε σημαντικό σφάλμα, ειδικά στην περίπτωση μεγάλων επιβαλλόμενων παραμορφώσεων, και κυρίως στις περιοχές έντονα μη-γραμμικής συμπεριφοράς, όταν η εντατική κατάσταση πλησιάζει την επιφάνεια κρίσιμης κατάστασης. Παρόλα αυτά, ο προτεινόμενος αλγόριθμος επιτρέπει την αυτόματη επιλογή του σχήματος ολοκλήρωσης ανάλογα με το επιβαλλόμενο βήμα παραμόρφωσης και με την τοπική μη-γραμμικότητα, με αποτέλεσμα να παρέχει ικανοποιητική ακρίβεια, επιτυγχάνοντας παράλληλα μείωση του υπολογιστικού χρόνου έως και κατά 90%.

ΒΑΘΜΟΝΟΜΗΣΗ & ΑΞΙΟΛΟΓΗΣΗ

Οι παράμετροι του καταστατικού προσομοιώματος που υϊοθετήθηκε στο παρόν ερευνητικό πρόγραμμα, προσαρμόστηκαν στη συμπεριφορά της άμμου Nevada, της οποίας τα φυσικά χαρακτηριστικά συνοψίζονται στον Πίνακα 3.4, ενώ η

κοκκομετρική της διαβάθμιση παρουσιάζεται στο Σχήμα 3.10. Οι επιλεγμένες παράμετροι συνοψίζονται στον Πίνακα 3.5. Οι προβλέψεις του καταστατικού προσομοιώματος συγκρίνονται με τα αντίστοιχα πειραματικά αποτελέσματα στα Σχήματα 3.11 έως 3.20, σε όρους μέγιστου μέτρου διάτμησης, απομείωσης του μέτρου διάτμησης και αύξησης της ιξώδους απόσβεσης με το εύρος της επιβαλλόμενης ανακυκλικής διατμητικής παραμόρφωσης, ρυθμού ανάπτυξης υπερπιέσεων πόρων, και καμπυλών ρευστοποίησης, για διαφορετικά επίπεδα επιβαλλόμενης μέσης τάσης, και διαφορετικές σχετικές πυκνότητες.

Πέραν της αξιολόγησης των προβλέψεων του καταστατικού προσομοιώματος έναντι εργαστηριακών δοκιμών εδαφομηχανικής, η ακρίβεια της αριθμητικής μεθοδολογίας επαληθεύθηκε και σε επίπεδο προβλήματος συνοριακών συνθηκών, μέσω της προσομοίωσης του πειράματος φυγοκεντριστή #12, του ερευνητικού προγράμματος VELACS (Arulmoli et al., 1992, Arulanandan & Scott, 1994). Το συγκεκριμένο πείραμα έχει άμεση σχέση με το αντικείμενο του παρόντος ερευνητικού προγράμματος, καθώς αφορά στη σεισμική συμπεριφορά επιφανειακής θεμελίωσης, εδραζόμενης επί ρευστοποιήσιμου εδάφους, του οποίου υπέρκειται μη ρευστοποιήσιμη επιφανειακή στρώση. Η διάταξη του εν λόγω πειράματος φυγοκεντριστή παρουσιάζεται στο Σχήμα 3.21, ενώ τα αντίστοιχα αποτελέσματα παρουσιάζονται στα Σχήματα 3.22 έως 3.24, σε όρους χρονοϊστοριών επιταχύνσεων, λόγων υπερπιέσεων πόρων και δυναμικών καθιζήσεων του θεμελίου.

Για την επαλήθευση της ακρίβειας του αλγορίθμου σε δύο και τρεις διαστάσεις πραγματοποιήθηκαν τρεις διαφορετικές αναλύσεις. Αρχικά έγινε ανάλυση σε δύο διαστάσεις, με τον κώδικα FLAC, στη συνέχεια πραγματοποιήθηκε μία ισοδύναμη ανάλυση επίπεδης παραμόρφωσης με τον κώδικα FLAC3D και τέλος προσομοιώθηκε το πλήρες τρισδιάστατο πρόβλημα με τον κώδικα FLAC3D. Οι αντίστοιχοι κάνναβοι πεπερασμένων διαφορών που θεωρήθηκαν παρουσιάζονται στα Σχήματα 3.25 έως 3.27, ενώ οι αντίστοιχες αριθμητικές προβλέψεις συγκρίνονται με τα πειραματικά αποτελέσματα στα Σχήματα 3.29 έως 3.31. Όπως φαίνεται στα εν λόγω σχήματα, η αναπτυχθείσα αριθμητική μεθοδολογία επιτρέπει την ακριβή προσομοίωση της συμπεριφοράς επιφανειακών θεμελιώσεων υπό καθεστώς ρευστοποίησης, με ικανοποιητική ποιοτική και ποσοτική ακρίβεια.

NATIONAL TECHNICAL UNIVERSITY OF ATHENS
SCHOOL OF CIVIL ENGINEERING – GEOTECHNICAL DEPARTMENT
9 Iroon Polytechniou str., 15780, Zografou Campus, Zografou, Greece
Tel: +30 210 772 3780, Fax: +30 210 772 3428, e-mail: gbouck@central.ntua.gr
www.georgebouckovalas.com

PROJECT:

«THALIS-NTUA: INNOVATIVE DESIGN OF BRIDGE PIERS ON LIQUEFIABLE SOILS WITH THE USE OF NATURAL SEISMIC ISOLATION»

MIS: 380043

Coordinator: PROF. G. BOUCKOVALAS

WORK PACKAGE 2

Software development for the numerical analysis of the coupled liquefiable soil-foundation-bridge pier response

DELIVERABLES

Technical Report (D1) & Software (D2)

November 2012

European Union
European Social Fund
OPERATIONAL PROGRAMME EDUCATION AND LIFELONG LEARNING
investing in knowledge society
MINISTRY OF EDUCATION & RELIGIOUS AFFAIRS, CULTURE & SPORTS
MANAGING AUTHORITY
NSRF 2007-2013
programme for development
EUROPEAN SOCIAL FUND
Co-financed by Greece and the European Union

Table of contents

1. Introduction 3

2. Numerical methodology: Background & new developments 6

2.1. General 6

2.2. Constitutive model description 9

2.2.1. Elastic moduli 10

2.2.2. Plastic moduli 14

2.2.3. Model surfaces 15

2.2.4. Flow rule 21

2.2.5. Plastic hardening modulus 21

2.2.6. Stress increment and load reversal 24

2.3. FLAC & FLAC3D finite difference codes 25

2.3.1. The explicit finite difference method 26

2.3.2. The finite difference equations 27

2.3.3. Mixed discretization 28

2.3.4. Discrete-model form of the finite difference equations 30

2.3.5. Numerical stability 33

2.3.6. Fluid-mechanical interaction 35

2.3.7. User defined models 38

2.4. Integration scheme 42

2.4.1. Modified Euler integration scheme, with automatic substepping and error control 43

2.4.2. Simple integration schemes 48

2.4.3. Modified Euler integration scheme, without error-control and substepping 49

2.4.4. Single-step Euler integration scheme 51

2.4.5. Combined integration scheme 53

2.5. Mapping rule 57

2.5.1. Algorithm proposed by Andrianopoulos (2006) 58

2.5.2. Modified algorithm for the application of the model's mapping rule 59

2.6. Drift Correction 61

3. Numerical methodology: Evaluation of performance 63

3.1. General 63

3.2. Accuracy of integration schemes 64

3.3. Computational efficiency of integration algorithms 70

3.4. Model calibration 82

3.5. Application – verification in boundary value problems 95

3.5.1. Experiment Results 95

3.5.2. Numerical Simulation 100

4. References 110

Chapter 1

Introduction

This Technical Report constitutes **Final Deliverable 1** of the Research Project with title:

THALIS-NTUA (MIS 380043)

Innovative Design of Bridge Piers on Liquefiable Soils with the use of Natural Seismic Isolation

performed under the general coordination of Professor **George Bouckovalas** (Scientific Responsible).

Namely, it presents the actions taken and the associated results of **Work Package WP2**, which aims at:

"*Software development for the numerical analysis of coupled bridge pier-foundation-liquefied ground response*".

Attached to this Report is **Final Deliverable D2** of the aforementioned Research Project, which includes the subroutine (in programming language C++) required for the application of the constitutive soil model developed herein to numerical (Finite Element and Finite Difference) computation algorithms.

The **Scope of Work Package WP2**, has been described in the approved Research Proposal as follows:

"The numerical analyses of liquefied ground response will be performed with an advanced computer software that has been developed at the Foundation Engineering laboratory of NTUA during long time research sponsored by OSDP (1994-1996), NTUA (1996-1999 & 2002-2004) and GSRT (2004-2007). This software combines the non linear, dynamic Finite Difference analysis method with a new constitutive model

for liquefiable soils which is implemented to the commercial codes FLAC and FLAC 3D (Itasca, 2006) using the UDM (User Defined Model) option of these codes.

To comply with the project requirements, the aforementioned software will have to be upgraded as described below:

(a) *The accuracy of computations will be improved for problems where excess pore pressure dissipation and soil consolidation takes place concurrently with seismic shaking. In addition, the numerical integration algorithm of the constitutive model will be optimized with respect to the required computational effort so that the parametric investigation of actual 3D boundary value problems, such as the one treated herein, can be performed in reasonable time.*

(b) *The constitutive model parameters will be calibrated against results from conventional geotechnical investigations in order to promote the application of the new model in practice by experienced but not necessarily expert users.*

(c) *The upgraded software that will be used for the numerical analysis of liquefied ground response will be verified against experimental results from two (2) relevant centrifuge tests performed during the well known VELACS research project (Arurmoli et al., 1992, Prevost et al 1994, Manzari & Arulanandan 1994): (a) seismic response of horizontally layered, liquefiable ground, and (b) seismic response of a square footing on liquefiable ground covered by a silty crust."*

Work Tasks (a), (b) and (c) above have been successfully executed, as described in the following Chapters. In addition, a CD has been prepared, and attached at the end of the report, with the electronic version of the constitutive model in C++, a detailed Users' Manual for its calibration and implementation to the Finite Difference codes FLAC (version 5) and FLAC 3D (version 4), as well as sample input files for typical analyses of liquefied ground response.

Chapter 2

Numerical methodology: Background & new developments

2.1. General

The qualitatively and quantitatively accurate numerical simulation of the seismic behavior of shallow foundations in a liquefiable regime would not be possible with the simple constitutive models (i.e. Mohr-Coulomb, Finn) which are offered by most commercial finite element and finite difference codes today. However, these commercial codes provide useful features, such as the ability to perform coupled dynamic effective stress analysis with groundwater flow, discretization into complicated meshes and use of structural elements (beams, shells and cables) together with a user-friendly application environment. Furthermore, many of them also allow the implementation of user-defined models. Therefore, the most efficient way to perform such a rigorous numerical analysis is to implement a constitutive model, capable of predicting accurately the basic aspects of cyclic response of sands under variable cyclic shear strain amplitudes, into one of the currently available commercial codes.

The constitutive model selected in this work, is the one proposed by Papadimitriou et al. (1999, 2001, 2002), as it was consequently modified by Andrianopoulos (2010a,b). This model provides the following advantages:

- The incorporation of the Critical State theory of Soil Mechanics (CSSM) (Schofield & Wroth, 1968) and the association of shear behavior to the state parameter ψ (Been & Jefferies, 1985), which allows the simulation of the effect of initial state (relative density and mean effective stress) with a single set of model parameters.

- The Ramberg-Osgood formulation adopted for elastic strain increments, which can simulate the non-linear hysteretic behaviour of sands (decrease of shear modulus and increase of hysteretic damping with increasing cyclic shear strain), at low strain levels.
- The introduction of an empirical coefficient, which quantifies the effect of fabric evolution during shearing and thus allows the accurate modeling of the excess pore pressure buildup rate, towards liquefaction.
- The vanished elastic region, a modification introduced by Andrianopoulos (2010a,b) to the original model by Papadimitriou et al. (2001), which increases the efficiency of the integration scheme, since it eliminates the iterative procedures required to estimate the crossing point on the yield surface and to ensure the consistency condition.

This constitutive model has been successfully implemented into the Finite Difference Code FLAC by Andrianopoulos (2010a,b). The same computer program, together with its 3D version, namely FLAC3D is also used herein. The selection of the specific computer code was based on the following criteria:

- FLAC uses an explicit integration scheme, which makes it more efficient and robust for modeling highly nonlinear problems (Frydman and Burd, 1997).
- FLAC allows the performance of fully coupled groundwater flow and dynamic analysis.
- Many special features, such as grid adjustment to fit any shape and use of structural and interface elements, are contained in the code.
- Most importantly, FLAC allows the implementation of new, user-defined constitutive models (UDMs), written in C++ and compiled as dynamic link libraries (DLLs) that can be loaded when needed. With slight modifications, a UDM compiled for FLAC, may be also used in FLAC3D.
- The currently available version of FLAC3D incorporates a parallel processing feature, which improves the code's efficiency by 1.7 times. UDMs compiled with C++ integrate with this feature, without any special modifications.

Initially, the implementation of the constitutive model by Andrianopoulos (2006), was achieved using the built-in programming language FISH. Extensive verification

through comparison of the enhanced code's predictions to the experimental results of three different centrifuge tests from the VELACS project (Arulanandan et al., 1994), proved the model's qualitative and quantitative accuracy in the analysis of soil liquefaction problems. However, the high computational cost of these analyses made the algorithm's extension to rigorous 3-dimensional analyses practically impossible. Therefore, as part of this Thesis:

- The UDM was rewritten in C++ and compiled as a DLL file, reducing the analysis time to about 1/3.
- Optimization of the new code resulted in an additional reduction in analysis time, of the order of 10%.
- Function profiling of the C++ code showed that the algorithm adopted by Andrianopoulos (2006) with regard to the model's mapping rule was very time consuming. Therefore, this algorithm was simplified, without altering the model's accuracy.
- Less accurate, but simpler and time efficient integration schemes were tested and evaluated in both element level (using isoerror maps) and boundary value problems (performing a benchmark analysis), in order to draw conclusions for their range of application.
- An automatic algorithm was developed, that switches between different integration schemes, based on the local non-linearity of the stress-strain relationship.

In the rest of this Chapter, a thorough presentation is provided for the finally implemented constitutive model, the finite difference codes FLAC and FLAC3D, as well as the adopted integration scheme, with emphasis upon the modifications which were applied to enhance the efficiency of the numerical algorithm.

2.2. Constitutive model description

The numerical methodology presented herein uses the constitutive model originally proposed by Papadimitriou et al. (1999, 2001, 2002), and consequently modified by Andrianopoulos (2006). The model is built on the general framework of elastoplasticity. It was originally developed in the triaxial space (p,q) (Papadimitriou et al., 2001), though the following presentation focuses on its multiaxial generalization (Papadimitriou et al, 2001, Andrianopoulos, 2006), which will be also used for the implementation to the finite difference codes FLAC and FLAC3D.

Following the elastoplasticity formulation, the stress increment $\dot{\sigma}_{ij}$ is computed for any given strain increment $\dot{\varepsilon}_{ij}$, using the elastoplastic tangent modulus C^{ep}_{ijkl}:

$$\dot{\sigma}_{ij} = C^{ep}_{ijkl}\dot{\varepsilon}_{kl} \tag{2.1}$$

The elastoplastic modulus is a fourth order tensor:

$$C^{ep}_{ijkl} = C^{e}_{ijkl} - \frac{C^{e}_{ijmn}R_{mn}L_{pq}C^{e}_{pqkl}}{K_p + L_{ij}C^{e}_{ijkl}R_{kl}} \tag{2.2}$$

where:

C^{e}_{ijkl} the elastic stiffness modulus

R_{ij} the perpendicular to the plastic potential surface in the stress space

L_{ij} the perpendicular to the yield surface in the stress space

K_p the plastic hardening modulus

The expressions adopted for the above moduli and tensors will be presented in the following paragraphs.

In Soil Mechanics, it is common practice to decompose stresses into an isotropic (p) and a deviatoric (s_{ij}) component. This deconvolution is also used in the model presented herein, and the corresponding stress components are defined as:

$$\sigma_{ij} = s_{ij} + p\delta_{ij} \tag{2.3}$$

where $p = \frac{\sigma_{kk}}{3}$.

Of importance is also the deviatoric stress ratio, which is defined as:

$$r_{ij} = \frac{s_{ij}}{p} \tag{2.4}$$

Accordingly, strains may be also decomposed to volumetric (ε_{vol}) and deviatoric (e_{ij}) as follows:

$$\varepsilon_{ij} = e_{ij} + \frac{\varepsilon_{vol}}{3}\delta_{ij} \tag{2.5}$$

where $\varepsilon_{vol} = \varepsilon_{kk}$.

2.2.1. Elastic moduli

As previously mentioned, Andrianopoulos (2006) modified the original model by Papadimitriou et al. (2001), by incorporating a vanished yield surface. This modification eliminates the iterative procedures which are required in order to estimate the crossing point on the yield surface and ensure the consistency condition, thus increasing the efficiency of the integration algorithm. The absence of a purely elastic region does not imply that strain increments do not have an elastic part. On the contrary, the deconvolution of strain increments into an elastic and a plastic component continues to apply, so that the plastic component is always present, even for small strain amplitudes.

The elastic moduli used herein follow a hypo-elastic formulation, based on the well-established one-dimensional hysteretic model by Ramberg and Osgood (1943). This formulation allows the smooth decrease of the tangential shear modulus G_t from its maximum value G_{max}, and the consequent smooth increase of viscous damping, with increasing shear strain amplitude (e.g. Vucetic & Dobry, 1991, Ishibashi & Zhang, 1993).

According to isotropic elasticity, the elastic stiffness coefficient is given from Equation (2.6):

$$C^{e}_{ijkl} = G_t \left(\delta_{ik}\delta_{jl} + \delta_{il}\delta_{jk} + \frac{2\nu}{1-2\nu}\delta_{ij}\delta_{kl} \right) \tag{2.6}$$

where ν is the Poisson's ratio, which is assumed to be constant.

The maximum shear modulus G_{max} is given from the well-established Hardin (1978) formula:

$$G_{max} = \frac{Bp_a}{0.3+0.7e}\sqrt{\frac{p}{p_a}} \tag{2.7}$$

where:

B	model parameter
e	void ratio
p	isotropic stress
p_a	atmospheric pressure ($=98.1\text{kPa}$)

It must be stressed out that the value of parameter B differs for monotonic and for cyclic loading. This is due to the fact that the constitutive model presented herein does not predict plastic behavior when the deviatoric stress ratio r_{ij} remains constant. Therefore, for loading with constant r_{ij}, such as in one-dimensional consolidation, the value of parameter B must be adjusted to a smaller G_{max} value, corresponding to larger strain amplitudes.

The tangent shear modulus G_t used in Equation (2.6), is related to the maximum shear modulus G_{max} as:

$$G_t = G_{max} \diagup T \tag{2.8}$$

where T is a positive scalar (≥ 1) defined in Equation (2.9), which is used to express the reduction of the elastic shear modulus taking place as the current deviatoric stress ratio r_{ij} diverts from a reference ratio r^{ref}_{ij}. The expression of T is different for initial shearing ($\notin \text{LR}$) and subsequent load reversals ($\in \text{LR}$).

$$T=\begin{cases}1+2\left(\dfrac{1}{a_1}-1\right)\left(\dfrac{|X|}{2\eta_1}\right) & \in LR\\ 1+2\left(\dfrac{1}{a_1}-1\right)\left(\dfrac{|X|}{\eta_1}\right) & \notin LR\end{cases} \tag{2.9}$$

In the above equation, X is a scalar quantifying the variation of the current deviatoric stress ratio r_{ij} from the reference ratio r_{ij}^{ref}. The latter is defined as the deviatoric stress ratio corresponding to the point of load reversal, while for the first shearing, it is the initial stress ratio.

$$X=\sqrt{\frac{1}{2}\left(r_{ij}-r_{ij}^{ref}\right)\left(r_{ij}-r_{ij}^{ref}\right)} \tag{2.10}$$

Variable η_1 is defined as:

$$\eta_1=a_1\left(\frac{G_{max}^{LR}}{p^{LR}}\right)\gamma_1 \tag{2.11}$$

where:

G_{max}^{LR} the maximum shear modulus at last load reversal

p^{LR} the isotropic stress at last load reversal

a_1, γ_1 model parameters

To provide insight to the above formulation, one may assume pure shearing $\tau-\gamma$ conditions, so that $X=\left(\tau-\tau^{ref}\right)/p_o$. The elastic stress-strain relationship resulting from the specified formula in this simple case, is depicted in Figure 2.1. The variation of the secant shear modulus, normalized with the maximum shear modulus, is shown in Figure 2.2, as a function of the shear strain amplitude γ. As shown in both Figures, a_1 is the ratio of the secant shear modulus to the maximum shear modulus, for the characteristic shear strain value γ_1. More specifically, model parameter a_1 quantifies the non-linearity for small strain amplitudes, where plastic strains are minor. A decrease of a_1 leads to increased non-linearity, while for $a_1=1$ the behavior is linear. On the other hand, model parameter γ_1 may be interpreted as a threshold shear strain

beyond which any further degradation to the overall stiffness is due to the development of plastic strain.

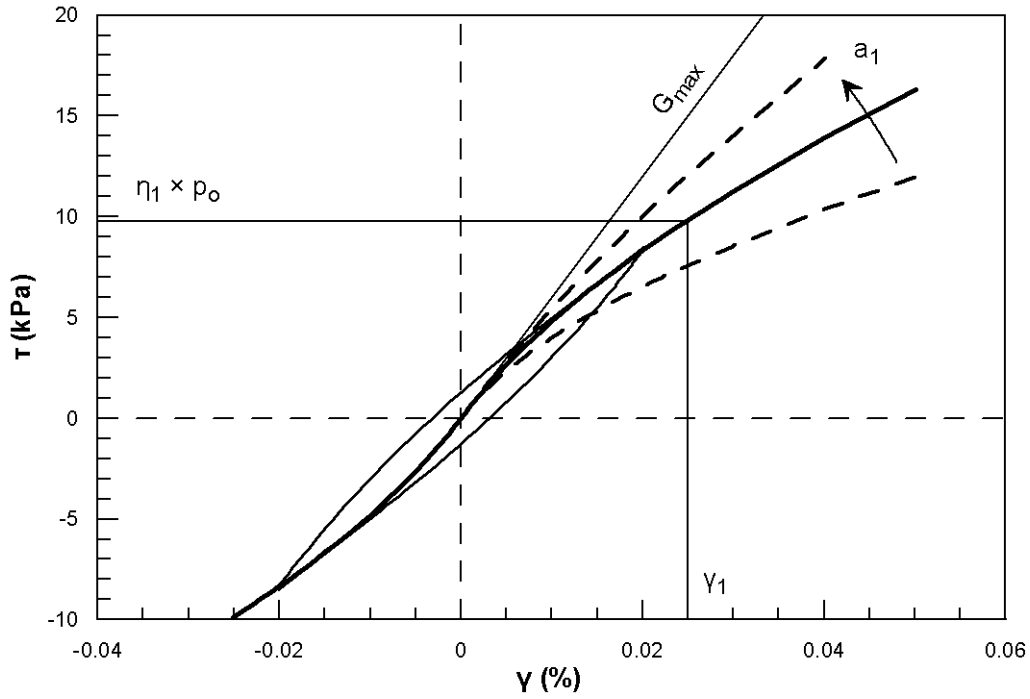

Figure 2.1. Exemplary pure shear stress-strain relation according to the Ramberg-Osgood formulation: shear reversal and effect of a_1.

Σχήμα 2.1. Τυπική σχέση διατμητικής τάσης-παραμόρφωσης σύμφωνα με το νόμο Ramberg-Osgood: αντιστροφή φόρτισης και επίδραση του a_1.

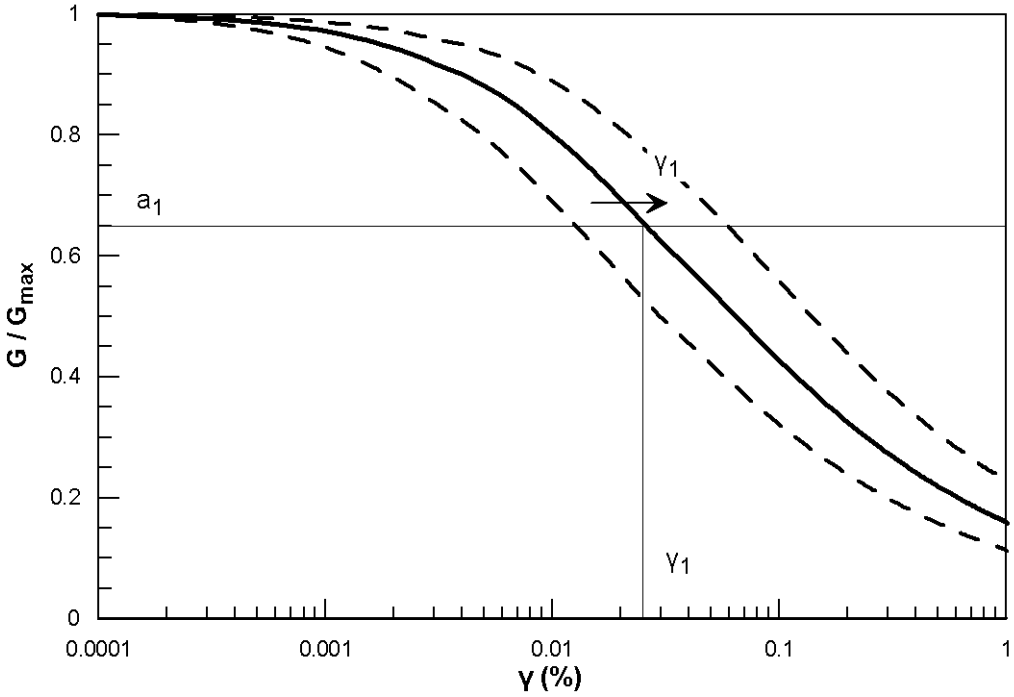

Figure 2.2. Exemplary shear modulus degradation with increasing shear strain, according to the Ramberg-Osgood formulation: effect of γ_1.

Σχήμα 2.2. Τυπική σχέση απομείωσης του μέτρου διάτμηση με αυξανόμενη διατμητική παραμόρφωση, σύμφωνα με το νόμο Ramberg-Osgood: επίδραση του γ_1.

2.2.2. Plastic moduli

According to the framework of classical elastoplasticity, the following functions need to be defined, in order to have a complete set of constitutive relations:

- An expression for the yield surface $f\left(\sigma_{ij}, q_n\right) = 0$, where q_n represent the model's internal variables.
- The gradient of the plastic potential surface $R_{ij} = dg\left(\sigma_{ij}, q_n\right) \Big/ d\sigma_{ij}$, which is multiplied by the loading index Λ to define the plastic strain increment $\dot{\varepsilon}_p = \left\langle \Lambda \right\rangle R_{ij}$.
- A rate equation $\dot{q}_n = \left\langle \Lambda \right\rangle \overline{q}_n$ which is necessary in order to define the evolution of the model's internal variables.

Combining the above functions with the kinematical assumption for the decomposition of total strain into elastic and plastic parts $\dot{\varepsilon}_{ij} = \dot{\varepsilon}^e_{ij} + \dot{\varepsilon}^p_{ij}$, the consistency

condition $f = \dot{f} = 0$ and the elasticity equation $\dot{\sigma}_{ij}^{e} = C_{ijkl}^{e}\dot{\varepsilon}_{kl}^{e}$, yields Equation (2.2) for the elastoplastic modulus C_{ijkl}^{ep}. However, as shown in Equation (2.2), in generalized plasticity, it suffices to define the gradients $L_{ij} = df\left(\sigma_{ij}, q_n\right)\big/ d\sigma_{ij}$ and $R_{ij} = dg\left(\sigma_{ij}, q_n\right)\big/ d\sigma_{ij}$, as well as the plastic modulus $K_p = -\dfrac{\partial f\left(\sigma_{ij}, q_n\right)}{\partial q_n}\bar{q}_n$. In the constitutive model used herein, L_{ij} and R_{ij} are defined as:

$$L_{ij} = \frac{\partial f}{\partial \sigma_{ij}} = n_{ij} - \frac{V}{3}\delta_{ij} = n_{ij} - \frac{n_{kl}r_{kl}}{3}\delta_{ij} \tag{2.12}$$

$$R_{ij} = \frac{\partial g}{\partial \sigma_{ij}} = n_{ij} + \frac{D}{3}\delta_{ij} \tag{2.13}$$

where V and D are scalar variables, and n_{ij} is a unit vector, which will be defined in the following paragraphs. It should be stressed that $D \neq -V$, implying that the model incorporates a non-associated flow rule.

2.2.3. Model surfaces

The adopted constitutive model belongs to the family of bounding surface models, where the plasticity equations are defined with the aid of two surfaces in the stress space, namely the Bounding Surface and the Dilatancy Surface. In order to incorporate the Critical State Theory of Soil Mechanics, the state parameter ψ (Been & Jefferies, 1985) is used to correlate the above to a third surface, namely the Critical State Surface. All three surfaces have the shape of a cone, with their apex at the origin of the stress space.

In the triaxial stress space $p' = \frac{1}{3}\left(\sigma'_{11} + 2\sigma'_{33}\right)$, $q = \sigma'_{11} - \sigma'_{33}$ the surfaces are defined as shown in Figure 2.3, using the deviatoric stress ratios M_c for compression and M_e for extension. More specifically, M_c^c, M_c^b and M_c^d are used for the critical state surface, the bounding surface and the dilatancy surface, respectively, for triaxial compression, while, for triaxial extension, the respective stress ratios are M_e^c, M_e^b and M_e^d.

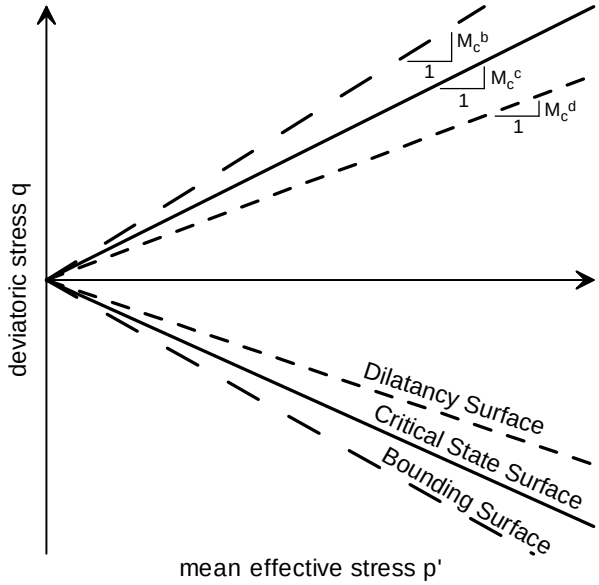

Figure 2.3. Projection of model surfaces on the triaxial stress space p'-q.

Σχήμα 2.3. Προβολή των επιφανειών του προσομοιώματος στον χώρο των τριαξονικών τάσεων p'-q.

The full description of the conical shape of the surfaces in the multiaxial stress space, requires the definition of the surfaces' shape on the π-plane, i.e. the plane in the r_1, r_2, r_3 space which is perpendicular to the hydrostatic axis ($r_1 = r_2 = r_3$). The Lode angle θ, defined in Equation (2.14), is used for this purpose (Figures 2.4 and 2.5).

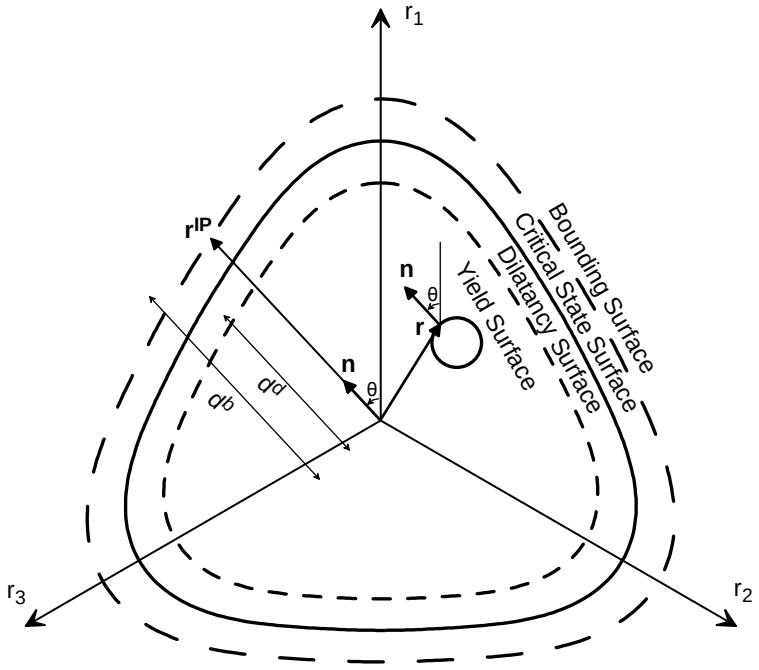

Figure 2.4. Projection of model surfaces on the π-plane – Mapping rule adopted by Papadimitriou et al (2002).

Σχήμα 2.4. Προβολή των επιφανειών του προσομοιώματος στο επίπεδο π – Νόμος προβολής σύμφωνα με Papadimitriou et al (2002).

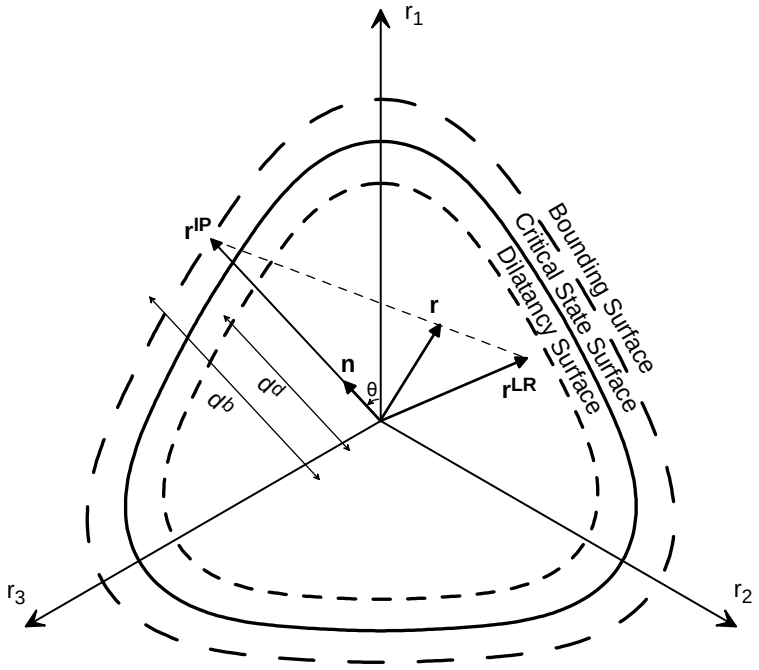

Figure 2.5. Projection of model surfaces on the π-plane – Mapping rule adopted by Andrianopoulos (2006).

Σχήμα 2.5. Προβολή των επιφανειών του προσομοιώματος στο επίπεδο π – Νόμος προβολής σύμφωνα με Andrianopoulos (2006).

Namely, this angle corresponds to the direction of the deviatoric stress ratio r_{ij} and ranges between 0° and 60°, where 0° corresponds to triaxial compression and 60° corresponds to triaxial extension. Intermediate values refer to non-triaxial loading.

$$\cos(3\theta) = \frac{3\sqrt{3}}{2}\frac{J_3}{J_2^{3/2}} \tag{2.14}$$

where:

$J_2 = \frac{1}{2}(r_{ij}r_{ij})$ the second invariant of r_{ij}

$J_3 = \frac{1}{3}(r_{ij}r_{ij}r_{ij})$ the third invariant of r_{ij}

Incorporating the effect of the Lode angle, the generally non-circular shape of the model surfaces on the π-plane is given by Equation (2.15):

$$M_\theta^c = g(\theta, c^c) M_c^c \tag{2.15}$$

where:

$$c^c = \frac{M_e^c}{M_c^c} \tag{2.16}$$

$$g(\theta, c^c) = \frac{2c^c}{\frac{1+c^c}{2} - \frac{1-c^c}{2}\cos(3\theta)} - \left[\frac{1+c^c}{2} + \frac{1-c^c}{2}\cos(3\theta)\right] \tag{2.17}$$

As described in the above, both the Bounding and Dilatancy Surfaces are correlated to the Critical State Surface, through the critical state parameter ψ (Been & Jefferies, 1985), defined as:

$$\psi = e - e_{cs} \tag{2.18}$$

where e_{cs} is the void ratio at Critical State, for an average stress equal to p. In the $e - \ln p$ space, the Critical State Surface is assumed to have the form of a straight line, described as:

$$e_{cs} = \left(e_{cs}\right)_a - \lambda \ln\left(\frac{p}{p_a}\right) \tag{2.19}$$

where:

p_a atmospheric pressure ($= 98.1\text{kPa}$)

$\left(e_{cs}\right)_a$ void ratio at critical state, for $p = p_a$

λ slope of Critical State Line (CSL) in the $e - \ln p$ space

It becomes clear that the state parameter ψ combines the effect of soil density (through the void ratio e) and the average consolidation (effective) pressure p (through e_{cs}). Positive ψ values ($\psi \geq 0$) imply contractive behavior and $\phi_{max} = \phi_{cs}$, while negative ψ values ($\psi < 0$) indicate dilative behavior and $\phi_{max} > \phi_{cs}$. This is incorporated into the model through Equations (2.20) to (2.23):

$$M_c^b = M_c^c + k_c^b \left\langle -\psi \right\rangle \tag{2.20}$$

$$M_e^b = M_e^c + k_e^b \left\langle -\psi \right\rangle \tag{2.21}$$

$$M_c^d = M_c^c + k_c^d \psi \tag{2.22}$$

$$M_e^d = M_e^c + k_e^d \psi \tag{2.23}$$

where M_c^c, M_e^c, k_c^b, k_e^b, k_c^d, k_e^d are user defined model parameters.

The deviatoric stress ratios M_c^c and M_e^c are related to the friction angles at Critical State $\phi_{cs,c}$ and $\phi_{cs,e}$ (for triaxial compression and extension, respectively), as:

$$M_c^c = \frac{6\sin\left(\phi_{cs,c}\right)}{3 - \sin\left(\phi_{cs,c}\right)} \tag{2.24}$$

$$M_e^c = \frac{6\sin\left(\phi_{cs,e}\right)}{3 + \sin\left(\phi_{cs,e}\right)} \tag{2.25}$$

while k_e^b and k_e^d can be computed by the following simplified expressions:

$$k_e^b = \frac{M_e^c}{M_c^c} k_c^b \tag{2.26}$$

$$k_e^d = \frac{M_e^c}{M_c^c} k_c^d \tag{2.27}$$

In order to incorporate the model surfaces in the constitutive equations, an image point r_{ij}^{IP} must be defined on each surface, and its distance from the current deviatoric stress ratio r_{ij} must be computed. In the original model presented by Papadimitriou et al. (2002), this was achieved using the unit deviatoric stress ratio tensor n_{ij}, which is normal to the yield surface at the current crossing point, as shown in Figure 2.4. The model adopted herein, presented by Andrianopoulos (2006) has a vanished yield surface, and therefore the unit vector n_{ij} must be defined otherwise. Andrianopoulos (2006) studied how various mapping rules affect the simulated sand response and concluded to the one schematically presented in Figure 2.5. Namely, the image point r_{ij}^{IP} is located on the bounding surface, as the projection along the $\left(r_{ij} - r_{ij}^{LR}\right)$ direction, where r_{ij} is the current deviatoric stress ratio, and r_{ij}^{LR} is the deviatoric stress ratio at load reversal. This mapping rule has the advantage of taking into account the recent shear stress history. However, it must be stressed that a perturbation of r_{ij} leads to the definition of a new r_{ij}^{LR}, which may affect the simulated soil behavior. Finally, the unit vector n_{ij} is computed as:

$$n_{ij} = \frac{r_{ij}^{IP}}{\sqrt{r_{kl}^{IP} r_{kl}^{IP}}} \tag{2.28}$$

Given the unit vector n_{ij}, the image points on the model surfaces may be computed using Equation (2.29), while their scalar distances from the current state r_{ij} may be computed using Equation (2.30). Positive $d^{c,b,d}$ values imply that the current state is inside the corresponding surface, while for negative values, it is outside.

$$r_{ij}^{IP,c,b,d} = \sqrt{\frac{2}{3}} M_\theta^{c,b,d} n_{ij} \tag{2.29}$$

$$d^{c,b,d} = \left(r_{ij}^{IP,c,b,d} - r_{ij} \right) n_{ij} \tag{2.30}$$

Both the interpolation rule and flow rule of the adopted constitutive model are functions of the above scalar distances, normalized against two reference distances, namely d_{ref}^{b} and d_{ref}^{d}, defined as:

$$d_{ref}^{b,d} = \sqrt{\frac{2}{3}} \left(M_{\theta}^{b,d} + M_{\theta+\pi}^{b,d} \right) \tag{2.31}$$

2.2.4. Flow rule

Having defined the unit vector n_{ij}, the gradient of the yield surface may be readily computed using Equation (2.12). However, in order to compute the direction R_{ij} of plastic strain increment (Equation (2.13)), the variable D must also be defined. This is expressed as a function of the scalar distance from the dilatancy surface, using the following expression:

$$D = A_o d^d \left(2.0 - \sqrt{\frac{\langle d^d \rangle}{d_{ref}^{d}}} \right) \tag{2.32}$$

where:

A_o non-dimensional model parameter

Note that the value of D affects only the volumetric component of plastic strains. Moreover, Equations (2.30) and (2.32) imply that positive volumetric strain (i.e. contraction) will occur when the current deviatoric stress ratio is inside the dilatancy surface, whereas dilative behavior will be simulated if loading continues beyond the dilatancy surface. In this sense, the dilatancy surface closely corresponds to the phase transformation line of Ishihara et al (1975).

2.2.5. Plastic hardening modulus

In order to have a complete set of constitutive equations, the plastic hardening modulus K_p remains to be defined. This modulus is related to the scalar distance d^b from the image point on the bounding surface, through the expression:

$$K_p = p h_b h_f d^b \tag{2.33}$$

where:

- p average stress, giving units to K_p
- h_b positive scalar, used to define the interpolation rule to the model's bounding surface
- h_f positive scalar, used to quantify the effect of fabric change
- d^b distance from the bounding surface

All parameters in Equation (2.33) are positive valued, except from d^b, which essentially controls the sign of K_p, thus differentiating hardening and softening behavior. More specifically, when the current deviatoric stress ratio lies inside the bounding surface, $d^b > 0$ and hardening occurs. When the bounding surface is crossed, then $d^b < 0$ and the post-peak strain softening behavior of dilative soils is simulated.

The interpolation rule used in the adopted constitutive model is described as:

$$h_b = h_o \frac{\left|d^b\right|^3}{\left\langle d^b_{ref} - \left|d^b\right| \right\rangle} \tag{2.34}$$

where h_o is a non-dimensional model parameter.

This expression of h_b was presented by Andrianopoulos (2006), and is different than the one originally proposed form by Papadimitriou et al (2002), where the quantity $\left|d^b\right|$ in the nominator was not raised to the 3rd power. This modification became necessary after the adoption of a vanished yield surface. The plastic modulus K_p resulting from this new expression, takes larger values when the current stress ratio r_{ij} is not far from the last shear reversal, while its reduction as the stress ratio r_{ij} moves closer to the bounding surface, is highly non-linear.

The fabric evolution is assumed to merely affect the plastic strain rates, and is introduced to the expression for the plastic modulus K_p through an empirical factor h_f, expressed as:

$$h_f = \frac{1 + \langle f_p \rangle}{1 + \langle f_{ij} n_{ij} \rangle} \tag{2.35}$$

According to Equation (2.35), the value of h_f is a function of the scalar variable f_p and the tensor f_{ij}, which take initial values equal to zero, and evolve as plastic volumetric strains accumulate, i.e.:

$$\dot{f}_p = H\dot{\varepsilon}^p_{vol} \tag{2.36}$$

$$\dot{f}_{ij} = -H\langle -\dot{\varepsilon}^p_{vol} \rangle \left(C n_{ij} + f_{ij} \right) \tag{2.37}$$

where:

$$C = 4 \max \left| f_p \right|^2 \tag{2.38}$$

$$H = H_o \left(\frac{\sigma_{1,o}}{p_a} \right) \langle -\psi_o \rangle \tag{2.39}$$

In Equation (2.39):

- $\sigma_{1,o}$ is the maximum principal stress at the initial state of consolidation
- ψ_o is the value of the state parameter ψ at the initial state of consolidation
- p_a is the atmospheric pressure
- H_o is a positive non-dimensional model parameter

According to Equation (2.36), f_p follows the whole shearing history of the sand. Therefore, when the shearing path remains under the phase transformation line, it simulates the continuously stiffening unloading-reloading behavior (Ladd et al, 1977, Seed et al, 1977), by increasing the nominator of h_f and thus the plastic modulus K_p.

On the other hand, according to Equation (2.37), f_{ij} develops only during dilation, and in the opposite sense relative to tensor $\left(C n_{ij} + f_{ij} \right)$, so that both $\left(C n_{ij} + f_{ij} \right)$ and $\dot{f}_{ij}$ will asymptotically tend to zero, until a potential load reversal will change the direction of n_{ij}. However, during this dilative shear path, the denominator of h_f remains equal to 1, because f_{ij} develops in the opposite sense of n_{ij} and thus $\langle f_{ij} n_{ij} \rangle = 0$. The

denominator becomes larger than 1 , only after a load reversal that follows a dilative path, and maintains its value until the next load reversal, or until tensor f_{ij} starts developing towards a different direction. This increase of the h_f denominator simulates the compliant unloading paths, observed after successive shearing cycles of larger amplitude (Ishihara et al, 1975, Ladd et al, 1977, Nemat-Nasser et al, 1982).

2.2.6. Stress increment and load reversal

Finally, in order to define a load reversal, the consistency condition is considered, and Equation (2.1) is rearranged as follows:

$$\dot{\sigma}_{ij} = C^{e}_{ijkl}\dot{\varepsilon}_{ij} - \langle \Lambda \rangle C^{e}_{ijmn} R_{mn} \tag{2.40}$$

where Λ is the loading index, defined in Equation (2.41):

$$\Lambda = \frac{L_{ij}\dot{\sigma}_{ij}}{K_p} \tag{2.41}$$

For the specific constitutive model, the above equations may be simplified as follows:

$$\dot{\sigma}_{ij} = 2G_t\dot{e}_{ij} + K_t\dot{\varepsilon}_{vol}\delta_{ij} - \langle \Lambda \rangle \left(2G_t n_{ij} + K_t D\delta_{ij} \right) \tag{2.42}$$

$$\Lambda = \frac{2G_t n_{ij}\dot{e}_{ij} - VK_t\dot{\varepsilon}_{vol}}{K_p + 2G_t - VK_t D} \tag{2.43}$$

The above expressions allow the distinction of three cases:

$\Lambda > 0$ Loading occurs and plastic strains accumulate.

$\Lambda = 0$ Neutral loading occurs and plastic strains are equal to zero.

$\Lambda < 0$ Unloading occurs. In this case, a load reversal point is defined, and the reference state r^{LR}_{ij} is reassigned. Therefore, the negative value of the loading index Λ is only instant, as the reassignment of the reference state yields a positive value for Λ .

2.3. FLAC & FLAC3D finite difference codes

The above presented constitutive model was implemented into the commercial codes FLAC and FLAC3D, using the program's option for User Defined Models (UDM). FLAC (standing for Fast Lagrangian Analysis of Continua) is an explicit finite difference program for geotechnical engineering mechanics computation. Materials are represented by elements, or zones, which form a grid that is adjusted by the user to fit the shape of the object to be modeled. Each element behaves according to a prescribed linear or nonlinear stress/strain law, in response to the applied forces or boundary restraints. The selection of the specific computer code for the purposes of this thesis was based on a number of available special features, including the following:

- FLAC offers the capability of performing dynamic effective stress analyses, together with fully coupled groundwater flow, thus satisfying the basic requirement for the numerical modeling of liquefaction related problems.
- A new feature added to the currently available version of FLAC 5 is the capacity to add user-defined constitutive models written in C++ and compiled as dynamic link libraries (DLLs). In all previous versions, the implementation of UDMs was made through the built-in programming language FISH. The main advantage of this modification is improved efficiency: UDMs compiled with C++ may perform 3 times faster than the ones written in FISH. Moreover, only slight modifications are needed for the UDM to be used in FLAC3D.
- FLAC also allows the use of interface elements to simulate distinct planes along which slip and/or separation can occur, as well as structural elements to simulate structural support. Therefore, the enhanced code may be used for the analysis of the most complicated liquefaction related problems.
- Finally, FLAC contains the powerful built-in programming language FISH, which allows the user to write his own functions and extend FLAC's pre- and post-processing capabilities. This feature may be used to define boundary conditions (such as tied nodes) for the dynamic analyses, as well as to manipulate the analyses output (i.e. create time histories and contours of excess pore pressures and excess pore pressure ratios).

2.3.1. The explicit finite difference method

The Finite Element Method has a central requirement, namely that the field quantities (stresses and displacements) vary throughout each element in a prescribed fashion, using specific functions controlled by nodal parameters. The formulation involves the adjustment of these parameters to minimize energy terms. In contrast, in the Finite Difference Method, every derivative in the set of governing equations is replaced directly by an algebraic expression written in terms of the field variables (stress, displacement) at discrete points in space, while these variables are not defined within elements.

Therefore, even for the solution of static problems, the dynamic equations of motion are the ones included in the formulation, using the general calculation sequence illustrated in Figure 2.6. This procedure first invokes the equations of motion to derive new velocities and displacements from stresses and forces. Then, strain rates are derived from velocities, and new stresses from strain rates. Each full cycle of this loop is taken as one timestep.

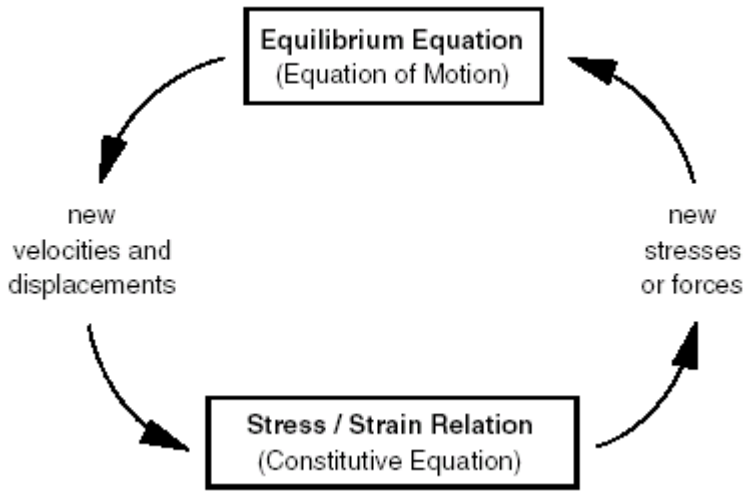

Figure 2.6. Explicit calculation sequence used in FLAC.

Σχήμα 2.6. Μη πεπλεγμένη διαδικασία υπολογισμού που χρησιμοποιείται στον κώδικα FLAC.

The most important characteristic of the explicit finite difference method is that each box in Figure 2.6 updates all of its grid variables (stresses or displacements) from known values that remain fixed while control is within the box. For example, the new

stresses computed in the lower box are based on the set of velocities which has been already calculated, and is assumed to be "frozen" for the operation of the box. This could be unreasonable, since a local stress change should influence the neighboring nodes and change their velocities. In order to justify this "frozen velocities" assumption, the integration timestep must be adequately small, so that information cannot physically pass from one element to another during that interval. This timestep value is dependant on the maximum speed at which information can propagate within each material, i.e. the pressure wave velocity, as well as the size of elements used. Of course, after several cycles of the loop, disturbances can propagate across several elements, just as they would propagate physically.

The most important advantage of the explicit finite difference method is that no iteration process is necessary when computing stresses from strains in an element, even if the constitutive law is highly nonlinear. In implicit methods, which are commonly used in finite element programs, every element communicates with every other element during one solution step, and therefore numerous iterations must be performed in order to obtain compatibility and equilibrium. It becomes obvious that the disadvantage of the explicit method is the small timestep required, and the consequently large number of computation steps, which makes the method inefficient for the modeling of linear, small-strain problems. However, it is more suitable for ill-behaved systems, where nonlinear constitutive laws, large-strain effects and physical instabilities become important. Therefore, in the case of the highly non-linear liquefaction related problems, FLAC is expected to perform better than most implicit finite element methods.

2.3.2. The finite difference equations

The first set of equations of dynamic equilibrium is the generalized Newton's law of motion for a continuous solid body, which is expressed as:

$$\rho \frac{\partial \dot{u}_i}{\partial t} = \frac{\partial \sigma_{ij}}{\partial x_j} + \rho g_i \qquad (2.44)$$

where:

t	time
x_i	coordinate vector

ρ mass density

g_i gravitational acceleration

$\dot{u}_i$ velocity vector

σ_{ij} stress tensor

The other set of equations is the constitutive relation, or stress/strain law, which has the following form:

$$\dot{\sigma}_{ij} = M\left(\sigma_{ij}, \dot{\varepsilon}_{ij}, q_n\right) \tag{2.45}$$

where:

$M(\ )$ is the functional form of the constitutive law,

$\dot{\varepsilon}_{ij}$ represents strain rates and

q_n are history parameters depending on the particular law.

The strain rate $\dot{\varepsilon}_{ij}$ is derived from velocity gradients as:

$$\dot{\varepsilon}_{ij} = \frac{1}{2}\left(\frac{\partial \dot{u}_i}{\partial x_j} + \frac{\partial \dot{u}_j}{\partial x_i}\right) \tag{2.46}$$

2.3.3. Mixed discretization

In order to solve the system of the above equations, the continuous medium is replaced by a discrete one, where velocities and forces are assumed to be concentrated on the nodes of a grid (or mesh). Therefore, the laws of motion for the continuum are transformed into discrete forms of Newton's law at the nodes. The spatial derivatives of velocities and forces (i.e. strain rates and stresses) are assumed to be constant within the zones (or elements) defined by the nodes mentioned above.

In FLAC, the finite difference mesh is composed of quadrilateral elements, which are internally subdivided into two overlaid sets of constant-strain triangular elements, as shown in Figure 2.7. The use of triangular elements eliminates problems which may occur with the deformational patterns of constant-strain finite difference quadrilaterals. More specifically, for polygons with more than three nodes, combinations of nodal displacements exist which produce no strain and may result in no opposing forces. To overcome this problem, the isotropic stress and strain

components are taken to be constant and are averaged over the whole quadrilateral element, while the deviatoric components are maintained and treated independently for each triangular sub-element. This procedure, referred to as mixed discretization, is described by Marti and Cundall (1982). The term mixed discretization arises from the different discretizations for the isotropic and deviatoric parts of the stress and stain tensors.

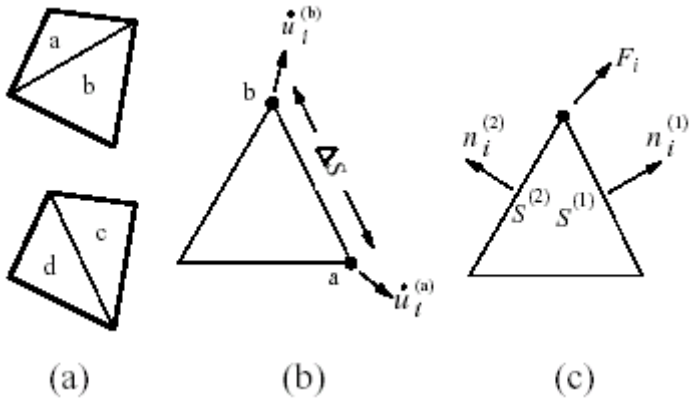

Figure 2.7. (a) Overlaid quadrilateral elements used in FLAC, (b) typical triangular element with velocity vectors and (c) typical triangular element with force vectors and unit normal vectors to the element's surfaces.

Σχήμα 2.7. (a) Επικαλυπτόμενα τετραπλευρικά στοιχεία που χρησιμοποιούνται στον κώδικα FLAC, (b) διανύσματα ταχύτητας στους κόμβους τυπικού τριγωνικού στοιχείου και (c) διανύσματα δυνάμεων στους κόμβους και μοναδιαία διανύσματα κάθετα στις πλευρές τυπικού τριγωνικού στοιχείου.

A mixed discretization technique is also used in FLAC3D. More specifically, the continuum is discretized into tetrahedra, which have the advantage of not generating hourglass deformations (i.e., deformation patterns created by combinations of nodal velocities producing no strain-rate and, thus, no nodal force increments). Similarly to FLAC, a coarser discretization in zones is superposed to the tetrahedral discretization (Figure 2.8). Isotropic stresses and volumetric strains in a zone are evaluated as the volumetric-average value over all tetrahedra in the zone, while the deviatoric components are manipulated independently.

It must be noted that one brick element in FLAC3D contains 2 overlays of 5 sub-zones each, and therefore model computations are performed 10 times per zone and per cycle, thus increasing the computational cost by 2.5 times, compared to the 4 sub-

zones of the 2-dimensional quadrilateral elements of FLAC. Moreover, in FLAC3D, all 6 stress components need to be computed, while in the plane strain conditions of FLAC, only 4 components are required. Finally, taking into account the increased number of elements required to perform a full 3-dimensional analysis, the importance of the computational efficiency of the User Defined Model's code is realized.

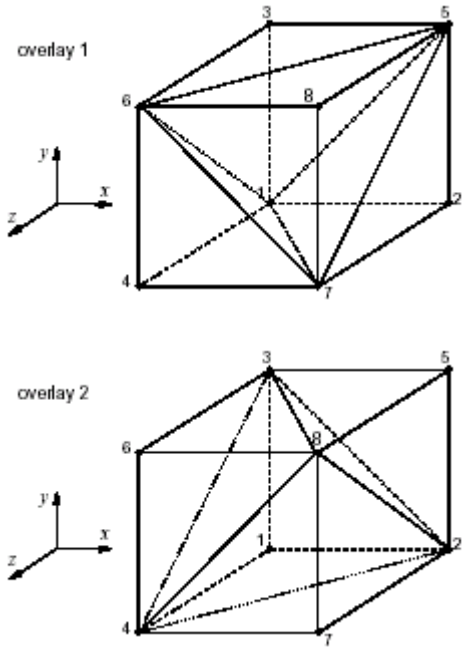

Figure 2.8. A 8-node zone in FLAC3D, with 2 overlaid sets of 5 tetrahedra each.

Σχήμα 2.8. 8-κομβικό στοιχείο του κώδικα FLAC3D, με δύο επικαλυπτόμενες ομάδες των 5 τετραεδρικών στοιχείων.

2.3.4. Discrete-model form of the finite difference equations

The finite difference equations for the triangular sub-elements of FLAC are derived using the generalized form of Gauss' divergence theorem. According to this theorem, the average value of the gradient $\left\langle \frac{\partial f}{\partial x_i} \right\rangle$ of a scalar, vector or tensor f over the area A may be computed as follows:

$$\left\langle \frac{\partial f}{\partial x_i} \right\rangle = \frac{1}{A}\int_A \frac{\partial f}{\partial x_i} dA = \frac{1}{A}\int_S n_i f dS \Rightarrow$$
$$\left\langle \frac{\partial f}{\partial x_i} \right\rangle = \frac{1}{A}\sum_s n_i \langle f \rangle \Delta s = \frac{1}{2A}\sum_s n_i \left(f^{(a)} + f^{(b)} \right) \Delta s \qquad (2.47)$$

where:

S	the boundary of a closed surface
n_i	is the unit normal to the surface
s	the length of a side of the triangle
$\langle f \rangle$	is taken to be the average over the side

The summation occurs over the three sides of the triangular sub-zone, and (a) and (b) are two consecutive nodes on a side. Equation (2.47) can be used to derive all the components of the strain rate tensor based on nodal velocities.

In FLAC3D, Equation (2.47) takes the following 3-dimensional form:

$$\begin{aligned} \left\langle \frac{\partial f}{\partial x_i} \right\rangle &= \frac{1}{V}\int_V \frac{\partial f}{\partial x_i} dA = \frac{1}{V}\int_A n_i f dA \Rightarrow \\ \left\langle \frac{\partial f}{\partial x_i} \right\rangle &= \frac{1}{V}\sum_f n_i \langle f \rangle \Delta A^{(f)} = \frac{1}{3V}\sum_f n_i \left(f^{(a)} + f^{(b)} + f^{(c)} \right) \Delta A^{(f)} \end{aligned} \tag{2.48}$$

where:

V	is the volume of the tetrahedron in consideration
A	is the tetrahedron surface
n_i	is the unit normal to the surface
$\langle f \rangle$	is taken to be the average over the surface

Here, the summation occurs over the four surfaces of each tetrahedron, denoted with the superscript (f), while (a), (b) and (c) denote the nodes of each surface.

Given the strain-rate tensor, the constitutive law of Equation (2.45) can be used to derive a new stress tensor. Once the stresses have been calculated, the equivalent forces applied to each nodal point need to be determined.

In FLAC, each quadrilateral zone contains two sets of two triangular sub-zones. Each corner of these sub-zones receives two force contributions, one from each adjoining side:

$$F_i = \frac{1}{2}\sigma_{ij}\left(n_j^{(1)} S^{(1)} + n_j^{(2)} S^{(2)} \right) \tag{2.49}$$

Within each set of sub-zones, the forces from triangles meeting at each node are summed. The forces from both sets are then averaged, to give the nodal force contribution of the quadrilateral. At each node, the forces from all surrounding quadrilaterals are summed to give the net nodal force vector, which includes contributions from applied loads and from body forces due to gravity. Gravity forces $F_i^{(g)}$ are computed as:

$$F_i^{(g)} = g_i m_g F \tag{2.50}$$

where m_g is the gravitational mass at the node, defined as the sum of one-third of the masses of triangles connected to the node.

Similarly, in FLAC3D, each corner of the tetrahedral sub-zones receives three force contributions, from each adjoining face:

$$F_i = \frac{1}{3}\sigma_{ij}\left(n_j^{(1)}A^{(1)} + n_j^{(2)}A^{(2)} + n_j^{(3)}A^{(3)}\right) \tag{2.51}$$

Within each set of sub-zones, the forces from the tetrahedra meeting at each node are summed. The nodal force contribution of each element is derived as the average of the sums of the two sets of overlaid tetrahedral sub-zones. The forces from all elements surrounding each node are summed and consequently added to externally applied loads and gravitational body forces to give the nodal force vector. The gravitational mass at each node, which is required for the computation of gravity forces, is defined as the sum of one-fourth of the masses of tetrahedra connected to the node.

In both FLAC and FLAC3D, if the body is at equilibrium, or in steady-state flow (e.g., plastic flow), F_i on the node will be zero. Otherwise, the node will be accelerated according to the finite difference form of Newton's second law of motion:

$$\dot{u}_i^{(t+\Delta t/2)} = \dot{u}_i^{(t-\Delta t/2)} + \sum F_i^{(t)} \frac{\Delta t}{m} \tag{2.52}$$

where the superscripts denote the time at which the corresponding variable is evaluated.

For large-strain problems Equation (2.52) is integrated over time to determine the coordinates x_i of the gridpoints:

$$x_i^{(t+\Delta t)} = x_i^{(t)} + \dot{u}_i^{(t+\Delta t/2)}\Delta t \tag{2.53}$$

Note that Equations (2.52) and (2.53) are both centered in time (central finite differences), with velocities existing at points in time that are shifted by half a timestep from the displacements and forces.

The above formulation is modified for the solution of static problems, by introducing into Equation (2.52) a form of damping, called local non-viscous damping, as follows:

$$\dot{u}_i^{(t+\Delta t/2)} = \dot{u}_i^{(t-\Delta t/2)} + \sum\left(F_i^{(t)} - F_{d,i}\right)\frac{\Delta t}{m} \tag{2.54}$$

where $F_{d,i}$ is the damping force, given by Equation (2.55):

$$F_{d,i} = \alpha\left|F_i^{(t)}\right|\mathrm{sgn}\left(\dot{u}_i^{(t-\Delta t/2)}\right) \tag{2.55}$$

and, by default, $\alpha = 0.80$.

2.3.5. Numerical stability

As described previously, the explicit finite difference solution procedure is not unconditionally stable. The speed of the "calculation front" must be greater than the maximum speed at which information propagates. This stability condition is expressed in terms of a critical timestep:

$$\Delta t_{crit} = \frac{\Delta x}{C} \tag{2.56}$$

where

Δx is the minimum propagation distance, estimated as $A/\Delta x_{max}$ in FLAC, and $V/\Delta A_{max}$ in FLAC3D.

C is the maximum speed at which information can propagate, namely the p-wave velocity $C_p = \sqrt{\frac{K + 4G/3}{\rho}}$.

It can be easily shown that the above expression is equivalent to Equation (2.57), which refers to a general system of solid materials and networks of interconnected masses and springs:

$$\Delta t_{crit} = \frac{T_{min}}{\pi} \tag{2.57}$$

where T_{min} is the smallest eigen-period of the system. For a single mass-spring element, the above equation becomes:

$$\Delta t_{crit} = 2\sqrt{\frac{m}{k}} \tag{2.58}$$

For the simple case of a rectangular zone, with area A_z, thickness T and diagonal length L_d, the gridpoint mass and the zone stiffness can be expressed as shown in Equations (2.59) and (2.60), respectively:

$$m = \frac{1}{4}\rho A_z T \tag{2.59}$$

$$k = \left(K + 4G/3\right)\frac{L_d^2}{A_z}T \tag{2.60}$$

It is obvious that the combination of Equations (2.58), (2.59) and (2.60) yields Equation (2.56). This implies that Equation (2.56) may be regarded as an estimate of the local critical timestep, which can be easily calculated without computing the eigen-period of the complete system.

In all cases, a timestep must be chosen that is smaller than the above critical timestep. In both FLAC and FLAC3D, a safety factor of 2 is applied for this purpose. In dynamic analyses the above timestep refers to the simulated problem time. In static analyses, it is more efficient to assume a pseudo-timestep $\Delta t = 1$ and adjust the nodal masses of Equation (2.54). In FLAC, nodal masses are computed by Equation (2.61):

$$m_n = \sum \frac{\left(K + 4G/3\right)\Delta x_{max}^2}{6A} \tag{2.61}$$

In FLAC3D, the above expression takes the following form:

$$m_n = \sum \frac{\left(K + 4G/3\right)\max\left\{\left(n_i \Delta A\right)^2\right\}}{9V} \tag{2.62}$$

In the case of effective stress analyses, where groundwater is present, the bulk modulus of the fluid increases the mechanical stiffness of the saturated zone, thus reducing the selected timestep. This is done by modifying the apparent mechanical bulk modulus of the zone, according to Equation (2.63):

$$K := K + a^2 M \tag{2.63}$$

where:

a Biot coefficient

M Biot modulus

If the compressibility of grains is neglected compared to that of the drained material, then $a = 1$ and $M = K_w / n$, where K_w is the fluid bulk modulus and n is the porosity.

Taking into account the large value of the water bulk modulus (e.g. about 200MPa), it becomes evident that in the analysis of liquefaction-related problems, where groundwater flow is present, the dynamic timestep is very small (of the order of $10^{-4}\,\text{sec}$), thus resulting to generally small strain increments. This observation is crucial for the selection of the integration algorithm of the implemented constitutive model, since the use of small integration steps improves the model's accuracy, and reduces the necessity for high-order integration schemes and complicated error-control algorithms.

2.3.6. Fluid-mechanical interaction

One of the basic features of FLAC is the capacity to model groundwater flow through permeable soils. The modeling of flow may be done uncoupled, i.e. independent of the mechanical calculations, or it may be done in a coupled way, so as to capture the effects of fluid/solid interaction. According to the latter:

- The fluid in a zone reacts to mechanically induced volume changes by a change in the pore pressure.
- Changes in pore pressures induce changes in the effective stresses, thus affecting the response of the solid.

Both FLAC and FLAC3D can calculate pore pressure effects, with or without pore pressure dissipation. They also provide a number of features, including isotropic and anisotropic permeability, partial saturation, compressibility of the saturated material,

two-phase flow, as well as a number of boundary conditions and fluid sources (prescribed inflow or outflow, varying with time).

Finally, dynamic pore pressure generation can be modeled using the "Finn" and the "Byrne" built-in constitutive models. In the model implemented herein though, dynamic pore pressure generation is modeled indirectly, as a result of the simulated decrease of effective stress.

In the simpler case of saturated flow, where grains are assumed to be incompressible compared to the soil skeleton, the equations governing the coupled fluid-deformation mechanisms are presented in the following.

First of all, water flow is described by Darcy's law:

$$q_i = -k_{ij} \frac{\partial}{\partial x_j} \left(P - \rho_w g_k x_k \right) \tag{2.64}$$

where:

- q_i specific charge vector
- k_{ij} mobility coefficient tensor (measure of permeability, equal to the hydraulic conductivity k_H – the commonly used permeability when Darcy's law is expressed in terms of head - divided by the fluid's unit weight: $k = k_H / \rho_w g$)
- P fluid pressure
- ρ_w mass density of the fluid
- g_k gravitational acceleration vector

The fluid pressure follows the constitutive law of Equation (2.65):

$$\frac{\partial P}{\partial t} = -M \frac{\partial \varepsilon_{vol}}{\partial t} \tag{2.65}$$

where:

- M Biot's fluid modulus, equal to K_w / n, where K_w is the fluid bulk modulus and n is the porosity (this only applies when grains are considered incompressible, compared to the soil skeleton)
- ε_{vol} volumetric strain

Finally, Equations (2.44) and (2.45) are expressed in terms of effective stresses $\sigma'_{ij} = \sigma_{ij} - P\delta_{ij}$, while the mass density ρ in Equation (2.44) is the saturated density $\rho_{sat} = \rho_d + n\rho_w$ (where ρ_d is the dry density).

The discretization and finite difference methods follow the general scheme presented in previous paragraphs:

- Pore pressures P are defined at gridpoints and assumed to vary linearly within each sub-zone.
- The specific charge vector q_i in Equation (2.64) is derived for each sub-zone through the Gauss divergence theorem (Equations (2.47) and (2.48)).
- The volumetric strain ε_{vol} in Equation (2.65) is the equivalent nodal volume increase arising from mechanical deformations of the grid. It is computed as the sum of the contributions from all sub-zones connected to the node. Each triangle contributes a third of its volume in FLAC, while each tetrahedron contributes one fourth of its volume in FLAC3D. The resulting sum is divided by two, to account for the double overlay scheme.
- Finally, zone pressures necessary to perform an effective stress analysis (stresses are also defined in zones), are derived from the surrounding nodal values by simple averaging.

Similar to the mechanical solution scheme, a critical timestep is defined to ensure the stability of the explicit solution of the fluid flow equations. In this case, the expression of the critical timestep has the following form:

$$\Delta t_{crit} = \frac{V}{M\sum K_{kk}} \qquad (2.66)$$

where:

V equivalent nodal volume

K_{ij} permeability matrix, relating nodal pore pressures to nodal flow rate (it is derived from the application of the Gauss divergence theorem to Equation (2.64))

The value of the timestep used in FLAC (and FLAC3D), is obtained by multiplication of the critical timestep with a safety factor of 0.8. Since the permeability appears at

the denominator of Equation (2.66), the flow timestep in many practical applications with low permeability values, becomes larger than the corresponding mechanical timestep, and is therefore not critical. The maximum flow timestep may become critical in cases that gravel or other high permeability materials are present (e.g. gravel drains), or in the numerical modeling of centrifuge experiments, where the prototype permeability is derived from the actual permeability of the model, multiplied by the centrifugal acceleration of the test.

2.3.7. User defined models

Both FLAC and FLAC3D allow the user to implement Used Defined Models (UDMs), written in C++ and compiled as Dynamic Link Libraries (DLLs). Once compiled successfully, UDMs behave just like built-in models, as far as the user is concerned. They can be installed and removed from specified zones, while their properties can be assigned, printed and plotted.

The basic incremental numerical algorithm is the following:

Given the former stress state and the total strain increment for the current timestep, the corresponding stress increment is determined and the new stress state is calculated.

It should be noted that all models are defined in terms of effective stresses. Pore pressures are used to convert total stresses to effective stresses before the constitutive model is called, while the reverse process occurs after the model calculations are complete.

The most important factor to be taken into account when implementing new constitutive models into FLAC is the fact that the UDM is called once per sub-zone (four times per quadrilateral zone in FLAC, and ten times per brick zone in FLAC3D), for every solution step. The averaging of the stress outputs is internally handled by FLAC, according to the mixed discretization technique described in the previous paragraphs. On the other hand, model parameters are stored once per zone, including the history variables used in elasto-plastic models, like the one adopted in the present work. The accumulation and averaging of these parameters must be performed inside the UDM. It must be noted that this averaging procedure may invoke errors in the application of the consistency condition of elasto-plastic model,

and was one of the main reasons for the adoption of a vanished yield surface in the constitutive model presented by Andrianopoulos (2006).

In previous versions of FLAC, constitutive models could only be written in the built-in programming language FISH. This technique was the one used by Andrianopoulos (2006). However, constitutive models written in FISH are executed with a speed which lays somewhere between one-quarter and one-third of the speed of built-in models. This problem has been overcome with C++, since the compiled DLLs perform 3 times faster than FISH models. It becomes evident that without reprogramming the model into C++, the computational cost of performing a 3-D dynamic analysis would make the numerical solution of 3-D liquefaction-related problems (e.g. seismic resoponse of shallow footings or pile foundations in a liquefaction regime) pratically impossible.

In the C++ language, the emphasis is on an object-oriented approach to program structure, where objects are represented by classes. Each object may contain data, which are encapsulated by the object and are invisible outside it. Communication with the object (and the associated data) is achieved by member functions that operate on the encapsulated data.

In addition, there is strong support for a hierarchy of objects: new object types may be derived from a base object and the base-object's member functions may be superseded by similar functions provided by the derived objects. This arrangement is very efficient in terms of program modularity. For example, the main program may need to access many different varieties of the derived objects in many different parts of the code. However, it does not need to make reference to the derived objects, but only to the base-objects. In this case, the appropriate member functions of the derived objects are automatically called.

This methodology is exploited in FLAC's support for UDMs. A base class, called **ConstitutiveModel**, provides the framework for actual constitutive models. No object of this base class can be created. However, new classes may be derived from the base class, representing the User Defined Models. Objects of the derived classes may be created, referring to zones with the assigned UDM.

The ConstitutiveModel base class is termed an "abstract" class because it declares a number of "virtual" member functions. The derived classes must supply real member

functions to replace the virtual functions of ConstitutiveModel, and to define the name, the properties and the mechanical behavior of the specific user-defined constitutive model. The most important member functions are summarized in the following:

- The **Keyword()** function returns a pointer to a character array containing the name of the constitutive model, as the user will refer to it within FLAC.
- The **Name()** function returns a pointer to a character array containing the name of the constitutive model that is to be used on printout.
- The **Properties()** function returns a pointer to an array of strings, containing the names of model properties, with a null pointer to denote the end of the character array of strings.
- The **SetProperty(**unsigned **n**, const double **&dVal)** function is used to store the supplied value **dVal**, given to FLAC as user input, to the model's private memory location, corresponding to the model property with sequential number **n**.
- The **GetProperty(**unsigned **n)** function returns to FLAC the value of the property with sequential number **n**.
- An **Initialize(**unsigned **uDim**, State ***ps)** function is called once for each model object (i.e., for each full zone), allowing to perform initialization of its variables.
- The **Run(**unsigned **uDim**, State **ps)** function is called from FLAC at each cycle, once for each sub-zone. The dimensionality (2 for FLAC and 3 for FLAC3D) is given as **uDim**, while the structure **ps** contains the current stress components and the computed strain increment components for the sub-zone being processed. The model must update the stress tensor from strain increments.
- The **ConfinedModulus()** function must return a value for the maximum confined modulus, which is used by FLAC to compute the stable timestep, as described in the previous paragraphs.
- The **ShearModulus()** function must return a value for the current tangent shear modulus, which is used by FLAC to determine coefficients for the quiet

and free-field boundaries, that can by used when performing dynamic analyses.

- Finally, the **SaveRestore(**ModelSaveObject ***mso)** function allows the model to save and restore data members of each object.

FLAC is made aware of a user-written constitutive model by a constructor call invoked by a static global instance of the model class. This call causes the base constructor to "register" the new model, and add it to the list of models. The static instance of the model is consulted whenever FLAC needs any information about the model (i.e. model name or property name), or when it needs to create a copy of the model (i.e. assign the model to a zone).

As previously described, the most important link between FLAC and a UDM is the member-function **Run(**unsigned **nDim**, State ***ps)**, which computes the mechanical response of the model during cycling. A structure, State ***ps**, is used to transfer information to and from the model. The most important members of **ps** are summarized in the following:

- **bySubZone** is the sequence number of the sub-zone currently being processed, while **byTotSubZones** is the total number of sub-zones in the specific zone (including those from all overlays - **byOverlay** is the number of overlays). This information is used in the UDM to scale accumulated sub-zone data correctly. For example, if four sub-zones are present (as in the 2-D version of FLAC), accumulated values will need to be divided by four, in order to obtain the average for the whole zone.
- **dSubZoneVolume** is the volume of the current sub-zone, while **dZoneVolume** is the total zone volume.
- **STensor stnE** is the strain increment tensor, which is input to the constitutive model.
- **STensor stnS** is the Stress tensor. The current effective stress tensor is input to the constitutive model, and the model must return the updated tensor.

In order for the user to load UDMs into FLAC, the program must be first configured to accept DLL models by giving the **CONFIG cppudm** command. Then, the model DLL may be loaded by giving the command **MODEL load <filename>**, with the

filename of the DLL. Thereafter, the new model name and property names will be recognized by FLAC, and can be used just like any built-in models.

2.4. Integration scheme

In previous paragraphs, it is explained that the implementation of a user-defined constitutive model into the finite difference code FLAC essentially requires to develop a numerical algorithm for the computation of the stress increment, for a given current stress state and a given strain increment. In other words, the constitutive stress-strain relationship needs to be explicitly integrated. In the general framework of elasto-plasticity, this relationship has the form of Equation (2.1), while for the specific constitutive model, this equation can be rearranged into Equation (2.42).

It must be stressed that explicit integration schemes can be easily applied for the numerical integration of exceedingly complex constitutive laws, as they are straightforward to implement. In contrast, implicit methods, which are commonly used with the Finite Element Method, are difficult to implement, except for the case of relatively simple soil models. This is because the gradients of the yield and the plastic potential surface, as well as the hardening law need to be evaluated for the final stress state, which is unknown. Therefore, the resulting system of non-linear equations must be solved iteratively. If the modified Newton-Raphson scheme is used for this purpose, then second derivatives of the yield function and plastic potential need to be computed in order to implement the iterative procedure, thus leading to much tedious algebra for complex soil plasticity models. In the model used herein, the gradients of the yield and the plastic potential surface, L_{ij} and R_{ij} respectively, are given by Equations (2.12) and (2.13), as functions of the unit vector n_{ij}. Figure 2.5 schematically illustrates the mapping rule adopted for the definition of n_{ij}, thus indicating the complexity of deriving the differentials of L_{ij} and R_{ij}, and justifying the selection of the explicit finite difference code FLAC, for the implementation of the model.

Effective algorithms for the explicit numerical integration of complex elastoplastic constitutive models, have been presented by Sloan et al (2001) and incorporated in the work of Andrianopoulos (2006). These algorithms may automatically divide the applied strain increment into sub-increments (sub-steps), in order to control the global

integration error. Using an estimate of the local error, the size and the number of sub-steps become a function of the specified error tolerance, the magnitude of the imposed strain increment, and the non-linearity of the constitutive relations. The algorithms presented by Sloan et al (2001) use either a modified Euler scheme or a Runge-Kutta-Dormand-Prince scheme to estimate the local error in the computed stresses and to control the sub-division of the applied strain increment.

2.4.1. Modified Euler integration scheme, with automatic substepping and error control

Following the work of Andrianopoulos (2006), the modified Euler scheme is used herein, together with the aforementioned sub-stepping and automatic error control algorithm. According to this specific algorithm, for each timestep Δt a pseudo time T $(0 \le T \le 1)$ is defined, as:

$$T = \frac{t - t_o}{\Delta t} \tag{2.67}$$

where:

t is the current time

t_o is the time at the start of the load increment

Differentiating Equation (2.67) yields:

$$\frac{dT}{dt} = \frac{1}{\Delta t} \tag{2.68}$$

Therefore, Equation (2.1) becomes:

$$\Delta\sigma_{ij}^{(\Delta T)} = \Delta T \frac{d\sigma_{ij}}{dT} = \Delta T \Delta t \dot{\sigma}_{ij} = C_{ijkl}^{ep}\left(\Delta T \Delta t \dot{\varepsilon}_{ij}\right) = C_{ijkl}^{ep}\left(\Delta T \Delta \varepsilon_{ij}\right) \tag{2.69}$$

In this way, the stress-strain relationship can be integrated over the pseudo-time interval $T = 0$ to $T = 1$, with the stress sub-increment $\Delta\sigma_{ij}^{(\Delta T)}$ corresponding to the pseudo-time increment ΔT, being computed from the same constitutive equations, for a strain sub-increment $\Delta\varepsilon_{ij}^{(\Delta T)}$ equal to:

$$\Delta\varepsilon_{ij}^{(\Delta T)} = \Delta T \Delta \varepsilon_{ij} \tag{2.70}$$

where $\Delta\varepsilon_{ij}$ is the total strain increment for the full timestep.

The pseudo-time is consequently divided into smaller increments $\Delta T^{(n)}$ where n denotes the pseudo-time $T^{(n)} = T^{(n-1)} + \Delta T^{(n)}$, as well as the associated stresses $\sigma_{ij}^{(n)}$ and the values $q^{(n)}$ of the model's hardening parameters.

In the constitutive model used herein, the hardening parameters are:

- The deviatoric stress ratio r_{ij}^{LR} which is defined at load reversal, i.e. when $\Lambda < 0$.
- The fabric variables f_p and f_{ij}, evolving according to Equations (2.36) and (2.37).

For convenience, the evolution of the above hardening parameters will be expressed as $\Delta q = \Lambda\left(\sigma_{ij}, q\right)\overline{q}\left(\sigma_{ij}\right)$.

The applied integration algorithm is schematically illustrated in Figure 2.9 and summarized in the following steps:

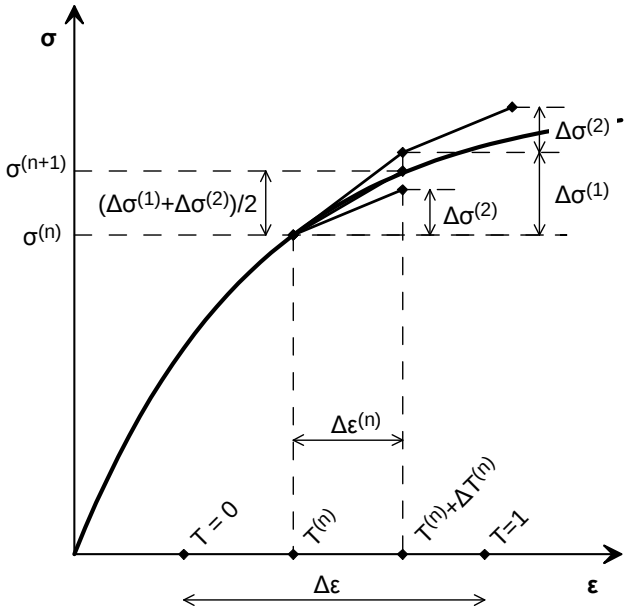

Figure 2.9. Modified Euler integration scheme with automatic sub-stepping and error control.

Σχήμα 2.9. Τροποποιημένη ολοκλήρωση κατά Euler με αυτόματη υποδιαίρεση του βήματος ολοκλήρωσης και έλεγχο σφάλματος.

Step 1

The current stress $\sigma_{ij}^{(0)}$, the strain increment $\Delta\varepsilon_{ij}$, and the current values of the hardening parameters $q^{(0)}$ are given by FLAC and input to the UDM code, while variables $T^{(0)}$ and $\Delta T^{(1)}$ are initialized:

$$T^{(0)} = 0 \tag{2.71}$$

$$\Delta T^{(1)} = 1 \tag{2.72}$$

Step 2

Steps 3-7 are repeated, for $n = 1,2,3...$, until $T^{(n)} = \sum_{i=1}^{n} \Delta T^{(i)} = 1$.

Step 3

The stress increment $\Delta\sigma_{ij}^{(n)}$ and the corresponding increment of the hardening parameters $\Delta q^{(n)}$ are estimated using the Modified Euler integration scheme, for a strain increment given by Equation (2.73):

$$\Delta\varepsilon_{ij}^{(n)} = \Delta T^{(n)} \Delta\varepsilon_{ij} \tag{2.73}$$

More specifically, a first stress increment estimate $\Delta\sigma_{ij}^{(1)}$ is computed using Equation (2.74):

$$\Delta\sigma_{ij}^{(1)} = C_{ijkl}^{ep}\left(\sigma_{ij}^{(n-1)}, q^{(n-1)}\right)\Delta\varepsilon_{ij}^{(n)} \tag{2.74}$$

The corresponding increment $\Delta q^{(1)}$ of the hardening parameters is computed using Equation (2.75):

$$\Delta q^{(1)} = \Lambda\left(\sigma_{ij}^{(n-1)}, q^{(n-1)}\right)\bar{q}\left(\sigma_{ij}^{(n-1)}\right) \tag{2.75}$$

A second pair of estimates $\Delta\sigma_{ij}^{(2)}$ and $\Delta q^{(2)}$ is computed using Equations (2.76) and (2.77).

$$\Delta\sigma_{ij}^{(2)} = C_{ijkl}^{ep}\left(\sigma_{ij}^{(n-1)} + \Delta\sigma_{ij}^{(1)}, q^{(n-1)} + \Delta q^{(1)}\right)\Delta\varepsilon_{ij}^{(n)} \tag{2.76}$$

$$\Delta q^{(2)} = \Lambda\left(\sigma_{ij}^{(n-1)} + \Delta\sigma_{ij}^{(1)}, q^{(n-1)} + \Delta q^{(1)}\right)\bar{q}\left(\sigma_{ij}^{(n-1)} + \Delta\sigma_{ij}^{(1)}\right) \tag{2.77}$$

Finally, the increments $\Delta\sigma_{ij}^{(n)}$ and $\Delta q^{(n)}$ are given from Equations (2.78) and (2.79):

$$\Delta\sigma_{ij}^{(n)} = \frac{\Delta\sigma_{ij}^{(1)} + \Delta\sigma_{ij}^{(2)}}{2} \tag{2.78}$$

$$\Delta q^{(n)} = \frac{\Delta q^{(1)} + \Delta q^{(2)}}{2} \tag{2.79}$$

Step 4

Since the local error in the Euler and modified Euler integration schemes is $O\left(\Delta T^2\right)$ and $O\left(\Delta T^3\right)$ respectively, the error in $\Delta\sigma_{ij}^{(n)}$ and $\Delta q^{(n)}$ can be estimated from:

$$\begin{Bmatrix} \Delta\hat{\sigma}_{ij}^{(n)} \\ \hat{q}^{(n)} \end{Bmatrix} - \begin{Bmatrix} \Delta\sigma_{ij}^{(n)} \\ q^{(n)} \end{Bmatrix} = \begin{Bmatrix} \frac{1}{2}\left(\Delta\sigma_{ij}^{(1)} + \Delta\sigma_{ij}^{(2)}\right) - \Delta\sigma_{ij}^{(1)} \\ \frac{1}{2}\left(\Delta q^{(1)} + \Delta q^{(2)}\right) - \Delta q^{(1)} \end{Bmatrix} = \begin{Bmatrix} \frac{1}{2}\left(\Delta\sigma_{ij}^{(2)} - \Delta\sigma_{ij}^{(1)}\right) \\ \frac{1}{2}\left(\Delta q^{(2)} - \Delta q^{(1)}\right) \end{Bmatrix} \tag{2.80}$$

Therefore, a relative error measure $R^{(n)}$ can be computed using Equation (2.81):

$$R^{(n)} = \frac{1}{2}\max\left\{\frac{\left\|\Delta\sigma_{ij}^{(2)} - \Delta\sigma_{ij}^{(1)}\right\|}{\left\|\sigma_{ij}^{(n)}\right\|}, \frac{\left\|\Delta q^{(2)} - \Delta q^{(1)}\right\|}{\left\|q^{(n)}\right\|}\right\} \tag{2.81}$$

It may be observed that for strain increments tending to zero, this relative error would become equal to the second derivative of the stress-strain relationship, for the given loading direction, normalized by the current stress:

$$R_{\Delta\varepsilon_{ij}\to 0} = \frac{\left\|\partial\sigma_{ij} \middle/ \partial\varepsilon_{ij}\right\|}{\left\|\sigma_{ij}\right\|} \tag{2.82}$$

Therefore, this relative error may also be regarded as a measure of the local degree of non-linearity, of the stress-strain relationship.

Step 5

The relative error $R^{(n)}$ is compared to the tolerance variable $STOL$. This variable has been implemented as a model property, that can be externally defined by the UDM user. The optimum value for $STOL$ proposed by Sloan et al (2001) is $STOL = 10^{-3}$, and this is the current default value for $STOL$ in the UDM.

If $R^{(n)} > STOL$ (and $\Delta T^{(n)} > \Delta T_{min}$) then the substep is rejected, and steps 3-4 are repeated for a smaller time increment $\Delta T^{(n')}$:

$$\Delta T^{(n')} = \max\left\{ q\Delta T^{(n)}, \Delta T_{min} \right\} \tag{2.83}$$

where:

$$q = 0.9\sqrt{\frac{STOL}{R^{(n)}}} \geq 0.1 \tag{2.84}$$

The value of ΔT_{min} is the minimum timestep value, introduced by Sloan et al (2001) for reasons of code robustness. In the implemented UDM, it can be defined by the user, with $\Delta T_{min} = 10^{-3}$ being the default minimum timestep, corresponding to a maximum of 1000 sub-steps.

Equation (2.84) is obtained from the requirement:

$$R^{(n')} \leq STOL \tag{2.85}$$

Given that the local error estimated by Equation (2.80) is $O\left(\Delta T^2\right)$, yields Equation (2.86):

$$R^{(n')} = \left(\frac{\Delta T^{(n')}}{\Delta T^{(n)}} \right)^2 R^{(n)} = q^2 R^{(n)} \tag{2.86}$$

which, combined with Equation (2.85) yields:

$$q = \sqrt{\frac{STOL}{R^{(n)}}} \tag{2.87}$$

The coefficient of 0.9 in Equation (2.84) acts as a safety factor for cases of highly non-linear behavior. Even though it leads to smaller sub-increment sizes, and consequently more sub-increments, it reduces the number of failed sub-increments and increases the algorithm's efficiency (Sloan et al, 2001).

Step 6

If $R^{(n)} \le STOL$, or if $\Delta T^{(n)} = \Delta T_{min}$, then the substep is accepted, stresses and hardening parameters are updated and a new timestep $\Delta T^{(n+1)}$ is selected:

$$\sigma_{ij}^{(n+1)} = \sigma_{ij}^{(n)} + \Delta\sigma_{ij}^{(n)} \tag{2.88}$$

$$q^{(n+1)} = q^{(n)} + \Delta q^{(n)} \tag{2.89}$$

$$T^{(n+1)} = T^{(n)} + \Delta T^{(n)} \tag{2.90}$$

$$\Delta T^{(n+1)} = q\Delta T^{(n)} \tag{2.91}$$

where:

$$q = 0.9\sqrt{\frac{STOL}{R^{(n)}}} \le 1.1 \tag{2.92}$$

If the last substep had been accepted with $R_n > STOL$ and $\Delta T^{(n)} = \Delta T_{min}$, then $q = 1$.

Step 7

The new timestep must be checked so that total time T will not overcome unity:

$$\Delta T^{(n+1)} \le 1 - T^{(n)} \tag{2.93}$$

Step 8

Return the final values of σ_{ij} and q to FLAC, and continue with the next timestep.

2.4.2. Simple integration schemes

The aforementioned modified Euler integration algorithm, with automatic sub-stepping and error control, has been shown to provide accurate results (Andrianopoulos, 2006). However, its main disadvantage is the high computational

cost, which noticeably increases the analysis time. On the other hand, FLAC and FLAC3D both use a very small timestep, in order to ensure the stability of the explicit finite difference solution scheme. In the case of liquefaction-related problems, this timestep is further reduced, due to the large value of the water's bulk modulus. Thus, strain increments are restricted to relatively small values (of the order of 10^{-5} for a typical liquefaction analysis, such as the ones shown in the following chapters). It becomes clear that if strain increments are sufficiently small, further sub-stepping might not be necessary. This observation indicates that simpler integration schemes could be used for the UDM's implementation, thus increasing the model's computational efficiency and reducing the analysis time. However, as these simpler algorithms would lack in accuracy, further investigation was conducted, focusing on the following issues:

- The development of an automatic algorithm, based on the error control concept presented by Sloan et al (2001). This algorithm switches between different integration schemes, depending on the local degree of non-linearity of the stress-strain relationship.
- The determination of a critical strain increment value, beyond which, sub-stepping and error control would become indispensable.

Before proceeding to the finally adopted algorithm, two more simplified integration schemes will be presented, namely the modified Euler integration scheme and the single-step Euler integration scheme.

2.4.3. Modified Euler integration scheme, without error-control and substepping

The version of the modified Euler integration scheme is schematically illustrated in Figure 2.10 and summarized in the following steps:

Step 1

The current stress $\sigma_{ij}^{(0)}$, the strain increment $\Delta\varepsilon_{ij}$, and the current values of the hardening parameters $q^{(0)}$ are given by FLAC and input to the UDM code.

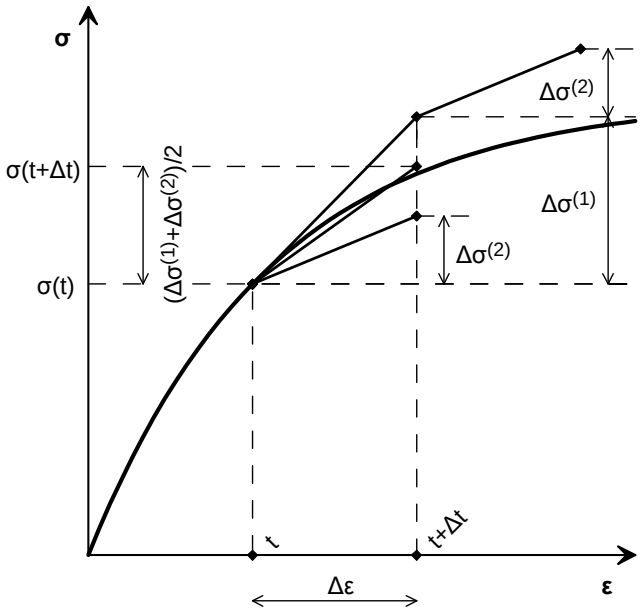

Figure 2.10. Modified Euler integration scheme without sub-stepping.

Σχήμα 2.10. Τροποποιημένη ολοκλήρωση κατά Euler χωρίς υποδιαίρεση του βήματος ολοκλήρωσης.

Step 2

The stress increment $\Delta\sigma_{ij}$ and the corresponding increment of the hardening parameters Δq are estimated using the Modified Euler integration scheme. More specifically, a first stress increment estimate $\Delta\sigma_{ij}^{(1)}$ is computed using Equation (2.94):

$$\Delta\sigma_{ij}^{(1)} = C_{ijkl}^{ep}\left(\sigma_{ij}^{(0)}, q^{(0)}\right)\Delta\varepsilon_{ij} \tag{2.94}$$

The corresponding increment $\Delta q^{(1)}$ of the hardening parameters is computed using Equation (2.95):

$$\Delta q^{(1)} = \Delta q^{(1)} = \Lambda\left(\sigma_{ij}^{(0)}, q\right)\bar{q}\left(\sigma_{ij}^{(0)}\right) \tag{2.95}$$

A second pair of estimates $\Delta\sigma_{ij}^{(2)}$ and $\Delta q^{(2)}$ is computed using Equations (2.96) and (2.97).

$$\Delta\sigma_{ij}^{(2)} = C_{ijkl}^{ep}\left(\sigma_{ij}^{(0)} + \Delta\sigma_{ij}^{(1)}, q^{(0)} + \Delta q^{(1)}\right)\Delta\varepsilon_{ij} \tag{2.96}$$

$$\Delta q^{(1)} = \Delta q^{(2)} = \Lambda\left(\sigma_{ij}^{(0)} + \Delta\sigma_{ij}^{(1)}, q^{(0)} + \Delta q^{(1)}\right)\bar{q}\left(\sigma_{ij}^{(0)} + \Delta\sigma_{ij}^{(1)}\right) \tag{2.97}$$

Finally, the increments $\Delta\sigma_{ij}$ and Δq are given from Equations (2.98) and (2.99):

$$\Delta\sigma_{ij} = \frac{\Delta\sigma_{ij}^{(1)} + \Delta\sigma_{ij}^{(2)}}{2} \tag{2.98}$$

$$\Delta q = \frac{\Delta q^{(1)} + \Delta q^{(2)}}{2} \tag{2.99}$$

Step 3

Stresses and hardening parameters are updated and returned to FLAC.

$$\sigma_{ij} = \sigma_{ij}^{(0)} + \Delta\sigma_{ij} \tag{2.100}$$

$$q = q^{(0)} + \Delta q \tag{2.101}$$

It may be observed that this integration scheme essentially consists of a reduced form of the algorithm presented by Sloan et al (2001), which may be alternatively achieved by either setting a large value of STOL (i.e. 10^3), or using small strain increments in order to minimize the relative error. As explained previously, strain increments are already limited to small values, due to the small timestep incorporated by FLAC and FLAC3D, in order to resolve stability-related issues. Therefore, integration steps are not expected to be further divided into smaller substeps, except for the cases where the predicted soil behavior becomes highly non-linear. In other words, the application of a modified Euler scheme, without substepping and error control, is not expected to perform much faster than the effective integration algorithm of Sloan et al (2001). The only computational benefit will arise when the stress-strain relationship enters regions of intense non-linearity. However, it would be definitely unsuitable to bypass automatic error control and substepping in these integration steps, as this local increase in computational efficiency would have been obviously accompanied by a significant lack in accuracy.

2.4.4. Single-step Euler integration scheme

The simplest integration scheme applied in the present work consists of the performance of a single Euler integration step. The integration procedure is schematically illustrated in Figure 2.11 and summarized in the following steps:

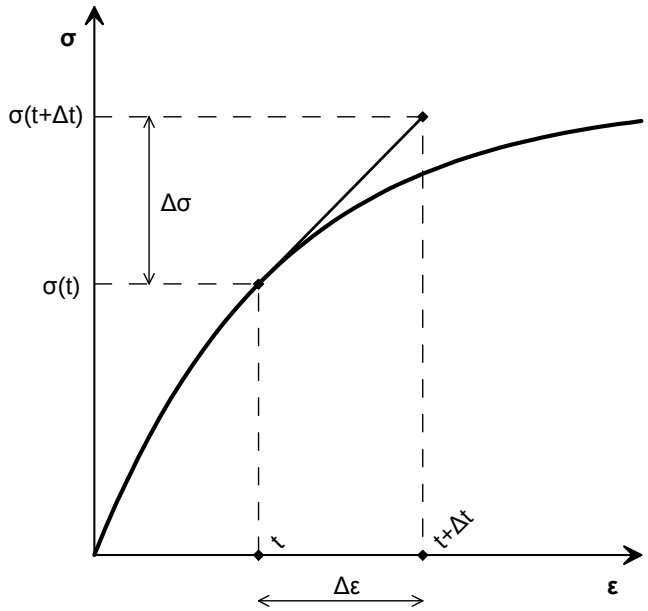

Figure 2.11. Single-step Euler integration scheme.

Σχήμα 2.11. Απλή ολοκλήρωση κατά Euler.

Step 1

The current stress $\sigma_{ij}^{(0)}$, the strain increment $\Delta\varepsilon_{ij}$, and the current values of the hardening parameters $q^{(0)}$ are given by FLAC and input to the UDM code.

Step 2

The stress increment $\Delta\sigma_{ij}$ and the corresponding increment of the hardening parameters Δq are estimated using Equations (2.106) and (2.107):

$$\Delta\sigma_{ij} = C_{ijkl}^{ep}\left(\sigma_{ij}^{(0)}, q^{(0)}\right)\Delta\varepsilon_{ij} \tag{2.102}$$

$$\Delta q = \Lambda\left(\sigma_{ij}^{(0)}, q\right)\bar{q}\left(\sigma_{ij}^{(0)}\right) \tag{2.103}$$

Step 3

Finally, stresses and hardening parameters are updated and returned to FLAC.

$$\sigma_{ij} = \sigma_{ij}^{(0)} + \Delta\sigma_{ij} \tag{2.104}$$

$$q = q^{(0)} + \Delta q \tag{2.105}$$

It becomes obvious that in this integration scheme, model computations are only performed once for each step. The algorithm is therefore expected to perform 2 times faster than the modified Euler scheme without error-control and substepping. However, the penalty paid for the considerably increased efficiency, is the lack of accuracy, as the error increases by one order of magnitude ($O\left(\Delta t^2\right)$ instead $O\left(\Delta t^3\right)$ in the modified Euler scheme). Moreover, this scheme does not allow for any estimation of the local error to be made, thus it is not possible to have any control on the accuracy of the integration procedure, and automatic substepping algorithms may not be applied.

2.4.5. Combined integration scheme

As explained in the above, the single-step integration scheme may become twice as effective than the double-step modified Euler scheme, but it does not allow for any error control to be applied and thus lacks in robustness. Therefore, a combined integration scheme was developed and adopted in the UDM, automatically switching from single-step integration to modified Euler integration with automatic substepping and error control. Substepping and error control may be omitted, depending on the value of the $STOL$ variable, defined by the UDM user.

The main concept of the proposed algorithm is similar to the error estimation procedure proposed by Sloan et al (2001). In both schemes, the error is measured from the difference of two consecutive stress increments, as shown in Equation (2.81). In the original algorithm of Sloan et al (2001), this difference is derived from the two increments of the modified Euler integration procedure. In the proposed algorithm, the local error measure is estimated using the stress increments of two consecutive steps. If this error measure remains below a given tolerance value $MSTOL$, then integration is performed using the single-step Euler scheme. If this value is exceeded, then modified Euler integration is activated.

According to this procedure, the current stress increment is actually regarded as the second stress increment of a modified Euler procedure that would have been applied in the previous step. Therefore, the estimated error does not correspond to the current step, but to the previous one. Since FLAC and FLAC3D do not allow for any corrections to be made in previously completed timesteps, it may seem that the application of a higher order integration scheme is not performed where necessary,

but actually it is performed with the delay of one timestep, thus not contributing to the increase of integration accuracy.

However, application of the previously presented integration schemes has indicated that there are distinct regions in the stress-strain relationship where non-linear behavior is not predominant, and where the single-step integration scheme is sufficiently accurate. Similarly, there are highly non-linear regions, where the use of higher-order integration schemes and potential substepping becomes imperative. These two regions are not singular timesteps, but entire sections of the stress-strain relationship, with a duration of many subsequent timesteps. According to the proposed methodology, when the stress state enters a region of high non-linearity, the estimated error increases and the modified Euler scheme is applied. Of course, during the first timestep of this highly non-linear region, the stress increment is not accurately predicted. However, the increased error measure implies the use of the modified Euler scheme in the subsequent timesteps. In other words, even with the delay of one single substep, this "combined integration" algorithm essentially allows to switch between the two different integration schemes, depending on the current highly or weakly non-linear soil behavior. In other words, the developed algorithm allows the integration scheme to adapt to the local degree of non-linearity of the stress-strain relationship, thus achieving the optimum balance between the accuracy of the integration procedure and the involved computational cost. Finally, it should be stressed that the small integration timestep which is used by FLAC in order to ensure the stability of the explicit finite difference solution scheme, results in the minimization of the effect of this single step delay on the overall accuracy.

The combined integration scheme is summarized in the following steps:

Step 1

The current stress $\sigma_{ij}^{(k)}$, the strain increment $\Delta\varepsilon_{ij}^{(k)}$, and the current values of the hardening parameters $q^{(k)}$ are given by FLAC and input to the UDM code.

Step 2

The stress increment $\Delta\sigma_{ij}^{(k)}$ and the corresponding increment of the hardening parameters $\Delta q^{(k)}$ are estimated using Equations (2.106) and (2.107):

$$\Delta\sigma_{ij}^{(k)} = C_{ijkl}^{ep}\left(\sigma_{ij}^{(k)}, q^{(k)}\right)\Delta\varepsilon_{ij}^{(k)} \tag{2.106}$$

$$\Delta q^{(k)} = \Lambda\left(\sigma_{ij}^{(k)}, q^{(k)}\right)\overline{q}\left(\sigma_{ij}^{(k)}\right) \tag{2.107}$$

Step 3

The accuracy of the single-step integration scheme for the previous step is evaluated. More specifically, the current stress increment $\Delta\sigma_{ij}^{(k)}$ is regarded as the second stress increment of a modified Euler scheme that would have been applied during the previous timestep. Therefore, a more accurate estimation $\Delta\hat{\sigma}_{ij}^{(k-1)}$ of the previous step's stress increment and the current stress $\hat{\sigma}_{ij}^{(k)}$ may be given by Equations (2.108) and (2.109), respectively:

$$\Delta\hat{\sigma}_{ij}^{(k-1)} = \frac{\Delta\sigma_{ij}^{(k-1)} + \Delta\overline{\sigma}_{ij}^{(k)}}{2} \tag{2.108}$$

$$\hat{\sigma}_{ij}^{(k)} = \sigma_{ij}^{(k-1)} + \Delta\hat{\sigma}_{ij}^{(k-1)} \tag{2.109}$$

In order to account for the different strain increments of the two individual integration steps, the current stress increment value $\Delta\sigma_{ij}^{(k)}$ is adjusted as:

$$\Delta\overline{\sigma}_{ij}^{(k)} = \frac{\left\|\Delta\varepsilon_{ij}^{(k-1)}\right\|}{\left\|\Delta\varepsilon_{ij}^{(k)}\right\|}\Delta\sigma_{ij}^{(k)} \tag{2.110}$$

This adjustment is not totally accurate, as it does not take into account changes in the direction of the strain increment. This would have great significance in load reversals. However, in this case, the error computed in the following steps would increase, thus forcing the algorithm to switch into the use of the more accurate modified Euler integration scheme.

Step 4

Similarly to the integration scheme presented by Sloan et al (2001), an error estimate for the stress increment $\Delta\sigma_{ij}^{(k-1)}$ may be calculated using Equation (2.111):

$$R = \frac{1}{2}\frac{\left\|\Delta\bar{\sigma}_{ij}^{(k)} - \Delta\sigma_{ij}^{(k-1)}\right\|}{\left\|\hat{\sigma}_{ij}^{(k-1)}\right\|} \qquad (2.111)$$

Step 5

The error estimate computed in Step 4 is compared to a tolerance variable $MSTOL$, which has been implemented as a model property and can be externally defined by the UDM user:

- If $R \le MSTOL$, then the single-step integration scheme is considered accurate, either due to the small strain increment defined by FLAC, or because the current stress state is far from the highly non-linear regions of the constitutive relation. Therefore, the stress increment $\Delta\sigma_{ij}^{(k)}$ is used to compute $\sigma_{ij}^{(k+1)}$, which is consequently returned to FLAC.

- If $R > MSTOL$, then the single-step integration scheme is not accurate, and a more accurate scheme (i.e. the modified Euler scheme) needs to be applied. In this case, the stress increment $\Delta\sigma_{ij}^{(k)}$ may be used as the first increment of the modified Euler scheme, thus only the second increment needs to be computed. The use of automatic substepping and error control depends on the selected value for the $STOL$ variable. For small tolerance values, the UDM performs the previously described error control procedure, while for larger values (i.e. $STOL = 10^3$) substepping does not occur and the integration scheme reduces to a simple modified Euler scheme.

The accuracy and computational efficiency of this combined algorithm is evaluated in Chapter 3, and compared to the simple single-step algorithm, the modified Euler algorithm, and the modified Euler algorithm with automatic error control and substepping.

2.5. Mapping rule

An important part of the integration algorithm is the application of the model's mapping rule, which was described in previous paragraphs and schematically illustrated in Figure 2.5. Due to the complicacy of the mapping rule, an iterative procedure is required, which demands high computational effort and increases the analysis time. Therefore, the algorithm adopted by Andrianopoulos (2006) for the application of the mapping rule was modified, aiming to increase the code's computational efficiency. This modification takes advantage of the small critical timestep used by FLAC to ensure the stability of the explicit finite difference scheme, by using the results from the previous step, as an initial value for the iterative procedure.

The application of the mapping rule essentially refers to the determination of the image point r_{ij}^{IP} on the bounding surface (Figure 2.5). This conjugate point lies on the line defined by the current deviatoric stress ratio r_{ij} and a reference point, namely the deviatoric stress ratio at last load reversal r_{ij}^{LR}. The location of this point may be expressed as a function of r_{ij} and r_{ij}^{LR}, with the aid of a variable a, as shown in Equation (2.112):

$$r_{ij}^{IP}(a) = r_{ij}^{LR} + a\left(r_{ij} - r_{ij}^{LR}\right) \tag{2.112}$$

The value of a must satisfy the condition that r_{ij}^{IP} lies on the bounding surface. In agreement with the definition of the model surfaces, presented in the previous paragraphs, the distance $F_{BS}(a)$ from the bounding surface can be computed using Equation (2.113):

$$F_{BS}(a) = r_{ij}^{IP}(a) r_{ij}^{IP}(a) - \sqrt{\frac{2}{3}} M_{\theta}^{b}\left(n_{ij}\right) \tag{2.113}$$

where n_{ij} is the unit vector in the direction of r_{ij}^{IP}:

$$n_{ij} = \frac{r_{ij}^{IP}}{\sqrt{r_{kl}^{IP} r_{kl}^{IP}}} \tag{2.114}$$

and M_0^b is computed according to Equation (2.15).

Positive values of $F_{BS}(a) > 0$ correspond to points r_{ij}^{IP} lying outside the Bounding Surface, while if $F_{BS}(a) < 0$ the corresponding point r_{ij}^{IP} is located inside the surface. In order for r_{ij}^{IP} to be the required image point, the condition $F_{BS}(a) = 0$ must be satisfied. It becomes evident that the above equations are interlaced, and an iterative procedure is necessary for the determination of coefficient a and the consequent computation of the unit vector n_{ij}.

2.5.1. Algorithm proposed by Andrianopoulos (2006)

The iterative algorithm proposed by Andrianopoulos (2006) for this purpose is summarized in the following steps:

Step 1

The final value of coefficient a is assumed to lie between two variables, namely a_0 and a_1. The initial values for these variables are $a_0 := 0$ and $a_1 := 1$.

Step 2

The distances $F_{BS}(a_0)$ and $F_{BS}(a_1)$ of the points corresponding to the values a_0 and a_1, from the model's Bounding Surface are initially computed.

Step 3

If $F_{BS}(a_1) > 0$ then a_0 and a_1 are accepted as bounding values of a, and the procedure continues with Step 4.

If $F_{BS}(a_1) < 0$ then a_0 and a_1 are updated to $a_0 := a_1$ and $a_1 := 2a_1$, and Steps 2-3 are repeated, until a proper pair of a_0 and a_1 is determined. $F_{BS}(a_0)$ does not need to be recomputed, as it is equal to $F_{BS}(a_1)$ from the previous step.

Step 4

The value of a is estimated by Equation (2.115):

$$a = a_1 - (a_1 - a_0)\frac{F_{BS}(a_1)}{F_{BS}(a_1) - F_{BS}(a_0)} \tag{2.115}$$

Step 5

The distance $F_{BS}(a)$ of the point corresponding to the value a is computed.

Step 6

If $|F_{BS}(a)| \le 10^{-5}$ then the image point has been found ($r_{ij}^{IP} = r_{ij}^{IP}(a)$) and the procedure is finished.

If $|F_{BS}(a)| > 10^{-5}$ and $F_{BS}(a) < 0$ then the correct value lies between a and a_1. Therefore, $a_0 := a$, $F_{BS}(a_0) := F_{BS}(a)$ and Steps 4-6 are repeated.

If $|F_{BS}(a)| > 10^{-5}$ and $F_{BS}(a) > 0$ then the correct value lies between a_0 and a. Therefore, $a_1 := a$, $F_{BS}(a_1) := F_{BS}(a)$ and Steps 4-6 are repeated.

2.5.2. Modified algorithm for the application of the model's mapping rule

Due to the complicacy of the equations involved in the calculation of $F_{BS}(a)$, the above algorithm is associated to relatively high computational cost. In order to increase the computational efficiency of the UDM, the above algorithm was replaced with a more straight-forward procedure. More specifically, combining Equations (2.112) and (2.113) with the condition $F_{BS}(a) = 0$, yields a binomial for the variable a:

$$\left(dr_{ij}dr_{ij}\right)a^2 + \left(2dr_{ij}r_{ij}^{LR}\right)a + \left(r_{ij}^{LR}r_{ij}^{LR} - \sqrt{\frac{2}{3}}M_{\theta}^{b}\left(n_{ij}\right)\right) = 0 \tag{2.116}$$

where:

$$dr_{ij} = r_{ij} - r_{ij}^{LR} \tag{2.117}$$

Equation (2.116) is interlaced, as M_{θ}^{b} is a function of the unity vector n_{ij}, defined in the direction of r_{ij}^{IP}, which in turn is a function of a. However, it can be easily solved iteratively:

- Since M_θ^b takes values between M_c^b and M_e^b, an initial value of $M_\theta^b\left(n_{ij}\right)=\left(M_c^b+M_e^b\right)/2$ can be used, so that a first estimate of a is computed from Equation (2.116).
- Next, r_{ij}^{IP} may be computed from Equation (2.112), allowing a more precise estimate of M_θ^b.
- Introducing this new value of M_θ^b into Equation (2.116) allows a more accurate estimate of a. This procedure may be continued iteratively until convergence. Experience from the application of this algorithm indicates that in most cases, convergence is achieved in less than 2-4 iterations.

Apart from reducing the size of the algorithm, and the number of equations involved, an important benefit from this modification is that the quantities $dr_{ij}dr_{ij}$, $dr_{ij}r_{ij}^{LR}$ and $r_{ij}^{LR}r_{ij}^{LR}$ that appear in Equation (2.116) need to be calculated only once. Therefore, the required computational effort is significantly reduced.

An even more important benefit from this algorithm is that the final estimate of M_θ^b may be stored into memory and used as an initial value for the next step's iterative procedure. As thoroughly explained in the previous paragraphs, the integration timestep in both FLAC and FLAC3D is restrained to very small values, in order to ensure the stability of the explicit finite difference solution scheme. Moreover, according to the model's mapping rule, the direction of the unit vector n_{ij} is only indirectly related to the current deviatoric stress ratio r_{ij}. As shown in Figure 2.5, the unit vector n_{ij} is associated with the direction of shearing ($r_{ij}-r_{ij}^{LR}$), and is therefore relatively insensitive to small changes in the current deviatoric stress ratio. As a result, the direction of the unit vector n_{ij} and the resulting value of $M_\theta^b\left(n_{ij}\right)$, are not expected to intensely fluctuate, during shearing. Therefore, the number of iterations needed for convergence is minimized and the computational efficiency is significantly increased.

2.6. Drift Correction

An important part of the constitutive model's integration scheme is the application of a drift correction algorithm, which ensures that the stress point does not move far outside the model's bounding surface. This correction becomes necessary due to the form of the adopted mapping rule, which was presented in the previous section. More specifically, if the current stress point lies far outside the bounding surface, it could become impossible to determine a conjugate image point.

Therefore, after each modification of the stress state, the distance from the bounding surface $F_{BS}(r_{ij})$ is computed, and consequently compared to a given tolerance value $F_{BS,tol}$. Following a sensitivity analysis, the tolerance value inherited in this work is equal to $F_{BS,tol}=10^{-2}$. If the distance is larger than this value, i.e. $F_{BS}(r_{ij}) > F_{BS,tol}$, the following drift correction algorithm is applied.

Step 1

The stress state is moved in the stress space, along the direction of the plastic potential derivative, i.e. $R_{ij} = \partial g / \partial \sigma_{ij}$:

$$\sigma_{ij}^{corr} = \sigma_{ij} + \Lambda\left(2G_t n_{ij} + K_t D\delta_{ij}\right) \tag{2.118}$$

where:

$$\Lambda = \frac{F_{BS}\left(r_{ij}\right)}{K_p + 2G_t + VK_t D} \tag{2.119}$$

Step 2

The result of the above correction is evaluated:

Case a: $F_{BS}(r_{ij}^{corr}) > F_{BS,tol}$

The corrected stress point is still far outside the bounding surface, thus the correction of Step 1 is repeated.

Case b: $F_{BS}(r_{ij}^{corr}) < 0$

The applied drift correction was larger than necessary, thus Step 1 is repeated, using $\Lambda' = 0.9\Lambda$.

Case c: $F_{BS}(r_{ij}^{corr}) < F_{BS,tol}$ and $F_{BS}(r_{ij}^{corr}) < 0$

The applied drift correction is accepted.

Chapter 3

Numerical methodology: Evaluation of performance

3.1. General

The numerical methodology presented in Chapter 2 is evaluated herein, in both element level and boundary value conditions. The accuracy of the addressed integration schemes was first assessed, through the development of isoerror maps. Their computational efficiency was also evaluated, through their application for a given undrained shear strain path and the comparison of the required computational times.

Consequently, the adopted constitutive model was calibrated against a wide range of resonant column, as well as monotonic and cyclic undrained simple shear and triaxial tests. Having achieved a good comparison between the experimental results and the respective numerical predictions, in element level, the accuracy of the developed numerical methodology in boundary value problems was evaluated in both 2- and 3-dimensions. This was achieved through the simulation of a well established centrifuge experiment, concerning the liquefaction performance of a shallow foundation, which will be the problem dealt with in the following chapters.

3.2. Accuracy of integration schemes

In the previous paragraphs, three different integration schemes have been adressed, namely the:

- Modified Euler integration with automatic sub-stepping and error control
- Modified Euler integration without sub-stepping and error control
- Single step Euler integration

In order to assess the accuracy of the above algorithms, and derive conclusions on their range of application, isoerror maps were developped. This procedure has been employed by a number of authors, e.g. Krieg & Krieg (1977), Schreyer, Kulak & Kramer (1979), Iwan & Yoder (1983), Ortiz & Popov (1985), Ortiz & Simo (1986) and Simo & Taylor (1986), as well as by Andrianopoulos (2006).

It must be noted, herein, that the combined integration scheme may not be evaluated using the isoerror maps procedure, as this procedure involves the accuracy evaluation of the integration algorithm over one single strain increment, while the developed scheme involves a sequence of increments.

The procedure for the creation of isoerror maps, is as follows:

- A minimum of three points in the stress space is selected, representing a wide range of possible stress states.
- A sequence of specified strain increments is applied to each selected point, and the integration algorithm is used for the computation of the corresponding stresses.
- The exact stresses for the prescribed strain increments are computed by repeatedly applying the algorithm with an increasing number of subincrements. The value for which further sub-incrementing produces no change in the numerical result is taken as the exact solution.
- Finally, results are reported as the relative root mean square of the error between the exact and computed solution, as obtained by Equation (3.1):

$$\delta = \frac{\sqrt{\left(\sigma_{ij} - \sigma_{ij}^{*}\right)\left(\sigma_{ij} - \sigma_{ij}^{*}\right)}}{\sqrt{\sigma_{ij}^{*}\sigma_{ij}^{*}}} \tag{3.1}$$

In the work presented herein, three different points in the stress space were examined. An initial void ratio of $e = 0.737$ was considered, corresponding to a relative density of $D_r = 40\%$. Starting from an initial isotropic pressure of $\sigma_v = \sigma_h = 80\text{kPa}$, the material was subjected to:

- undrained triaxial compression
- undrained triaxial extension
- undrained simple shear

More specifically, in the first case of triaxial compression, a vertical compressive strain of $\varepsilon_v = 0.01\%$ was applied to the specimen, accompanied by an equal and opposite horizontal strain of $\varepsilon_h = -0.01\%$, in order to achieve initial yielding. In the case of triaxial extension, the specimen was subjected to a vertical strain of $\varepsilon_v = -0.01\%$ and a horizontal strain of $\varepsilon_h = 0.01\%$. The application of these strains was performed incrementally, in 10.000 steps ($\Delta\varepsilon = 10^{-8}$). Finally, in order for the isoerror maps to be constructed, different combinations of vertical ($\Delta\varepsilon_v$) and horizontal ($\Delta\varepsilon_h$) strains were consequently applied, ranging from 10^{-5} to 10^{-3},.

In the third case, yielding was achieved by initially applying a shear strain of $\varepsilon_{vh} = 0.01\%$. Similar to the previous cases, shearing was applied under constant volume, in 10.000 steps ($\Delta\varepsilon = 10^{-8}$). At the final stage, different combinations of shear ($\Delta\varepsilon_{vh}$) and vertical ($\Delta\varepsilon_v$) strain were applied, ranging from 10^{-5} to 10^{-3}.

In all cases, the exact solutions were obtained by applying the stain increments in steps of $\Delta\varepsilon = 10^{-8}$, and using the Modified Euler integration scheme with automatic sub-stepping and error control, with an error tolerance value of $\text{STOL} = 10^{-5}$.

The above procedure was performed three times, corresponding to the different integration algorithms presented in the above. The resulting isoerror maps are shown in Figures 3.1 and 3.2.

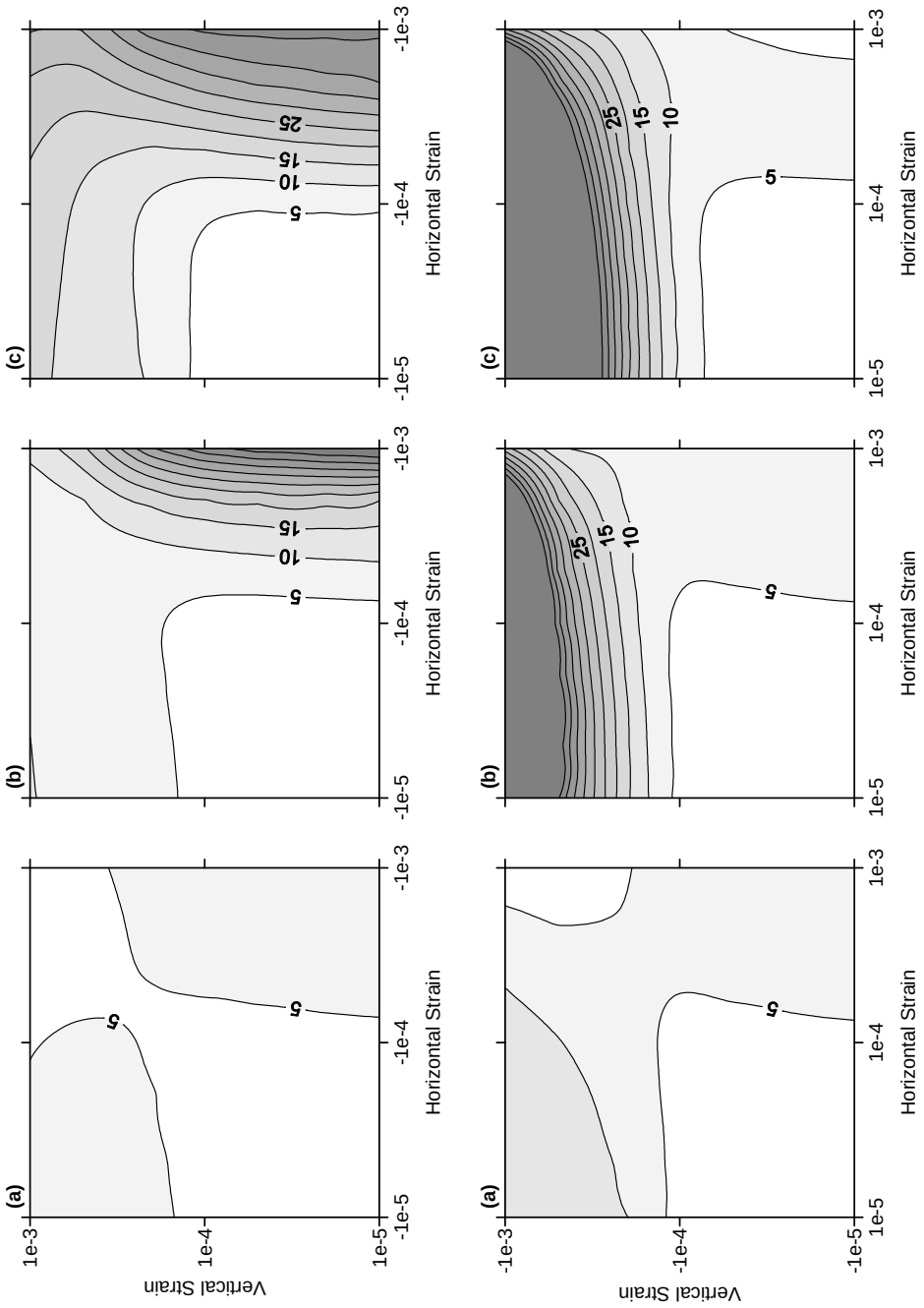

Figure 3.1. Isoerror maps for undrained triaxial compression and extension, created using (a) the Modified Euler integration scheme, with automatic sub-stepping and error control, (b) the Modified Euler scheme without substepping and error control and (c) the single-step Euler integration scheme.

Σχήμα 3.1. Ισοκαμπύλες σφάλματος για αστράγγιστη τριαξονική θλίψη και εφελκυσμό, θεωρώντας (a) τροποποιημένη ολοκλήρωση κατά Euler με αυτόματη υποδιαίρεση βήματος και έλεγχο σφάλματος, (b) τροποποιημένη ολοκλήρωση κατά Euler χωρίς υποδιαίρεση βήματος και (c) απλή ολοκλήρωση κατά Euler.

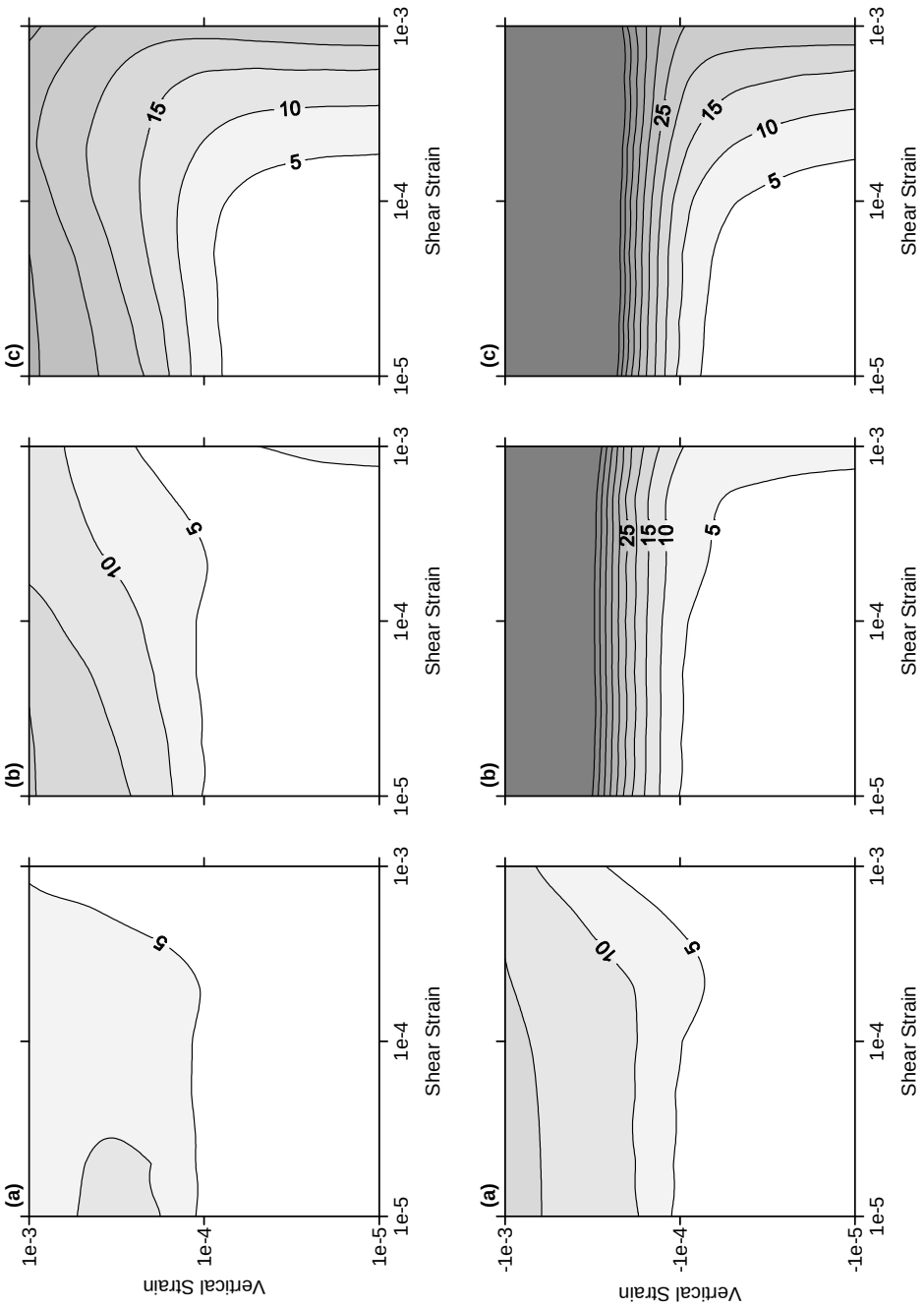

Figure 3.2. Isoerror maps for simple shear, created using (a) the Modified Euler integration scheme, with automatic sub-stepping and error control, (b) the Modified Euler scheme without substepping and error control and (c) the single-step Euler integration scheme.

Σχήμα 3.1. Ισοκαμπύλες σφάλματος για απλή διάτμηση, θεωρώντας (a) τροποποιημένη ολοκλήρωση κατά Euler με αυτόματη υποδιαίρεση βήματος και έλεγχο σφάλματος, (b) τροποποιημένη ολοκλήρωση κατά Euler χωρίς υποδιαίρεση βήματος και (c) απλή ολοκλήρωση κατά Euler.

Thorough observation of Figures 3.1 and 3.2 yields the following conclusions:

- As it was expected, the computed relative error increases with increasing strain increments, for all initial stress states and for all integration schemes.
- Relative error increases when large tensile strain increments are applied.
- The Modified Euler integration scheme with automatic sub-stepping and error control is proved to provide the most accurate results, with the relative error not exceeding 5 to 10%, even for the largest applied strain increments.
- Compared to the single step Euler integration scheme, the benefit from the application of the modified Euler algorithm without sub-stepping and error control, is proved to be relatively small. It should be taken into account that model computations in the modified Euler scheme are performed twice, and thus the single-step Euler scheme is expected to be twice as efficient.
- For strain increments smaller than 10^{-4}, all algorithms provide accurate results, with the relative error not exceeding 5%.

This last observation was incorporated into the combined integration scheme of the UDM code, by adding the restriction not to perform a single-step Euler integration, when the norm of the applied strain increment $\left\|\Delta\varepsilon_{ij}\right\| = \Delta\varepsilon_{ij}\Delta\varepsilon_{ij}$ is beyond a threshold strain value $ETOL$. This tolerance value was implemented as a UDM property and may be defined by the user. According to the above presented isoerror maps, this value should not be larger than 10^{-4}. However, taking into account that these maps do not cover the whole range of possible stress states and strain increments, a smaller default value of 10^{-5} was conservatively selected.

Therefore, the implemented combined integration scheme, features the following parameters:

- A strain threshold value $ETOL$: when the norm of the strain increment is beyond this value, then the modified Euler scheme with automatic error control and substepping is applied. In other words, if $ETOL = 0$, then the previously presented combined integration scheme is bypassed. For larger values, the integration scheme selection depends on the values of $MSTOL$ and $STOL$.

- An error tolerance value MSTOL, which defines whether the single-step integration turns to a modified Euler integration scheme. If large values of both MSTOL and ETOL are selected (i.e. 10^3), then the integration scheme reduces to single-step Euler integration.
- An error tolerance value STOL, which defines whether the automatic substepping algorithm is turned on. It becomes evident that in order for automatic error control and substepping to be applied, small values of ETOL and MSTOL must be selected, so that the modified Euler scheme is used.

In order to explain the use of the above parameters, Table 3.1 shows how different integration schemes may applied, using the appropriate values for ETOL, MSTOL and STOL.

Table 3.1. Typical values for parameters ETOL, MSTOL and STOL, used for the application of different integration schemes.

Πίνακας 3.1. Τυποκές τιμές των παραμέτρων ETOL, MSTOL και STOL που χρησιμοποιούνται για την εφαρμογή του κάθε σχήματος ολοκλήρωσης.

Integration Scheme	ETOL	MSTOL	STOL
Modified Euler, with error control & substepping	0	0	10^{-3}
Modified Euler, without error control & substepping	0	0	10^{3}
Combined scheme, with error control & substepping	10^{-4}	10^{-3}	10^{-3}
Combined scheme, without error control & substepping	10^{-4}	10^{-3}	10^{3}
Single step Euler	10^{3}	10^{3}	10^{3}

Evaluation of the overall accuracy and computational efficiency of the UDM, with the use of different combinations for these parameters, will be presented in the following.

3.3. Computational efficiency of integration algorithms

The computational efficiency of all algorithms presented previously is evaluated herein, through their application in the prediction of stresses, for a given undrained shear strain path, in element level. More specifically, an initial void ratio of $e = 0.737$ was considered, corresponding to a relative density of $D_r = 40\%$, while the initial vertical and horizontal stresses were equal to $\sigma_v = 80\text{KPa}$ and $\sigma_h = 36\text{KPa}$ respectively, corresponding to a horizontal earth pressure coefficient of $K_o = 0.45$. The element was subjected to the shear strain γ_{vh} path shown in Figure 3.3. The prescribed strain path was applied in increments of $\Delta\gamma_{vh} = 10^{-4}$ and 10^{-5}, which are typical for FLAC and FLAC3D numerical analyses. Plane strain conditions were considered, while no volume change was allowed ($\varepsilon_v = \varepsilon_h = 0$).

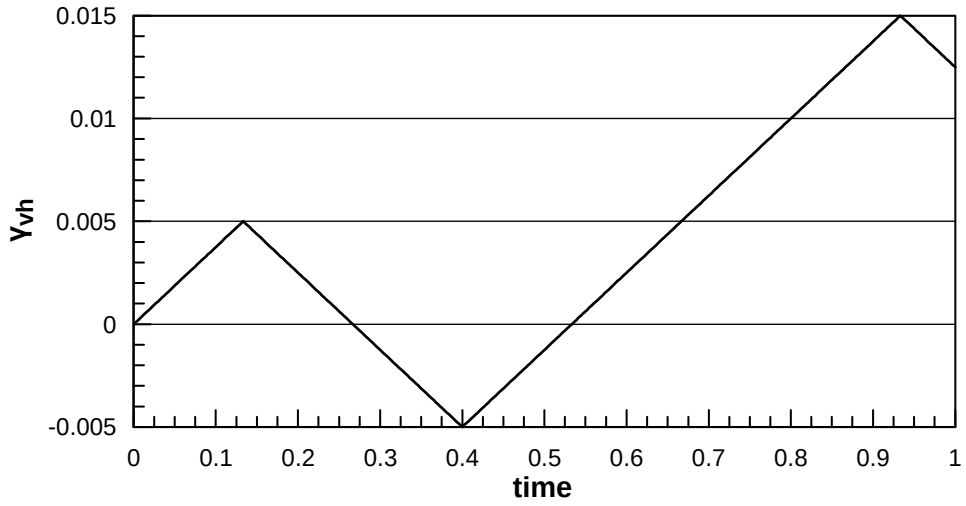

Figure 3.3. Applied shear strain history.

Σχήμα 3.3. Επιβαλόμενη χρονοϊστορία διατμητικών παραμορφώσεων.

The analyses were performed in both FLAC and FLAC3D (Figure 3.4). The results from all cases a-d shown in Figure 3.4 were identical, thus confirming the model's implementation in the multi-axial stress space. In the following figures, only results from the 2-dimensional element tests are shown.

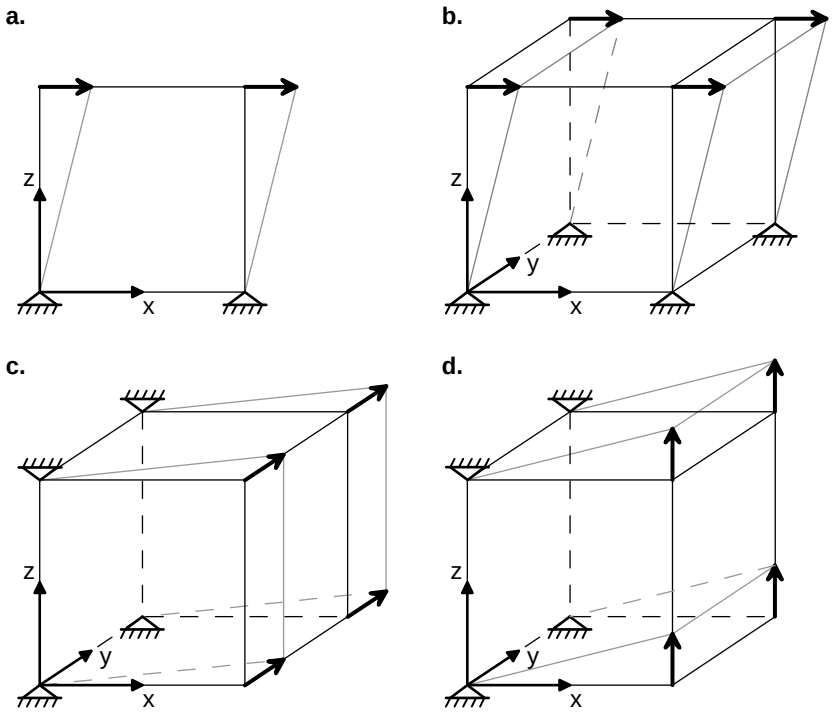

Figure 3.4. Applied boundary conditions in (a) FLAC, and (b-d) FLAC3D.

Σχήμα 3.4. Επιβαλόμενες συνοριακές συνθήκες στους κώδικες (a) FLAC και (b-d) FLAC3D.

More specifically, the following cases were examined:

i. Original UDM, by Andrianopoulos (2006), programmed in FISH.

ii. The same UDM, reprogrammed using C++.

iii. Optimized C++ UDM code, without any algorithm modifications. The modified Euler integration scheme with automatic error control and substepping was applied (i.e. $\mathrm{ETOL}=0$, $\mathrm{MSTOL}=0$ and $\mathrm{STOL}=10^{-3}$).

iv. Similar to case iii, though using the new algorithm for the application of the mapping rule, with $\left(\mathrm{M}_{\mathrm{c}}^{\mathrm{b}}+\mathrm{M}_{\mathrm{e}}^{\mathrm{b}}\right)/2$ as an initial value for the involved iterative procedure.

v. Similar to case iii, though using the new algorithm for the application of the mapping rule, with a constantly upgrading initial value of $\mathrm{M}_{0}^{\mathrm{b}}$, for the involved iterative procedure.

vi. Similar to case v, though using the modified Euler integration scheme, without substepping and error control (i.e. $\mathrm{ETOL}=0$, $\mathrm{MSTOL}=0$ and $\mathrm{STOL}=10^{3}$).

vii. Similar to case v, though using the combined integration scheme, with automatic substepping and error control where necessary (i.e. $\mathrm{ETOL}=10^{3}$, $\mathrm{MSTOL}=10^{-3}$ and $\mathrm{STOL}=10^{-3}$).

viii. Similar to case v, though using the combined integration scheme, without substepping and error control (i.e. $\mathrm{ETOL}=10^{3}$, $\mathrm{MSTOL}=10^{-3}$ and $\mathrm{STOL}=10^{3}$).

ix. Similar to case v, though using the single-step Euler integration scheme (i.e. $\mathrm{ETOL}=10^{3}$, $\mathrm{MSTOL}=10^{3}$ and $\mathrm{STOL}=10^{3}$).

As described in the above, analyses i to v were performed in order to assess the increase in computational efficiency, which was achieved by reprogramming the UDM in C++, rearranging and optimizing the code, and improving the algorithm for the application of the model's mapping rule. As expected, the results from all these analyses are identical. The resulting shear stress vs. vertical stress path, shear stress vs. shear strain relationship and excess pore pressure vs. shear strain relationship are presented in Figure 3.5.

As it may be observed in this figure, the results from analyses i to v were identical. However, significant differences were obseved, in terms of computational effort. Table 3.2 shows the average computational time required to perform the UDM computations, per zone and per timestep, in the above cases, with the prescribed shear strain path being applied in increments of $\Delta\gamma_{vh}=10^{-4}$ and 10^{-5}. These times were measured in a Personal Computer with an 3.0 GHz Intel Pentium Processor and 1GB of RAM. The analyses were performed using the 2-dimensional code FLAC. The corresponding computational time in FLAC3D is increased by an average of 150%, as model computations in FLAC3D are performed ten times per zone, compared to the four subzones used in FLAC.

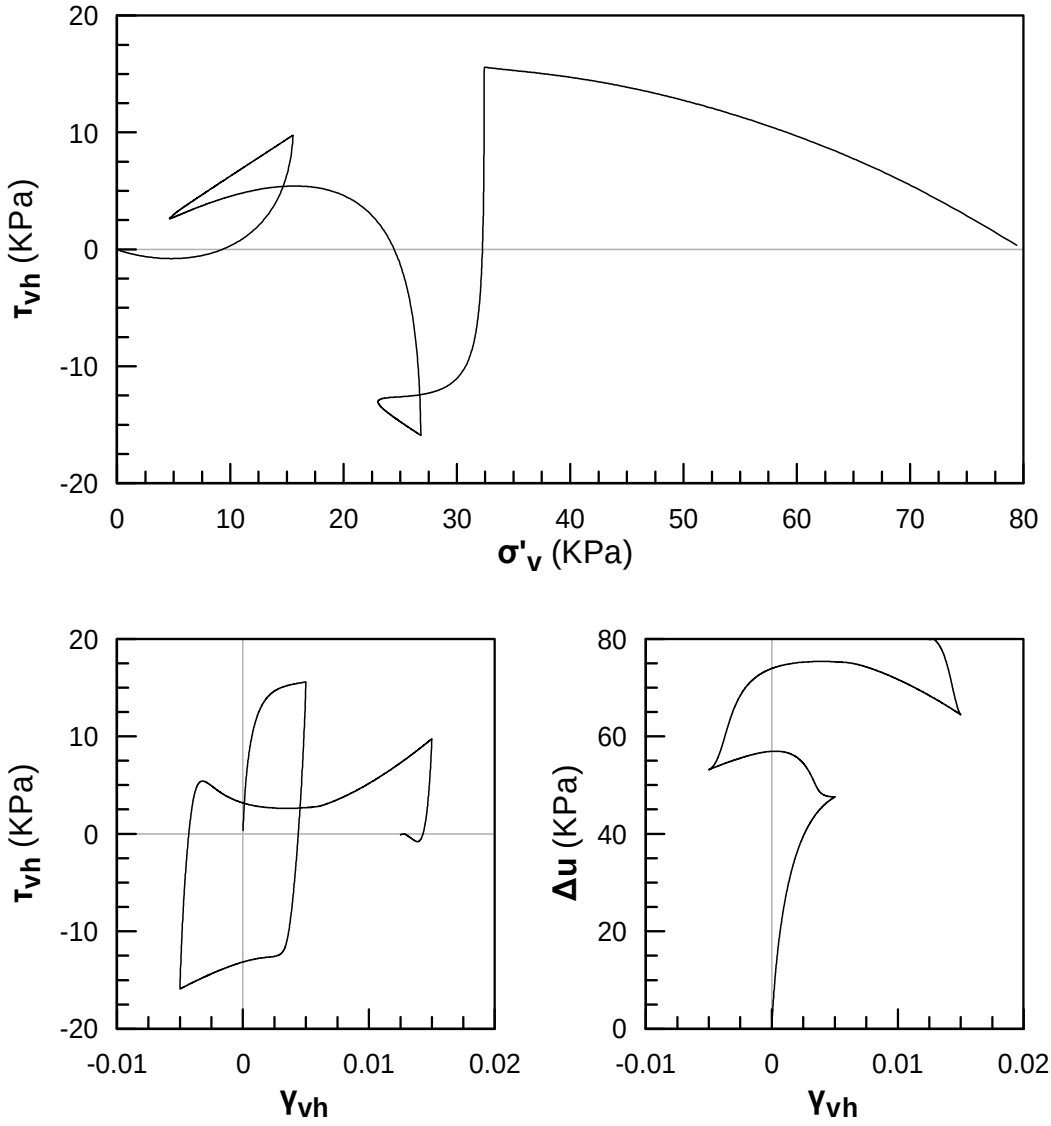

Figure 3.5. Results of element tests i to v, in terms of shear stress vs. vertical stress path, shear stress vs. shear strain relationship and excess pore pressure vs. shear strain relationship.

Σχήμα 3.5. Αποτελέσματα δοκιμών i έως v, σε όρους διαδρομής διατμητικής τάσης προς κατακόρυφη τάση, σχέσης διατμητικής τάσης προς διατμητική παραμόρφωση και σχέσης υπερ-πίεσης πόρων προς διατμητική παραμόρφωση.

Observation of the computational time values presented in Table 3.2 yields the following conclusions:

- A significant decrease of the average computational time is observed for all cases, when the strain path is applied using smaller increments. This is due to

the smaller average number of substeps required to maintain the integration error within the allowable tolerance values.

- Regardless of the applied strain increment, the C++ written UDM performs at least 3 times faster than the one written in FISH. This does not imply that the total analysis time in boundary value problems will be reduced to 1/3. The computational times presented herein involve the UDM performance alone, while in a FLAC analysis, an important amount of computational time is consumed for other purposes, independent of the UDM, such as the solution and integration of the equations of motion, the derivation of strain rates from gridpoint velocities and groundwater flow associated calculations.
- Comparison between cases ii and iii indicates that rearrangement and optimization of the C++ code resulted in a computational efficiency increase of about 10%.
- As shown in cases iii and iv, the new algorithm for the application of the model's mapping rule speeds up the UDM by 12%.
- Comparison between cases iv and v indicates that the use of a constantly upgrading initial value of M_{θ}^{b} in the iterative procedure for the application of the model's mapping rule, reduces the computational time by another 12% in the case of $\Delta\gamma_{vh} = 10^{-4}$, and by 16% for $\Delta\gamma_{vh} = 10^{-5}$. The higher increase of computational efficiency in the case of smaller strain increments is justified by the fact that the direction of the unity vector n_{ij}, as well as the resulting bounding surface radius M_{θ}^{b}, do not intensely fluctuate during subsequent timesteps and, consequently, the required number of iterations is minimized.

Table 3.2. Comparison of the computational efficiency for cases i to v, with the prescribed strain path being applied using different increment sizes.

Πίνακας 3.2. Σύγκριση υπολογιστικού χρόνου στις περιπτώσεις i έως v, για διαφορετικά βήματα επιβολής της προδιαγεγραμμένης χρονοϊστορίας παραμόρφωσης.

Case Number & Description		**Average computational time per zone and per timestep (in μs)**	
		$\Delta\gamma_{vh} = 10^{-4}$	$\Delta\gamma_{vh} = 10^{-5}$
i	FISH compiled UDM	≈ 7500	≈ 2000
ii	C++ compiled UDM	2350	620
iii	Optimized UDM code	2139	561
iv	New mapping rule algorithm	1879	494
v	Constantly upgrading M_θ^b	1620	416

Analyses v to ix were performed to assess the increase in computational efficiency achieved by the application of different computation schemes. As expected, simplifications in the integration algorithm have a negative effect on the accuracy of predicted stresses. This effect is evaluated through comparison with the higher accuracy algorithm, that is the modified Euler scheme with automatic substepping and error control (Case v). More specifically, a relative error measure was computed for each case, as shown in Equation (3.2):

$$\text{R.E.} = \sqrt{\frac{\left(\Delta\sigma'_{ij} - \Delta\sigma'^{(v)}_{ij}\right)\left(\Delta\sigma'_{ij} - \Delta\sigma'^{(v)}_{ij}\right)}{\sigma'^{(v)}_{ij}\sigma'^{(v)}_{ij}}} \qquad (3.2)$$

The resulting shear stress vs. vertical stress path, shear stress vs. shear strain relationship and excess pore pressure vs. shear strain relationship for cases v to ix are presented in Figures 3.6 and 3.7, with the strain path being applied at increments of $\Delta\gamma_{vh} = 10^{-4}$ and $\Delta\gamma_{vh} = 10^{-5}$ respectively. Time histories of shear strain, shear stress, vertical effective stress and the error measure of Equation (3.2) are shown in Figures 3.8 and 3.9. Finally, the average computational time required to perform the UDM computations, per zone and per timestep, is presented for each case in Table 3.3.

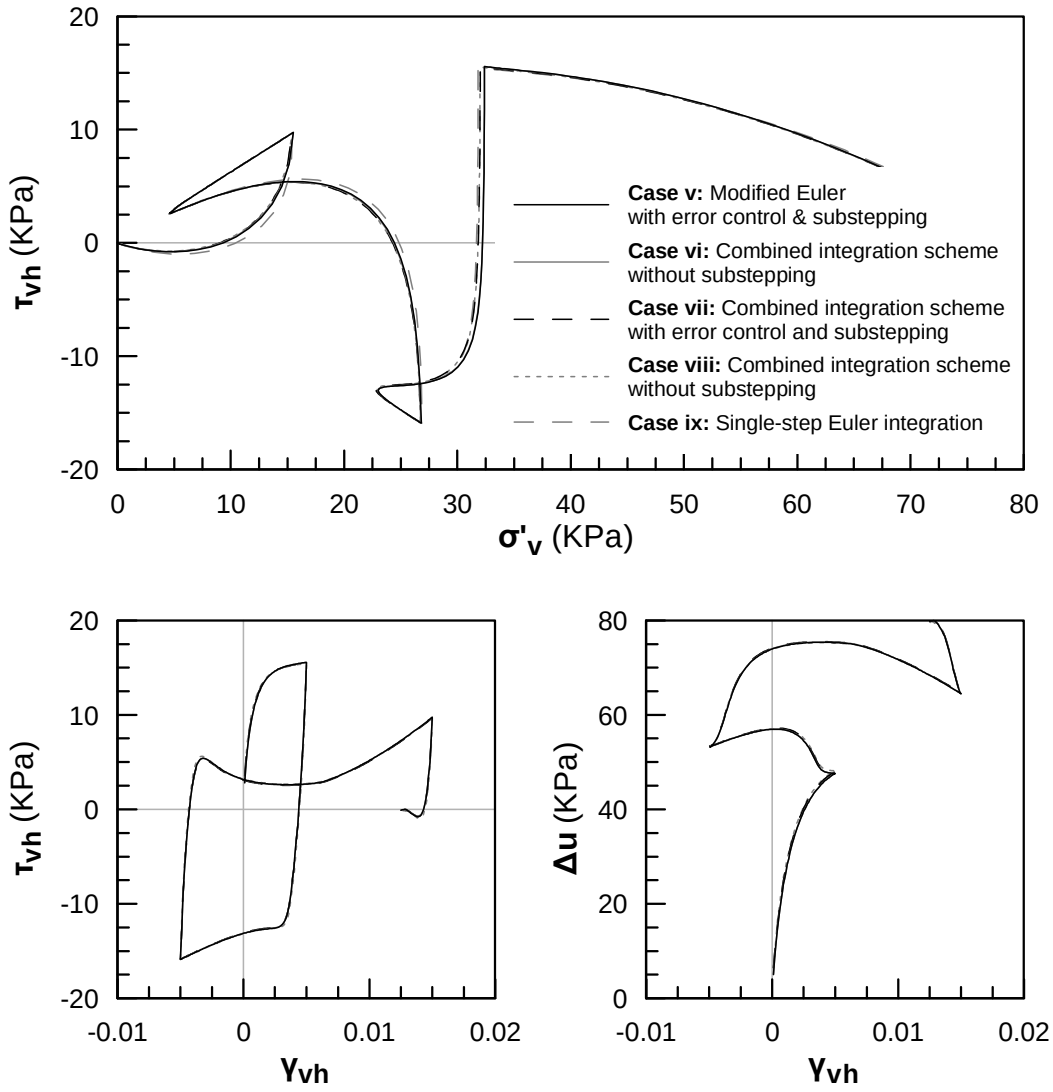

Figure 3.6. Results of element tests v to ix, in terms of shear stress vs. vertical stress path, shear stress vs. shear strain relationship and excess pore pressure vs. shear strain relationship, for applied strain increments of $\Delta\gamma_{vh} = 10^{-4}$.

Σχήμα 3.6. Αποτελέσματα δοκιμών v έως ix, σε όρους διαδρομής διατμητικής τάσης προς κατακόρυφη τάση, σχέσης διατμητικής τάσης προς διατμητική παραμόρφωση και σχέσης υπερ-πίεσης πόρων προς διατμητική παραμόρφωση, όταν η διατμητική παραμόρφωση επιβάλλεται σε βήματα $\Delta\gamma_{vh} = 10^{-4}$.

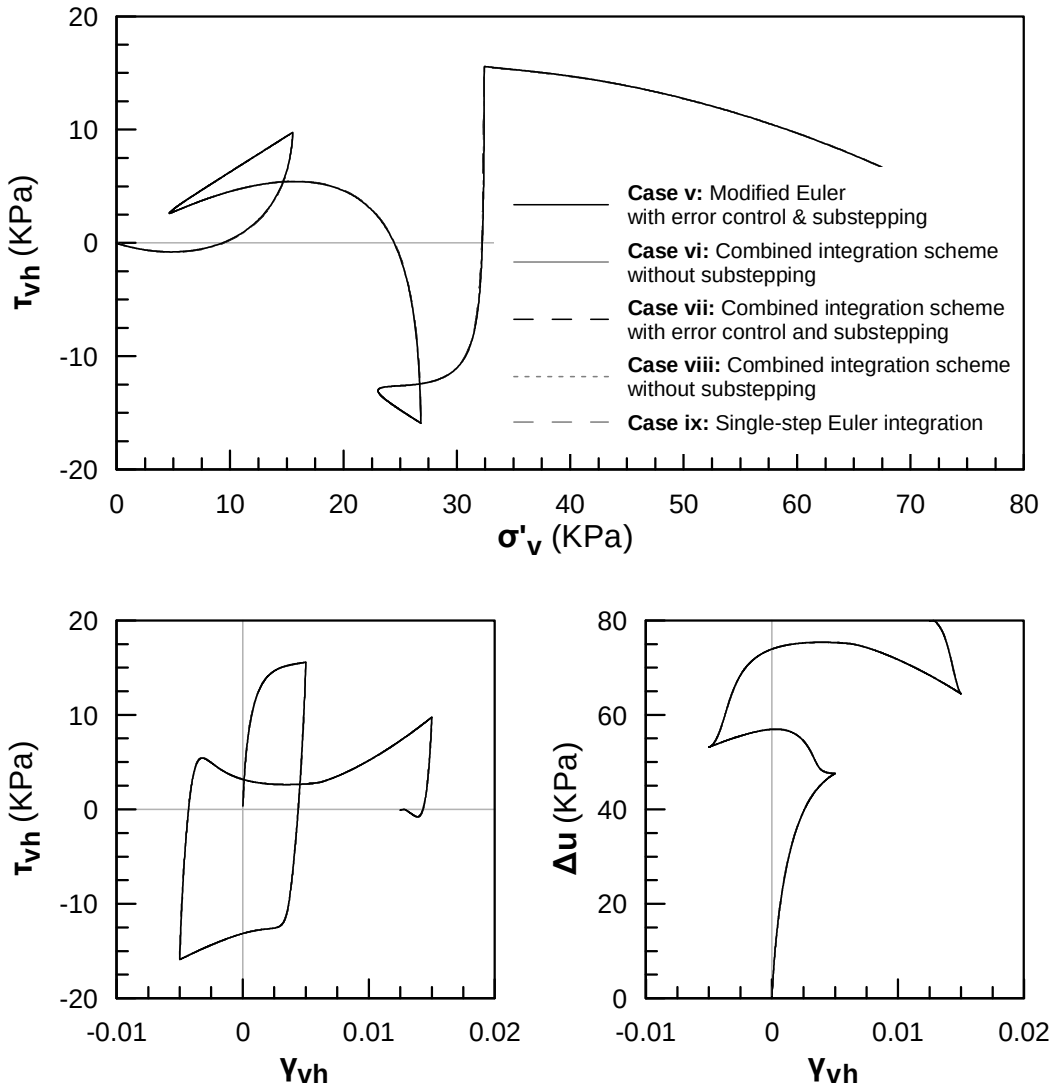

Figure 3.7. Results of element tests v to ix, in terms of shear stress vs. vertical stress path, shear stress vs. shear strain relationship and excess pore pressure vs. shear strain relationship, for applied strain increments of $\Delta\gamma_{vh} = 10^{-5}$.

Σχήμα 3.7. Αποτελέσματα δοκιμών v έως ix, σε όρους διαδρομής διατμητικής τάσης προς κατακόρυφη τάση, σχέσης διατμητικής τάσης προς διατμητική παραμόρφωση και σχέσης υπερ-πίεσης πόρων προς διατμητική παραμόρφωση, όταν η διατμητική παραμόρφωση επιβάλλεται σε βήματα $\Delta\gamma_{vh} = 10^{-5}$.

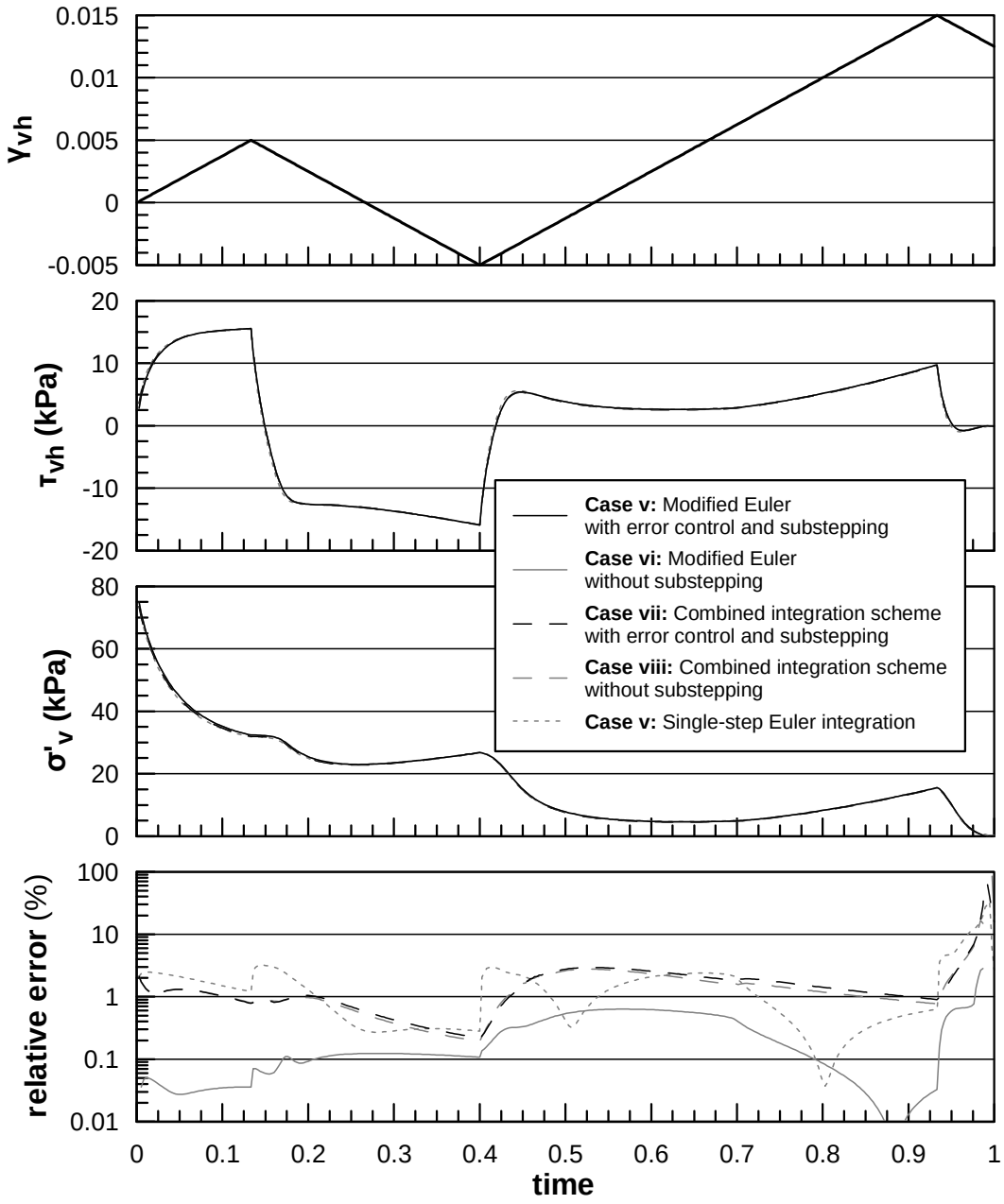

Figure 3.8. Results of element tests v to ix, in terms of shear strain, shear stress, vertical effective stress and error time histories, for applied strain increments of $\Delta\gamma_{vh} = 10^{-4}$.

Σχήμα 3.8. Αποτελέσματα δοκιμών v έως ix, σε όρους χρονοϊστοριών διατμητικής παραμόρφωσης, διατμητικής τάσης, κατακόρυφης ενεργού τάσης και σχετικού σφάλματος, όταν η διατμητική παραμόρφωση επιβάλλεται σε βήματα $\Delta\gamma_{vh} = 10^{-4}$.

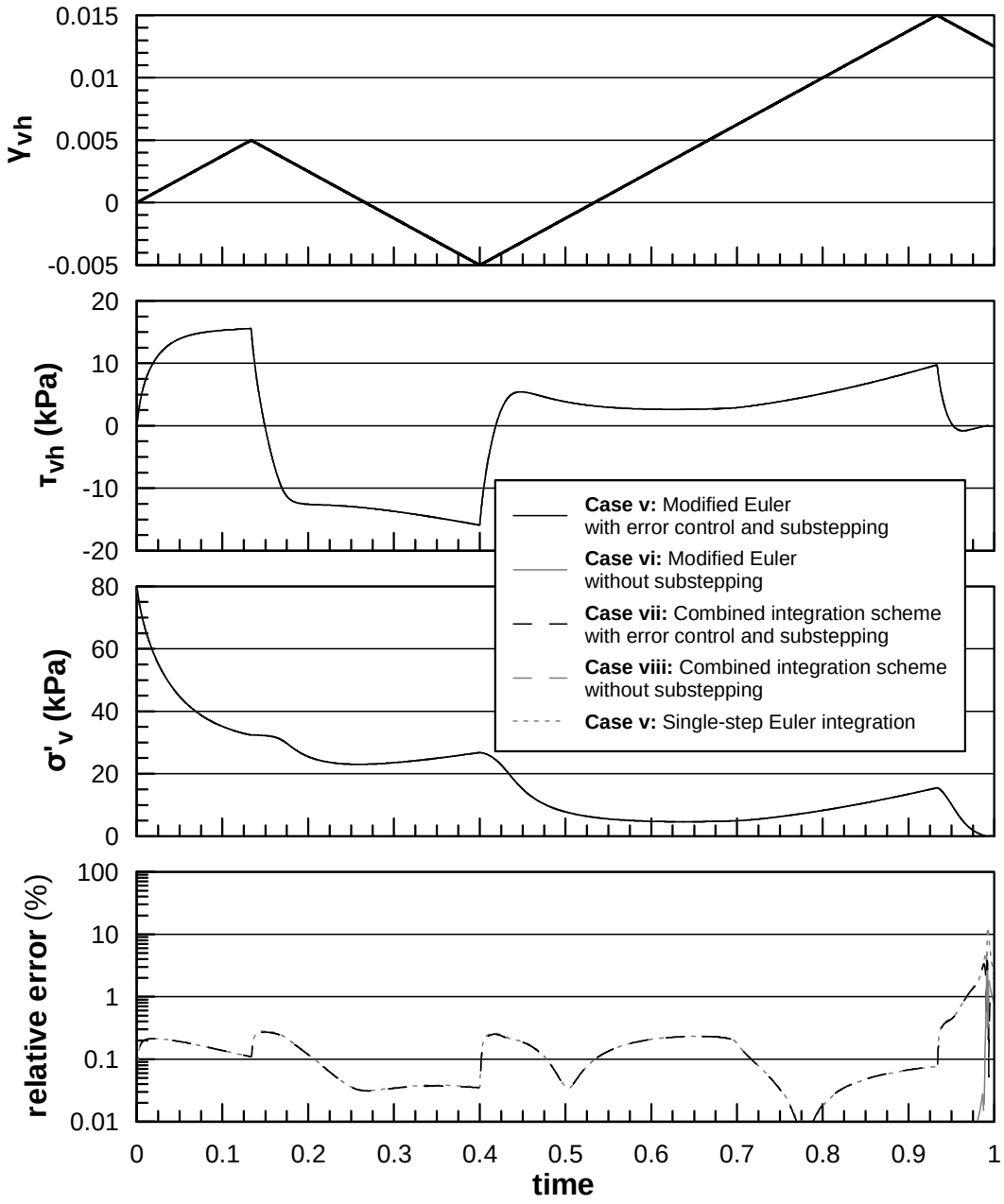

Figure 3.9. Results of element tests v to ix, in terms of shear strain, shear stress, vertical effective stress and error time histories, for applied strain increments of $\Delta\gamma_{vh} = 10^{-5}$.

Σχήμα 3.9. Αποτελέσματα δοκιμών v έως ix, σε όρους χρονοϊστοριών διατμητικής παραμόρφωσης, διατμητικής τάσης, κατακόρυφης ενεργού τάσης και σχετικού σφάλματος, όταν η διατμητική παραμόρφωση επιβάλλεται σε βήματα $\Delta\gamma_{vh} = 10^{-5}$.

Table 3.3. Comparison of the computational efficiency for cases v to ix, with the prescribed strain path being applied using different increment sizes.

Πίνακας 3.3. Σύγκριση υπολογιστικού χρόνου στις περιπτώσεις v έως ix, για διαφορετικά βήματα επιβολής της προδιαγεγραμμένης χρονοϊστορίας παραμόρφωσης.

Case Number & Description		**Computational time per zone and per timestep (in μs)**	
		$\Delta\gamma_{vh} = 10^{-4}$	$\Delta\gamma_{vh} = 10^{-5}$
v	Modified Euler with error control and substepping	1620	416
vi	Modified Euler without substepping	355	342
vii	Combined integration scheme with error control and substepping	306	215
viii	Combined integration scheme without substepping	234	199
ix	Single step Euler integration	202	197

Observation of Figures 3.6 to 3.9 as well as Table 3.3, yields the following conclusions:

- Comparison between computational times for applied strain increments of $\Delta\gamma_{vh} = 10^{-4}$ and $\Delta\gamma_{vh} = 10^{-5}$ indicates that effective integration algorithms (cases v, vii and viii), where either the integration scheme or the number of substeps depends on the estimated local error, the UDM performs much faster, as the strain increment decreases. However, smaller strain incremens also affect the computational times in cases vi and ix, where the integration algorithm does not include any form of error control. This is due to the algorithm used for the application of the mapping rule, as the application of smaller strain increments minimizes the number of iterations.

- Bypassing the automatic error control and substepping procedure, considerably increases computational efficiency, especially for larger applied strain increments, as shown by comparison of cases v and vi, or cases vii and viii. However, a significant increase in computational error is also observed. This error increases when the stress path enters specific regions of highly non-linear behavior. More specifically, peaks in the computed error are observed when the dilation surface is crossed, and the model approaches the critical

state. In liquefaction related boundary value problems, behavior is expected to be highly non-linear, thus bypassing error control should not be recommended.

- On the other hand, a significant decrease of computational time is also observed when the combined integration algorithm is applied. More specifically, computational time in case vii remains between cases v and ix. However, even though the local error in case ix is significantly increased, the combined integration algorithm seems to effectively switch to the higher order scheme when highly non-linear behavior is observed, thus minimizing the computational error.

As described above, the combined integration algorithm which allows to switch between single step Euler integration and modified Euler integration with error control, provides increased computational efficiency, without any major sacrifice in accuracy, and may be therefore recommended for use in boundary value problems. The use of this new integration scheme, together with the reprogramming of the original code of Andrianopoulos et al (2008) into C++, the consequent code optimization and the modifications in the algorithm for the application of the mapping rule, resulted in a total decrease of computational time, of the order of 90%! In other words, as shown from the comparison between cases i and vii, the developed UDM executes at 1/10 (one tenth) of the initial computational time, without any significant loss in the accuracy of the predictions. It should be stressed out that this computational time is increased by 150% for applications in FLAC3D, due to the different discretization of elements into a larger number of subzones. However, the improved computational efficiency of the new UDM, allows the performance of both 2-D and 3-D finite difference analyses, in rational times, which would not be possible with the original non-optimized code.

3.4. Model calibration

The model parameters were been calibrated against the results of tests performed during the VELACS research program (Arulmoli et al., 1992). These tests have been performed on Nevada sand #120, with the physical characteristics presented in Table 3.4, and the gradation curve of Figure 3.10. More specifically, the calibration was based on resonant column tests, as well as on monotonic and cyclic undrained simple shear and triaxial tests. These tests cover a wide range of initial relative density ($D_r = 40-60\%$), and initial consolidation stress ($40-160\text{kPa}$). Thus, they can be considered adequate for quantifying the behavior of the sand in terms of shear modulus reduction and damping increase with increasing shear strain, as well as the rate of excess pore pressure development and liquefaction resistance.

Table 3.4. Summary of Nevada Sand physical characteristics.

Πινακας 3.4. Σύνοψη φυσικών χαρακτηριστικών της Άμμου Nevada.

Density of grains (ρ_s)	$2.67\,\text{Mgr}/\text{m}^3$
Maximum dry density ($\rho_{dry,max}$)	$1.77\,\text{Mgr}/\text{m}^3$
Minimum dry density ($\rho_{dry,min}$)	$1.41\,\text{Mgr}/\text{m}^3$
Maximum void ratio (e_{max})	0.887
Minimum void ratio (e_{min})	0.511

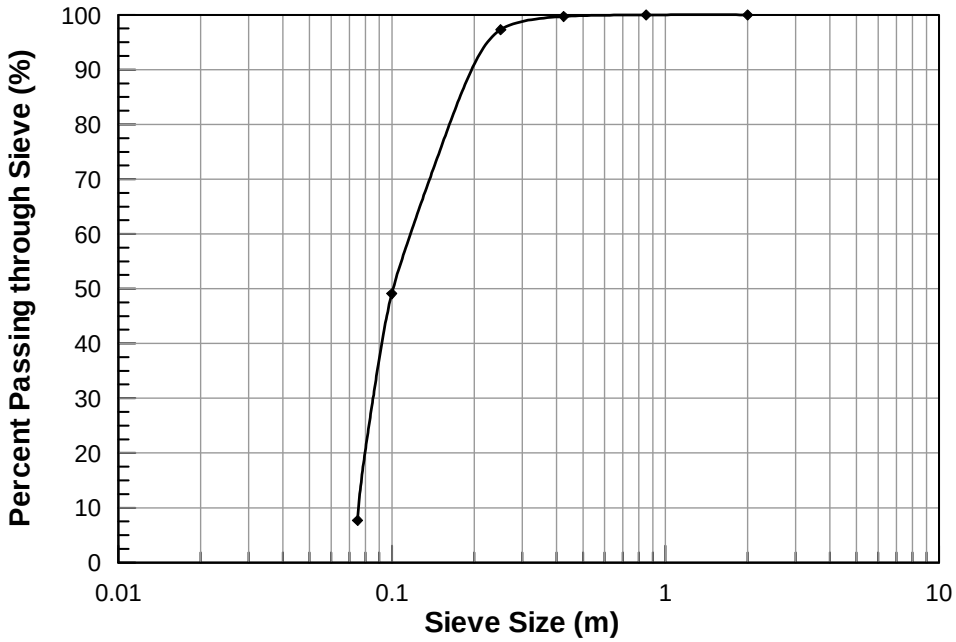

Figure 3.10. Gradation curve of Nevada Sand #120.

Σχήμα 3.10. Καμπύλη κοκκομετρικής διαβάθμισης της Άμμου Nevada #120.

The procedures which were followed in order to select the model parameters are covered extensively in Papadimitriou (1999, 2001, 2002) and Andrianopoulos (2006). The parameters which were finally incorporated to the present thesis, are shown in Table ??.

Table 3.5. Constitutive model parameters for Nevada Sand #120.

Πίνακας 3.5. Παράμετροι καταστατικού προσομοιώματος για την Άμμο Nevada #120.

Parameter	**Parameter Name used in FLAC & FLAC3D**	**Value**
M_c^c	mc_comp	1.25
M_e^c	mc_ext	0.90
$(e_{cs})_a$	void_cr	0.809
λ	lamda	0.022
B	m_b	600 *(180 for monotonic loading)*
ν	m_poiss	0.33
k_c^b	kb_comp	1.45
k_e^b	kb_ext	1.044
k_c^d	kd_comp	0.30

k_e^d	kd_ext	0.216
γ_1	m_g1	0.00025
a_1	m_a1	0.6 *(1.0 for monotonic loading)*
A_o	ao	0.8
h_o	ho	15000
H_o	ho_fab	40000

Figures 3.11 to 3.20 summarize the comparison between experimental results and numerical predictions:

- More specifically, Figure 3.11 compares experimental results and model predictions in terms of maximum shear modulus G_{max} variation with applied isotropic pressure p, for relative densities $D_r = 40\%$ and 60%.
- Figure 3.12 concerns shear modulus degradation G/G_{max} and damping ξ increase with increasing cyclic shear strain amplitude γ_{cyc}. In order to demonstrate the contribution of the Ramberg-Osgood formulation and the effect of plasticity on the model's behaviour, the above curves were also obtained using $a_1 = 1.0$ (which essentially turns off the Ramberg-Osgood formulation for the computation of elastic strains), as well as with a large value for h_o (which essentially turns plastic strains equal to zero).
- Finally, Figures 3.13 to 3.20 show the comparison between experimental results and model predictions, in terms of excess pore pressure ratio r_u generation rate, as well as in terms of liquefaction curves, in both dynamic simple shear and triaxial tests, with initial effective consolidation stresses (vertical and isotropic, respectively) equal to 80 and 160kPa, and relative densities of $D_r = 40\%$ and 60%.

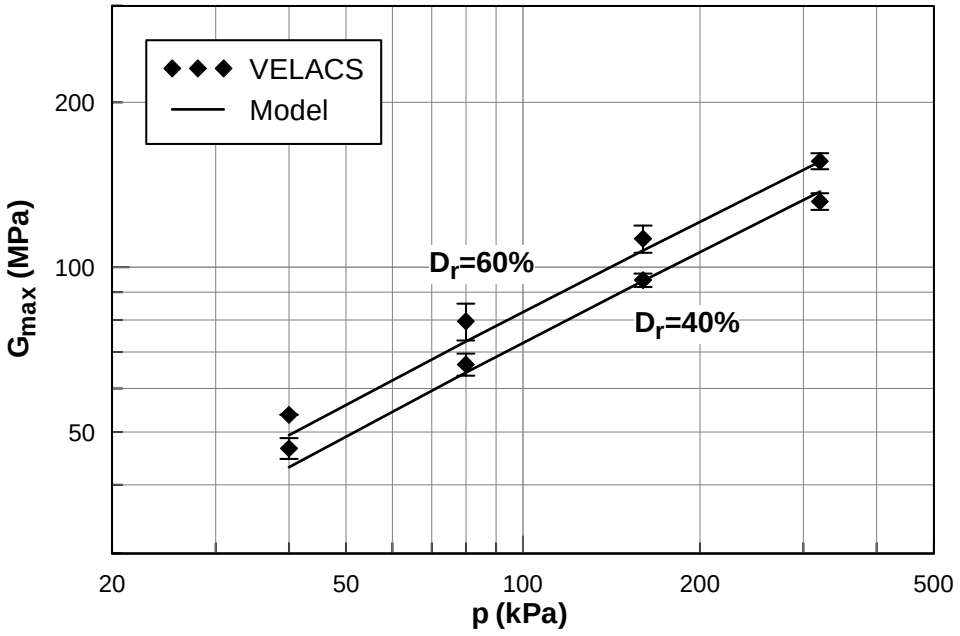

Figure 3.11. Comparison between experimental results and model predictions in terms of maximum shear modulus G_{max} variation with applied isotropic pressure p, for relative densities $D_r = 40\%$ and 60%.

Σχήμα 3.11. Σύγκριση πειραματικών αποτελεσμάτων και προβλέψεων καταστατικού προσομοιώματος σε όρους μεταβολής του μέγιστου μέτρου διάτμησης G_{max} με την επιβαλλόμενη μέση τάση p, για τιμές της σχετικής πυκνότητας $D_r = 40\%$ και 60%.

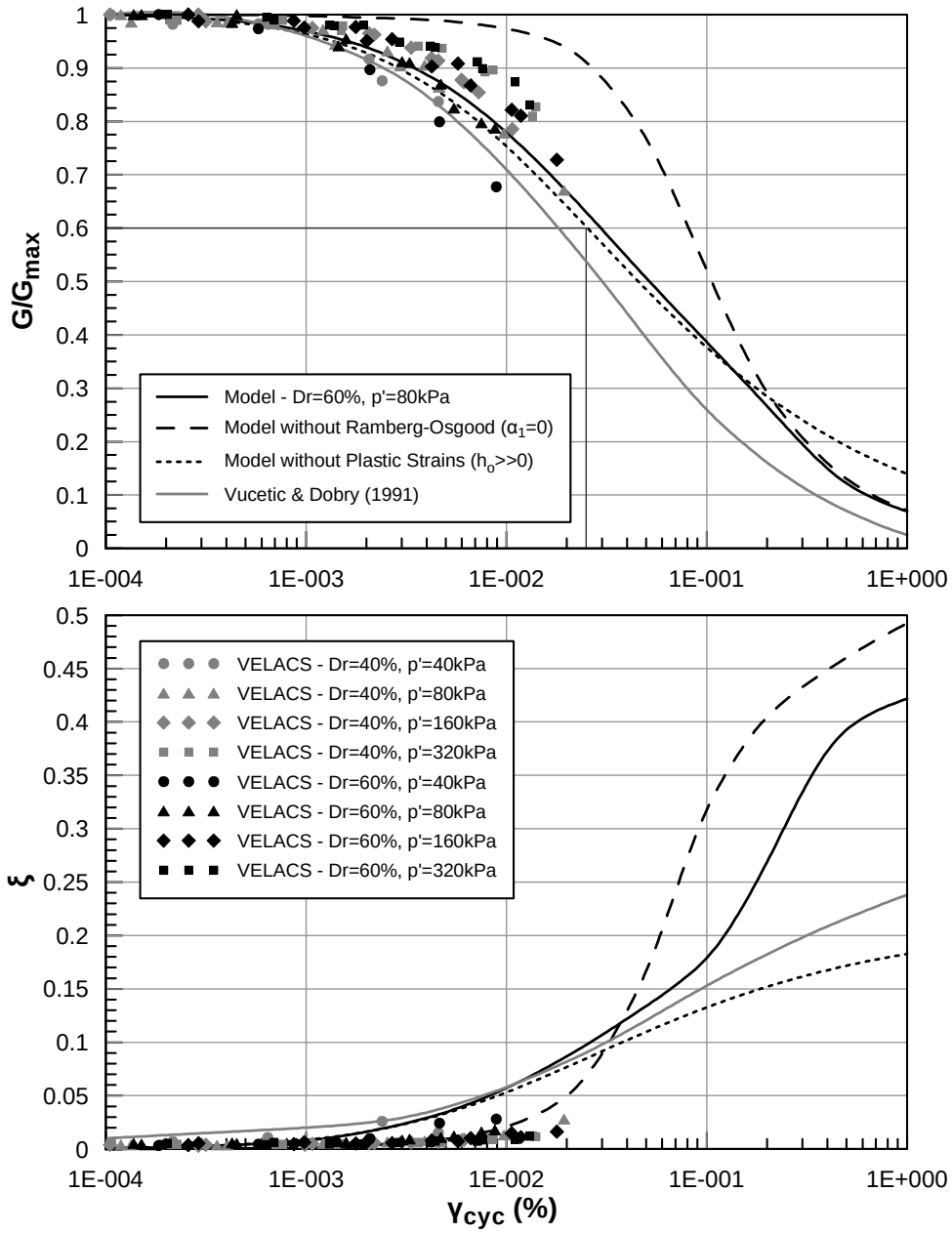

Figure 3.12. Comparison between experimental results and model predictions in terms of shear modulus degradation G/G_{max} and damping ξ increase with increasing cyclic shear strain amplitude γ_{cyc}.

Σχήμα 3.12. Σύγκριση πειραματικών αποτελεσμάτων και προβλέψεων καταστατικού προσομοιώματος σε όρους απομείωσης του κανονικοποιημένου μέτρου διάτμησης G/G_{max} και αύξησης της απόσβεσης ξ με το αυξανόμενο πλάτος της επιβαλλόμενης ανακυκλικής διατμητικής παραμόρφωσης γ_{cyc}.

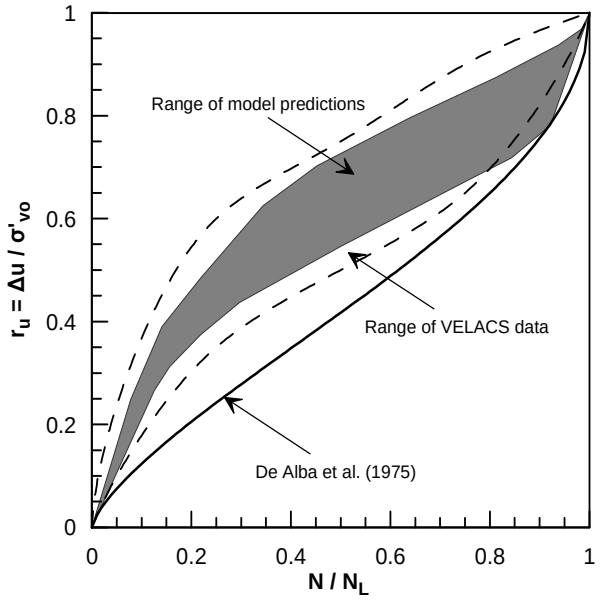

Figure 3.13. Comparison between experimental results and model predictions in terms of excess pore pressure ratio r_u generation rate, in dynamic simple shear tests, for relative density $D_r = 60\%$.

Σχήμα 3.13. Σύγκριση πειραματικών αποτελεσμάτων και προβλέψεων καταστατικού προσομοιώματος σε όρους ρυθμού ανάπτυξης υπερπιέσεων πόρων r_u σε ανακυκλικές δοκιμές απλής διάτμησης, για σχετική πυκνότητα $D_r = 60\%$.

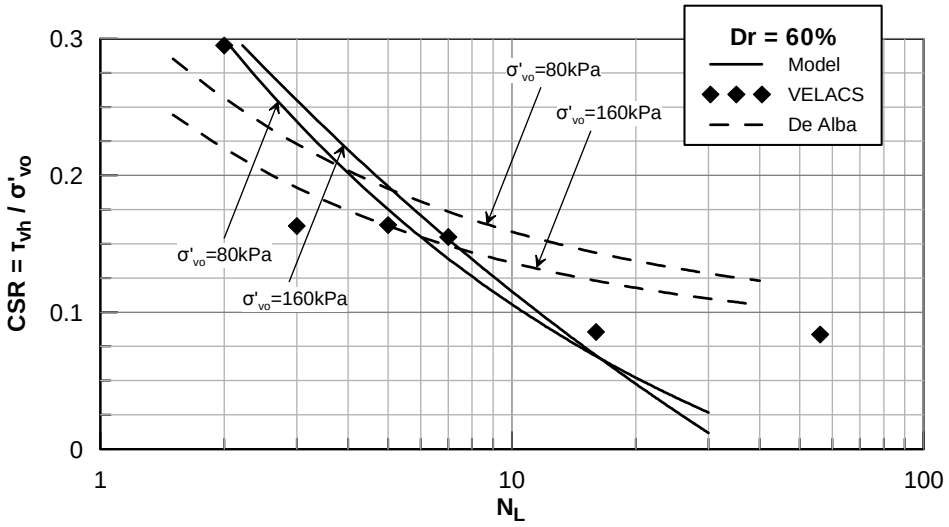

Figure 3.14. Comparison between experimental and model predicted liquefaction curves, derived from dynamic simple shear tests, at relative density $D_r = 60\%$.

Σχήμα 3.14. Σύγκριση πειραματικών αποτελεσμάτων και προβλέψεων καταστατικού προσομοιώματος σε όρους καμπύλων ρευστοποίησης από ανακυκλικές δοκιμές απλής διάτμησης, για σχετική πυκνότητα $D_r = 60\%$.

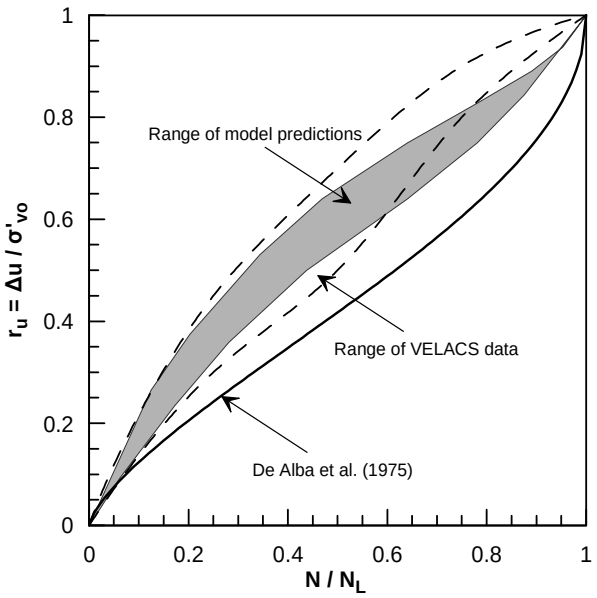

Figure 3.15. Comparison between experimental results and model predictions in terms of excess pore pressure ratio r_u generation rate, in dynamic simple shear tests, for relative density $D_r = 40\%$.

Σχήμα 3.15. Σύγκριση πειραματικών αποτελεσμάτων και προβλέψεων καταστατικού προσομοιώματος σε όρους ρυθμού ανάπτυξης υπερπιέσεων πόρων r_u σε ανακυκλικές δοκιμές απλής διάτμησης, για σχετική πυκνότητα $D_r = 40\%$.

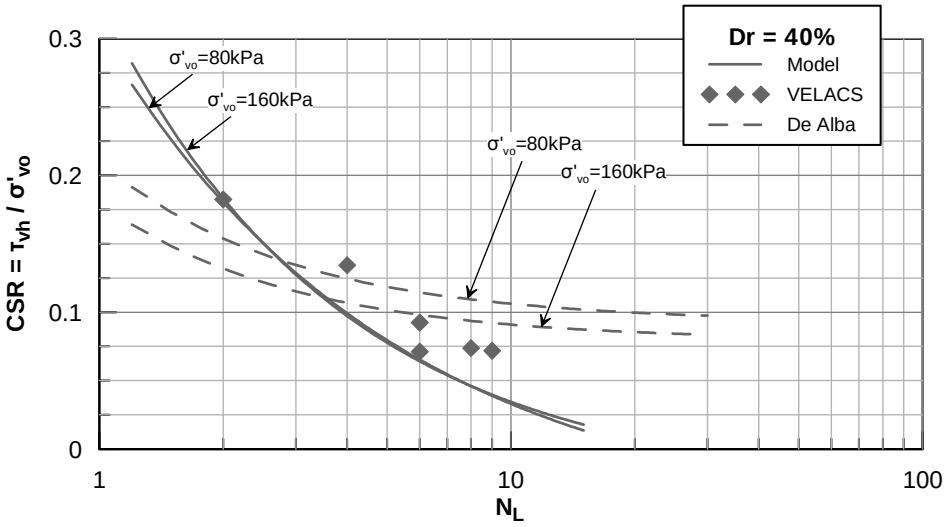

Figure 3.16. Comparison between experimental and model predicted liquefaction curves, derived from dynamic simple shear tests, at relative density $D_r = 40\%$.

Σχήμα 3.16. Σύγκριση πειραματικών αποτελεσμάτων και προβλέψεων καταστατικού προσομοιώματος σε όρους καμπύλων ρευστοποίησης από ανακυκλικές δοκιμές απλής διάτμησης, για σχετική πυκνότητα $D_r = 40\%$.

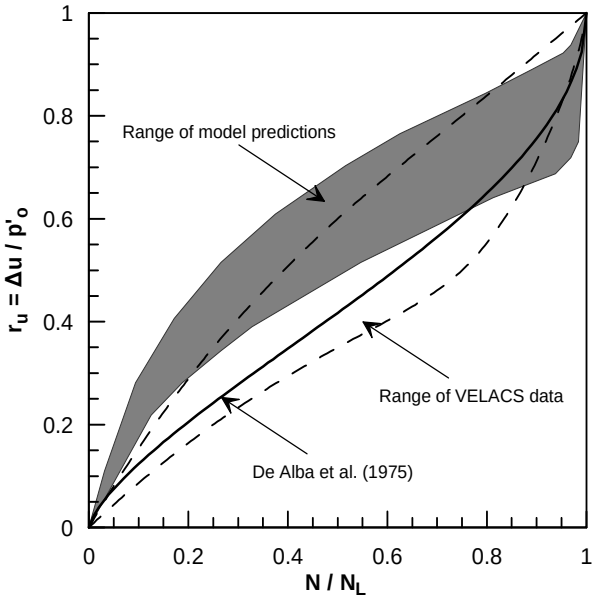

Figure 3.17. Comparison between experimental results and model predictions in terms of excess pore pressure ratio r_u generation rate, in dynamic triaxial tests, for relative density $D_r = 60\%$.

Σχήμα 3.17. Σύγκριση πειραματικών αποτελεσμάτων και προβλέψεων καταστατικού προσομοιώματος σε όρους ρυθμού ανάπτυξης υπερπιέσεων πόρων r_u σε ανακυκλικές τριαξονικές δοκιμές, για σχετική πυκνότητα $D_r = 60\%$.

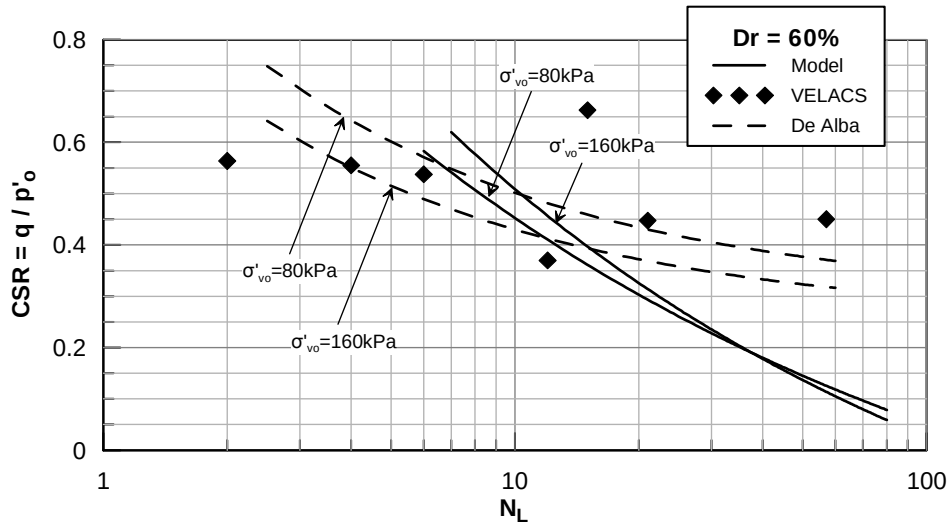

Figure 3.18. Comparison between experimental and model predicted liquefaction curves, derived from dynamic triaxial tests, at relative density $D_r = 60\%$.

Σχήμα 3.18. Σύγκριση πειραματικών αποτελεσμάτων και προβλέψεων καταστατικού προσομοιώματος σε όρους καμπύλων ρευστοποίησης από ανακυκλικές τριαξονικές δοκιμές, για σχετική πυκνότητα $D_r = 60\%$.

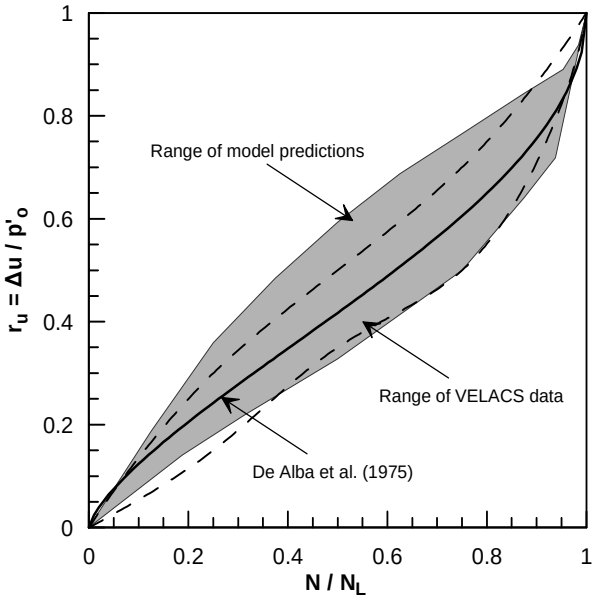

Figure 3.19. Comparison between experimental results and model predictions in terms of excess pore pressure ratio r_u generation rate, in dynamic triaxial tests, for relative density $D_r = 40\%$.

Σχήμα 3.19. Σύγκριση πειραματικών αποτελεσμάτων και προβλέψεων καταστατικού προσομοιώματος σε όρους ρυθμού ανάπτυξης υπερπιέσεων πόρων r_u σε ανακυκλικές τριαξονικές δοκιμές, για σχετική πυκνότητα $D_r = 40\%$.

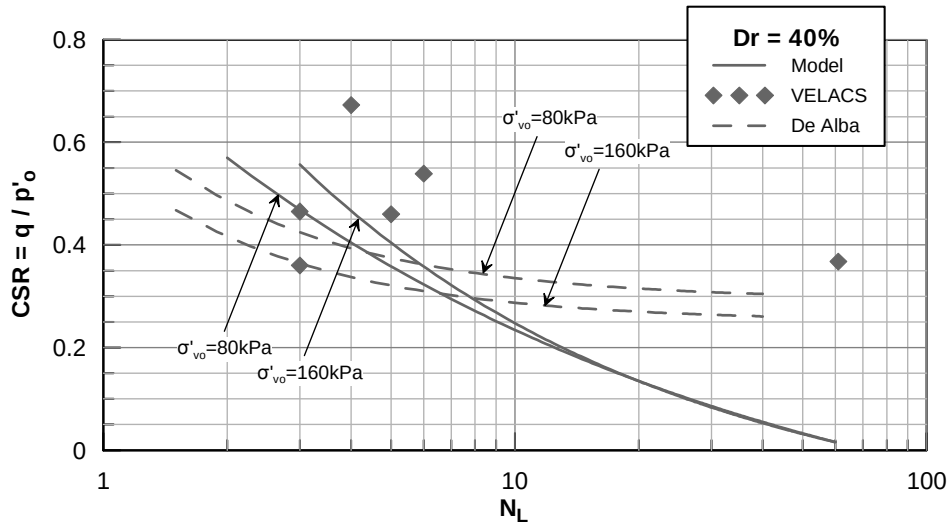

Figure 3.20. Comparison between experimental and model predicted liquefaction curves, derived from dynamic triaxial tests, at relative density $D_r = 40\%$.

Σχήμα 3.20. Σύγκριση πειραματικών αποτελεσμάτων και προβλέψεων καταστατικού προσομοιώματος σε όρους καμπύλων ρευστοποίησης από ανακυκλικές τριαξονικές δοκιμές, για σχετική πυκνότητα $D_r = 40\%$.

3.5. Application – verification in boundary value problems

In order to verify the model's accuracy and performance, a number of analyses were performed, simulating a well established centrifuge experiment, namely the Model 12 performed during the VELACS research project (Arulmoli et al., 1992, Arulanandan & Scott, 1994). The selection of this test is directly related to the problem investigated in the following chapters, that is, the dynamic response of a surface foundation, resting on liquefiable soil. Moreover, the 3-dimensional nature of the experiment allows to evaluate the capabilities of the 2-D, but also the 3-D numerical methodology developed herein.

3.5.1. Experiment Results

Model No12 was tested in a rigid box, with a plan area of 28×13m in prototype scale. The model consists of a 6m deep sand layer, overlaid by a 1m thick silt layer. Nevada sand #120 and Bonnie Silt were used as soil. The sand was pluviated through a raining device, from a constant height which was calibrated to obtain a relative density of 60%. A 4m high structure was placed in the center of the sample, applying a bearing pressure of 150KPa on a surface of 3×3m, 0.5m below the surface of the sand layer. The structure model was made out of an aluminium container, filled with lead shoot in order to achieve the desired pressure. Water was used as pore fluid, with the water table being 1m above the surface of the silt. The target input motion for the test was 10 cycles of 2Hz sine wave, with an amplitude of 0.25g, while the experiment was performed at a centrifuge acceleration level of 100g. Finally, soil-structure behavior was monitored via 4 accelerometers (AccB, AccC, AccD and AccF), 4 pressure transducers (PPT1 to PPT4) and 1 LVDT, placed as shown in Figure 3.21.

As far as model construction is concerned, the sand layer was placed first, with pluviation interrupted four times, in order to install accelerometers, pressure transducers, as well as the structure. Next, the bucket was sealed and vacuum was applied to the sample. Water was subjected to the vacuum amd drawn into the testing container. Finally, Silt was poured on the top of the sand and spread to cover the entire sand layer. The experiment was performed at a centrifugal acceleration of 100g. The sample was first left in flight for approximately 10 minutes. Following the consolidation process, the centrifuge was stopped and the structure was checked for

standing. The centrifuge was again spun up to 100g and the test was performed after the pore pressure transducers had stabilized.

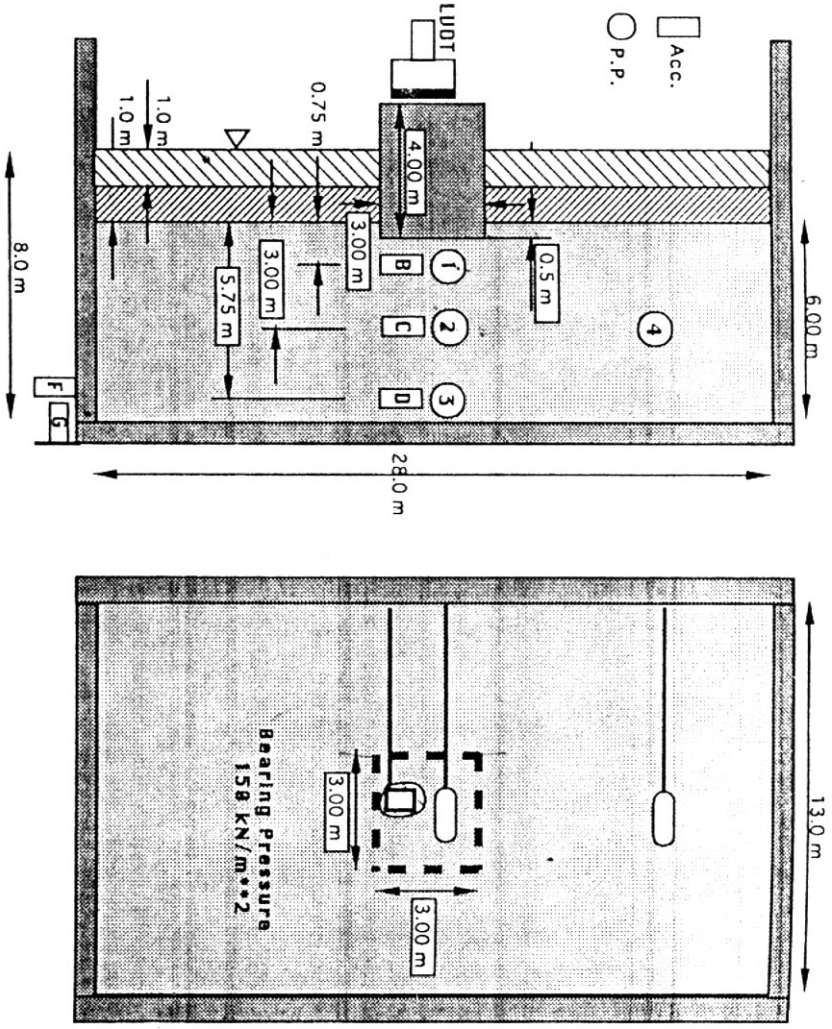

Figure 3.21. VELACS Model 12 centrifuge test setup.

Σχήμα 3.21. Διάταξη πειράματος φυγοκεντριστή VELACS Model 12.

Model Test No12 was duplicated several times, in three different Universities, namely Princeton University (six times, I to VI), University of California at Davis (U.C. Davis) and Reanseller Polytechnical Institute (R.P.I.). Results of Tests II and IV of Princeton University are not available due to problems with instrumentation malfunction, while Test III had a higher excitation level of 0.35g, instead of the prescribed 0.25g. Moreover, not all pore pressure time histories are available from a single test, as an average of one pressure transducer malfunctioned during each test. Despite the above difficulties, good overall repeatability was observed between the

available recordings, in terms of acceleration. However, there was a scatter in the recorded foundation settlements, which ranged from 21 to 27cm at the end of shaking. The test was duplicated in R.P.I., where three identical tests were performed, with similar results being reached in each trial. Therefore, the resulting value of 13cm for the foundation settlements, may be regarded as more reliable than the ones recorded in Princeton University. Acceleration and pore pressure time histories were more or less similar to the ones recorded in Princeton. Finally, in U.C. Davis, the input motion amplitude was similar to Princeton Test III, with an average of 0.33g and a maximum of 0.37g, and are therefore not presented herein.

Figure 3.22 shows the recorded results in terms of excess pore pressure ratios $\Delta u/\sigma'_{v,o}$, where Δu is the excess pore water pressure and $\sigma'_{v,o}$ is the initial vertical effective stress. It may be observed that in the position of the transducer PPT4, excess pore pressure ratios reach values larger than 0.9, indicating that liquefaction occurred in the free field. However, underneath the footing, excess pore ratios remain significantly lower, implying that the presence of the superstructure inhibited liquefaction. As a result, no significant deamplification was observed in the respective acceleration recordings, which are shown in Figure 3.23.

The final foundation settlements are presented for all tests in Table 3.6. Larger foundation settlements were recorded in test III of Princeton University, as well as in the test performed in U.C.Davis. This may be attributed to the larger amplitudes of the applied acceleration. The evolution of foundation settlements for the tests performed with the originally prescribed acceleration amplitude of 0.25g is shown in Figure 3.24.

Table 3.6. Recorded foundation settlements in VELACS Model 12 centrifuge experiments.

Πίνακας 3.6. Καταγεγραμμένες καθιζήσεις θεμελίων στα πειράματα φυγοκεντριστή VELACS Model 12.

University	Test	Settlement (cm)
Princeton	I	27
	III	47
	V	22
	VI	21
U.C. Davis	-	18
R.P.I.	I, II & III	13

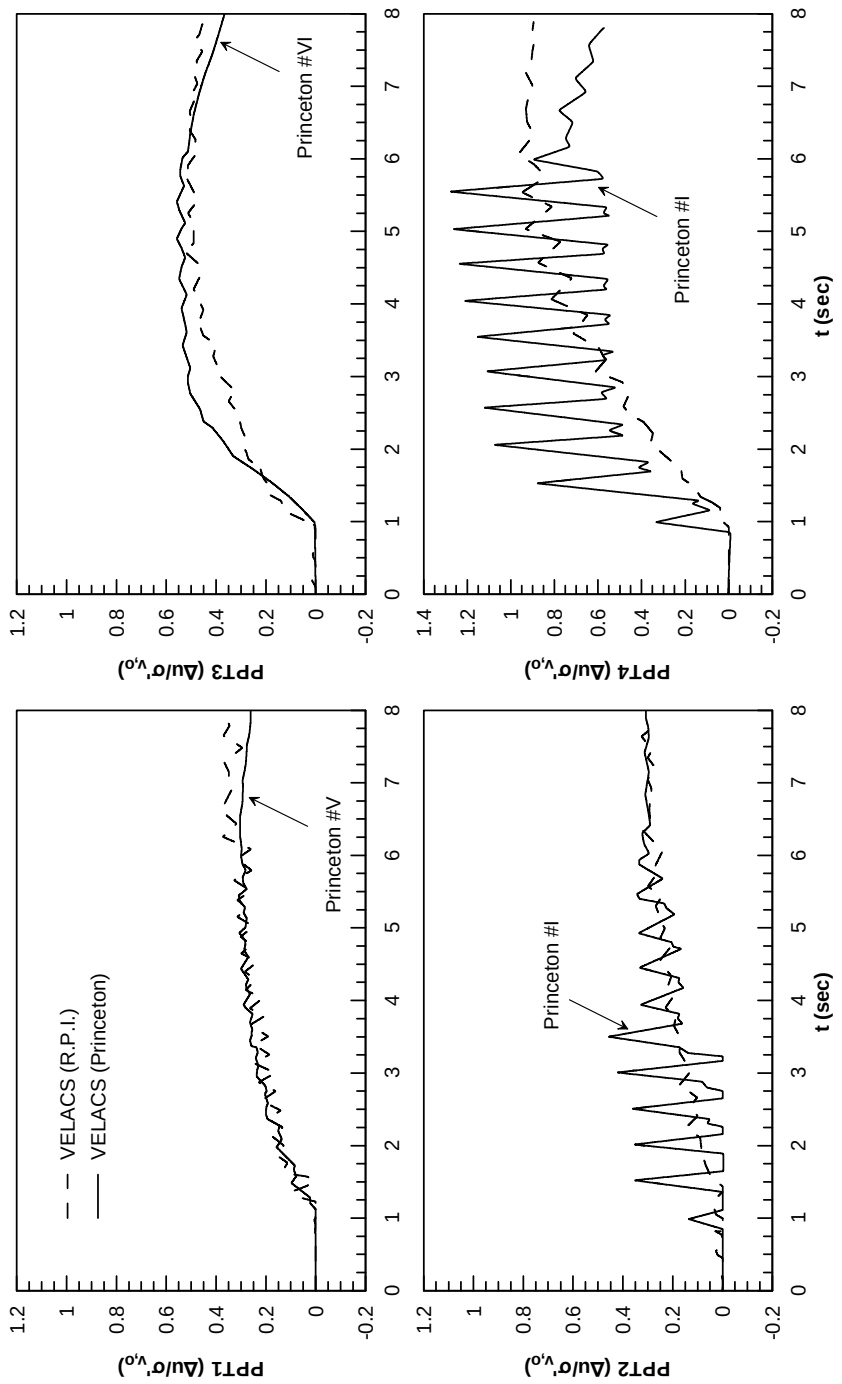

Figure 3.22. Recorded time histories of excess pore pressure ratios.

Σχήμα 3.22. Καταγεγραμμένες χρονοϊστορίες λόγων υπερπιέσεων πόρων.

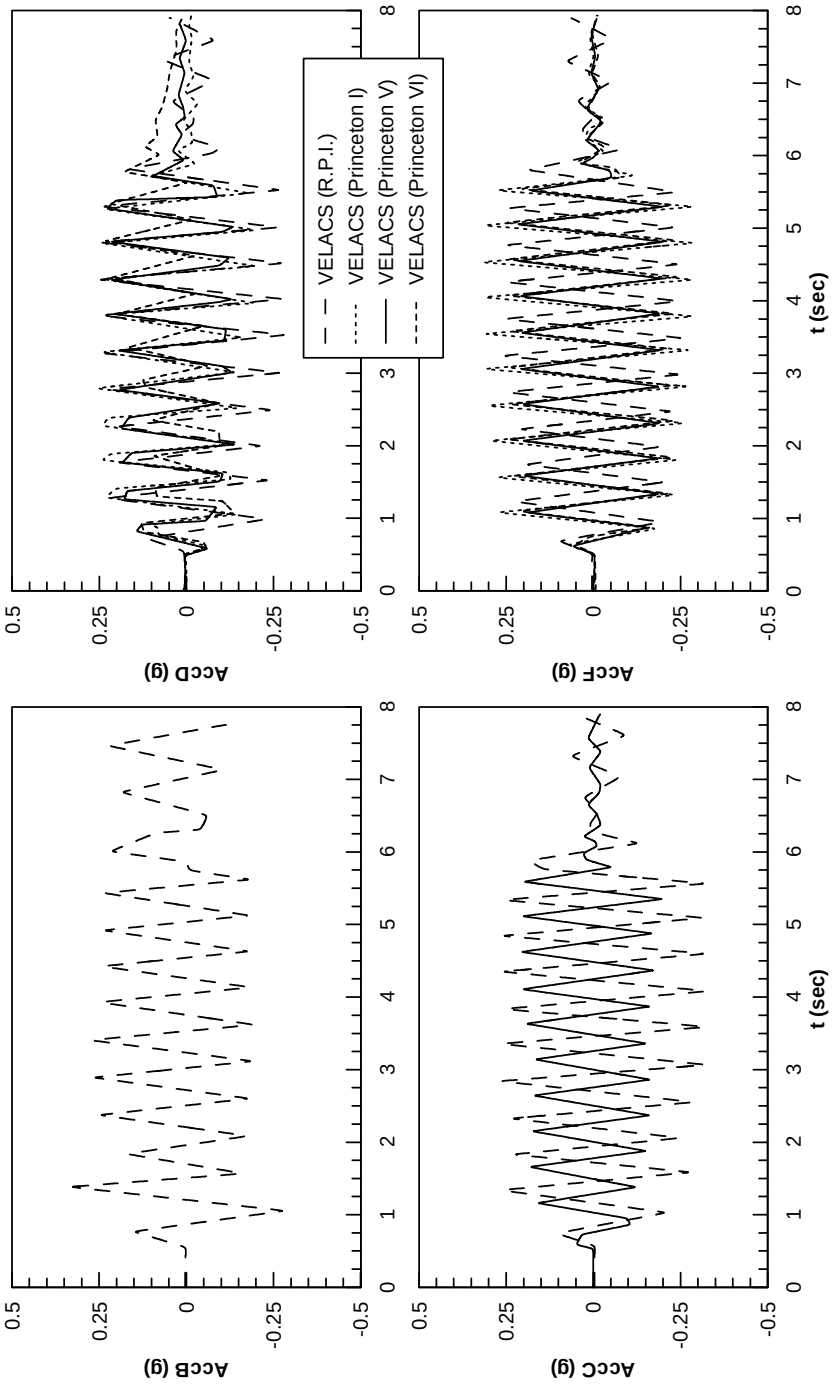
VELACS (R.P.I.)
VELACS (Princeton I)
VELACS (Princeton V)
VELACS (Princeton VI)
Acc D (g)
Acc F (g)
Acc B (g)
Acc C (g)
t (sec)
0.5
0.25
0
-0.25
-0.5
0
1
2
3
4
5
6
7
8

Figure 3.23. Recorded acceleration time histories.

Σχήμα 3.23. Καταγεγραμμένες χρονοϊστορίες επιταχύνσεων.

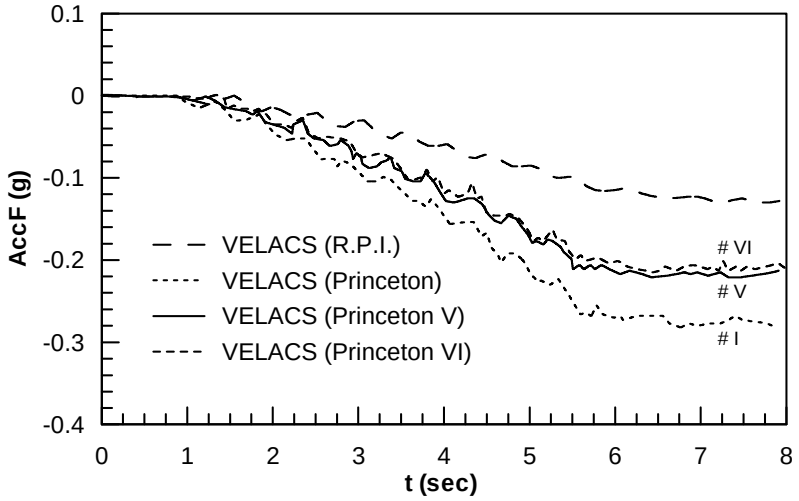

Figure 3.24. Recorded foundation settlement time histories.

Σχήμα 3.24. Καταγεγραμμένες χρονοϊστορίες καθιζήσεων θεμελίου.

3.5.2. Numerical Simulation

In order to assess the qualitative and quantitative accuracy of the developed numerical methodology, a total of three (3) numerical simulations were performed:

i. Initially, a 2-dimensional simulation was conducted, using the finite difference code FLAC. In this case, the square foundation is essentially replaced by a strip footing. Therefore, the structure's density was reduced, as described in the following, in order to convert the actual applied pressure into an equivalent 2-dimensional loading.

ii. Next, a similar analysis was performed, using the finite difference code FLAC3D. In this case, a single row of 1m wide elements was used and plane strain conditions were considered, in order to allow the comparison of the results with the 2-dimensional analysis, aiming to verify the correct implementation of the UDM in FLAC3D.

iii. The equivalent plane strain analyses were followed by a real 3-dimensional analysis. This analysis demonstrates the capabilities of the developed numerical methodology, as the full 3-dimensional problem may be accurately

simulated without any simplifications, regarding the equivalent applied pressure.

Figures 3.25 to 3.27 show the meshes used for each one of the above numerical simulations. In the first (2-dimensional) analysis, 482 zones and 541 gridpoints were used, with dimensions varying from 0.60m × 0.50m (width × height), in the region near the structure, to 0.75m × 0.75m away from the foundation. In the second (3-dimensional, equivalent plane strane) analysis, the number and the dimensions of zones in the problem's plane were the same as in the 2-dimensional analysis. A single row of 1m wide elements was used, while the total number of gridpoints was equal to 2×541=1082. Finally, in the third (complete 3-dimensional) analysis, the total number of zones reached 4680, corresponding to 5751 gridpoints. Within the plane of the applied excitation, the mesh was similar to the previous plane strain analyses. In the third dimension, only one half of the model was simulated, as the behavior is symmetrical. A total width of 10 zones was considered, with zone dimensions varying from 0.60m near the footing to 0.75m further away.

As it may be observed in Figures 3.25 to 3.27, the modeled footing width was considered equal to 4×0.60m=2.40m. According to Itasca (2005), the bearing area is found by assuming that vertical velocity developing as the footing settles varies linearly, from the value at the last gridpoint of the footing, to zero at the next gridpoint. Therefore, half the width of the adjascent elements should be added to the actual footing width, resulting to a total width of 2.40m+2*0.30m=3.00m. Of course, the applied pressure was appropriately adjusted.

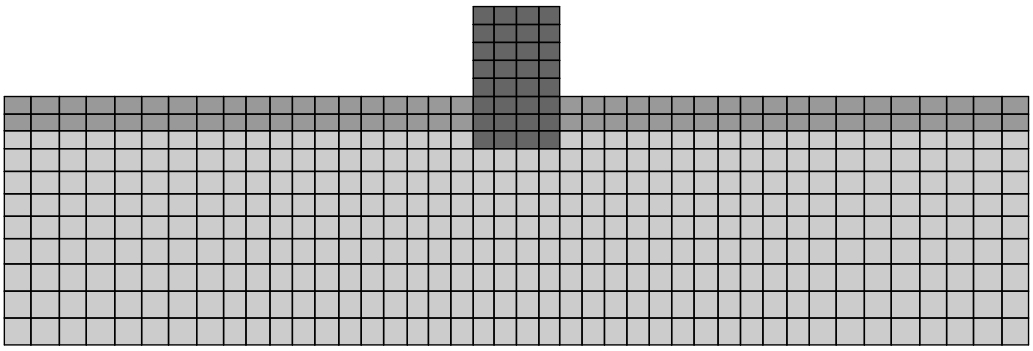

Figure 3.25. Mesh used in the 2-dimensional numerical simulation.

Σχήμα 3.25. Δίκτυο στοιχείων που χρησιμοποιήθηκε στη 2-διάστατη αριθμητική προσομοίωση.

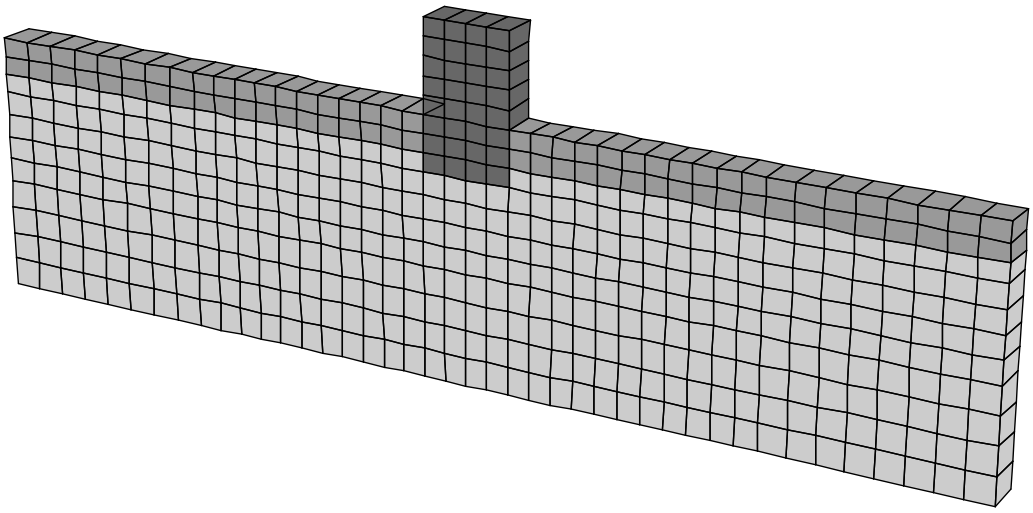

Figure 3.26. Mesh used in the 3-dimensional, equivalent plane strain numerical simulation.

Σχήμα 3.26. Δίκτυο στοιχείων που χρησιμοποιήθηκε στην 3-διάστατη αριθμητική προσομοίωση υπό συνθήκες επίπεδης παραμόρφωσης.

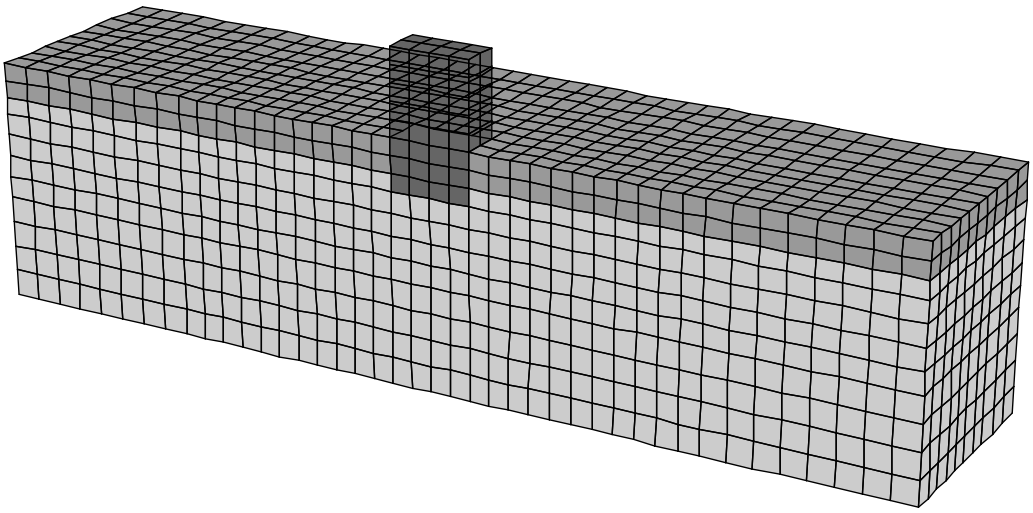

Figure 3.27. Mesh used in the complete 3-dimensional numerical simulation.

Σχήμα 3.27. Δίκτυο στοιχείων που χρησιμοποιήθηκε στην 3-διάστατη αριθμητική προσομοίωση.

As far as boundary conditions are concerned, only horizontal displacements were restrained in the lateral boundaries of the 2-dimensional analysis, while no restraint was considered in the vertical direction, in order to allow the development of settlements. In the 3-dimensional analysis, horizontal restraints refer to the directions vertical to the lateral boundaries' planes. During the initial static loading and the computation of initial stresses, only vertical restraints were applied in the bottom boundaries of all three numerical models. Horizontal displacements of the bottom

gridpoints were allowed to move horizontally, in order to avoid the development of parasitic shear stresses. Horizontal displacements of the bottom boundary were restrained during shaking, simulating rigid bedrock conditions.

In all three numerical analyses, the constitutive model presented in previous chapters was used to simulate sand behaviour. The parameters considered were the ones presented in the prevous paragraphs, corresponding to Nevada Sand, with an initial void ratio of $e = 0.661$, corresponding to a relative density of $D_r = 60\%$. Both the silt cap and the superstructure were simulated as elastic materials. More specifically, a shear modulus of $G = 5760\text{kPa}$ was considered for the silt layer. This value results from a maximum shear wave velocity of $V_s = 60\,\text{m/sec}$, and a shear modulus degradation of 20%, corresponding to cyclic shear strains of the order of 0.01%, for soils with a plasticity index of $PI = 15\%$ (Vucetic & Dobry, 1991). The elastic parameters of aluminium were considered for the superstructure, namely shear modulus equal to $G = 2.9 \cdot 10^6\,\text{kPa}$ and bulk modulus equal to $K = 3.9 \cdot 10^6\,\text{kPa}$.

Local nonviscous damping was considered for all materials. According to this form of damping, the damping force on a gridpoint is proportional to the magnitude of the unbalanced force, while its direction is such that energy is always dissipated. This formulation does not influence the mode of failure as it does not introduce body forces in flowing regions, while it allows for different amounts of damping to be defined for different regions. Most importantly, it does not require the performance of a complete modal analysis to compute the eigenvalues of the matrix, as it is independent of properties or boundary conditions, which also makes it appropriate for highly non-linear problems as the one addressed herein. A damping value of 2% was selected for the sand, corresponding to the minimum damping value reported by Vucetic & Dobry (1991), for very small cyclic shear strains (0.001%). For larger shear strain amplitudes, hysteretic damping will be simulated by the non-linear behavior of the model itself. A value of 10% was selected for the silt cap, corresponding to cyclic shear strains of the order of 0.01%, for soils with a plasticity index of $PI = 15\%$ (Vucetic & Dobry, 1991). Finally, 5% damping was used for the superstructure material.

As far as permeability is concerned, a value of $k = 2.1 \cdot 10^{-5}\,\text{m/sec}$ was used for Nevada Sand, that is 100 times larger than the actual value, for reasons of scaling to

prototype conditions. The corresponding values for the relatively impermeable silt and the superstructure were smaller, by 4 and 10 orders of magnitude respectively. In order to simulate the water table level, pore pressures and vertical stresses equal to 9.81kPa were applied to the ground surface, corresponding to 1m of water.

As mentioned in the previous paragraphs, in the first two plane strane analyses, the bearing pressure of the superstructure was reduced from the initial value of 150kPa into an equivalent strip foundation pressure of 95kPa. This value was suggested by Popescu & Prevost (1994), as the applied pressure that would produce the same elastic static settlements in plane strain conditions and in the full 3-dimensional problem. It is noted that in the third (3-dimensional) analysis there was no need to make such simplifications and the value of 150kPa was used directly.

In order to produce the initial stress state, the procedure followed during the preparation of the sample in the experiments was also followed in the numerical simulation. More specifically:

- The lowest 5.5m of the sand layer were first placed. Initial stresses were computed considering water level at 7m. In order to achieve this, the density of all elements corresponding to the higher 0.5m of the sand layer, the silt layer, and the submerged part of the superstructure, was set equal to water density ($\rho = 1.0\,\mathrm{Mgr/m^3}$), while pore pressures and vertical stresses were applied at the surface, as described above. The density of the part of the superstructure that is above water level was set to a small value of $\rho = 0.001\,\mathrm{Mgr/m^3}$.

- The structure was then added, by gradually increasing the density of the corresponding model zones.

- Consequently, the rest 0.5m of sand and the silt layer were added, also as a gradual increase of the density of the corresponding zones.

- Taking into account that the experiment was performed in a rigid box, the excitation was applied to both the bottom boundary of the model's mesh, as well as to the lateral boundaries, in the direction of shaking. The applied excitation time history is presented in Figure 3.28.

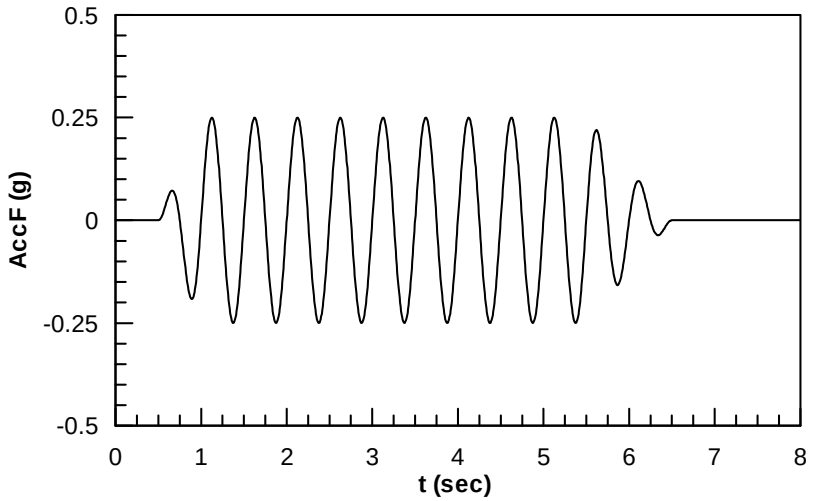

Figure 3.28. Applied acceleration time-history.

Σχήμα 3.28. Επιβαλόμενη χρονοϊστορία επιταχύνσεων.

Figures 3.29 to 3.31 quantify the results of the numerical analyses and compare them to experimental recordings, in terms of excess pore pressure ratios $\Delta u/\sigma'_{v,o}$, accelerations, and settlement timehistories, respectively. It may be observed that:

- The developed numerical methodology accurately predicts the evolution of excess pore pressure ratios, indicating higher ratios in the free filed than in the region underneath the footing. The effect of the superstructure on the underlying soil is therefore successfully quantified.
- The fact that there is no degradation of accelerations, due to the non-liquefaction of the subsoil, is also well predicted by the numerical methodology.
- Finally, predicted settlements match fairly well the ones recorded in the R.P.I. centruifuge, being smaller than the ones resulting from the Princeton centrifuge tests. It has been explained though, that results of the R.P.I. test showed higher repeatability and may be regarded as more reliable.

Furthermore, comparison between the rusults of the first (2-dimensional) and the second (3-dimensional plane-strain) analysis, indicates that the 2-D model has been correctly extended to three (3) dimensions and implemented into FLAC3D. Any small differences noticed in the results are attributed to differences in the numerical methodology, combined with the complexity and the high non-linearity of the

analyzed phenomenon. As described in the previous chapters, finite difference computations in FLAC are performed after the discretization of the quadrilateral zones into four (4) triangular subzones. On the other hand, the 8-noded zones of FLAC3D are divided into ten (10) tetrahedral subzones.

Finally, the results of the plane-strain analyses are well compared to the ones of the complete 3-dimensional analysis. It should be stressed though, that the full 3-dimensional analysis succeeds to provide accurate predictions without the necessity to make any simplifications regarding the foundation's bearing pressure.

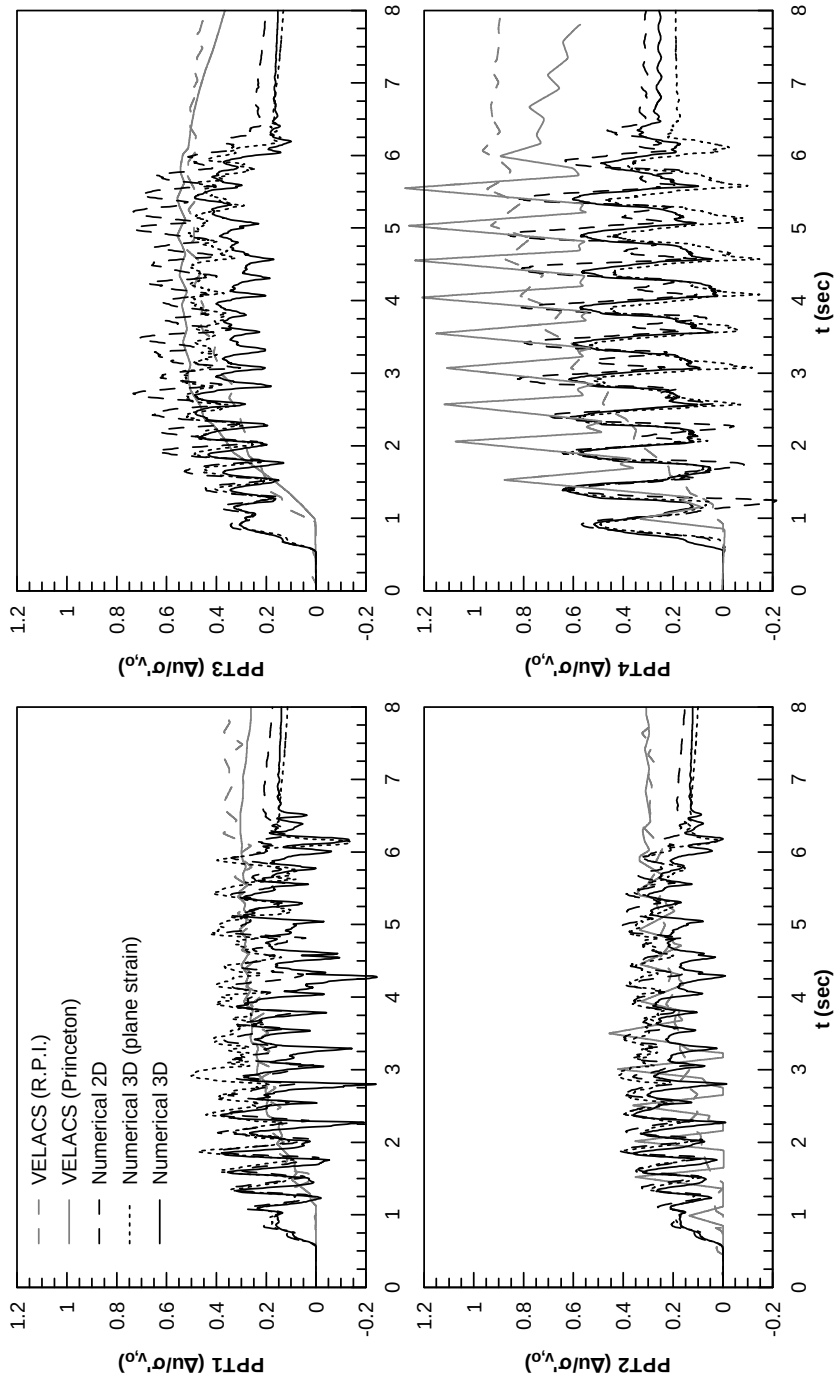

Figure 3.29. Comparison of experimental results and numerical predictions, in terms of excess pore pressure ratio timehistories.

Σχήμα 3.29. Σύγκριση πειραματικών αποτελεσμάτων και αριθμητικών προβλέψεων σε όρους χρονοϊστοριών λόγου υπερπιέσεων πόρων.

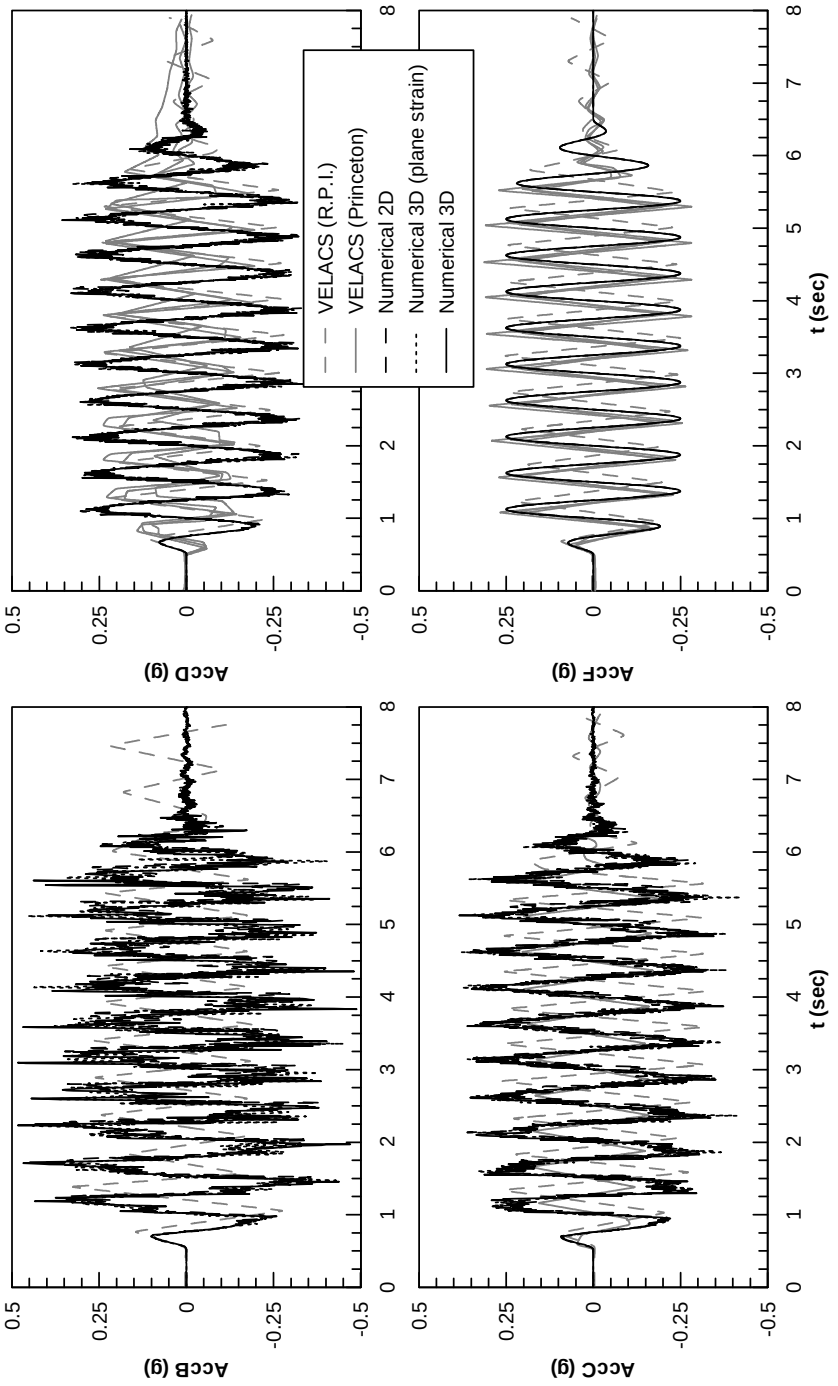

Figure 3.30. Comparison of experimental results and numerical predictions, in terms of acceleration timehistories.

Σχήμα 3.30. Σύγκριση πειραματικών αποτελεσμάτων και αριθμητικών προβλέψεων σε όρους χρονοϊστοριών επιταχύνσεων.

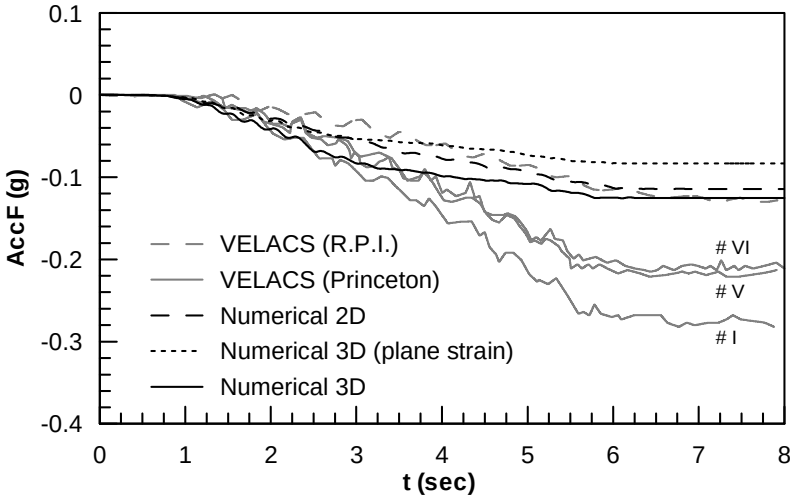

Figure 3.31. Comparison of experimental results and numerical predictions, in terms of foundation settlement timehistories.

Σχήμα 3.31. Σύγκριση πειραματικών αποτελεσμάτων και αριθμητικών προβλέψεων σε όρους χρονοϊστοριών καθιζήσεων θεμελίου.

References

Andrianopoulos, K. (2006): “Numerical simulation of static and dynamic loading on elastoplastic soils”, PhD Thesis, National Technical University of Athens, School of Civil Engineering, Geotechnical Department (in Greek).

Arulanandan, K., Scott, R.F. (1994): “Verification of numerical procedures for the analysis of soil liquefaction problems”, Proceedings of the International Conference on Verification of Numerical Procedures for the Analysis of Soil Liquefaction Problems, Davis, CA, 17-20 October, Vol. 1,2.

Arulmoli, K., Muraleetharan, K.K., Hossain, M.M., Fruth, L.S. (1992): “VELACS: Verification of Liquefaction Analyses by Centrifuge Studies; Laboratory Testing – Soil Data Report”, Research Report, The Earth Technology Corporation

Aubry, D., Hujeux, J.C., Lassoudiere, F., Meimon, Y. (1982): “Double memory model with multiple mechanisms for cyclic soil behaviour”, Proceedings of the International Symposium on Numerical Models.

Been, K., Jefferies, M.G. (1985): “State parameter for sands”, Geotechnique, 35 (2), pp. 99-112.

Bouckovalas, G., Marr, W.A., Christian, J.T. (1986): “Analyzing permanent drift due to cyclic loads”, Journal of Geotechnical Engineering, ASCE, 112 (6), pp. 579-593.

Bouckovalas, G., Whitman, R.V., Marr, W.A. (1984): “Permanent displacement of sand with cyclic loading”, Journal of Geotechnical Engineering, ASCE, 110 (11), pp. 1606-1623.

Byrne, P.M. (1991): “A model for predicting liquefaction induced displacement”, Proceedings of the Second International Conference on Recent Advances in Geotechnical Earthquake Engineering and Soil Dynamics.

Byrne, P.M., Beaty, M. (1998): “An Effective Stress Model for Predicting Liquefaction Behaviour”, Geotechnical Special Publication.

Elgamal, A., Yang, Z., Parra, E., Ragheb, A. (2003): “Modeling of cyclic mobility in saturated cohesionless soils”, International Journal of Plasticity, 19 (6), pp. 883-905.

Hardin, B.O. (1978): “Nature of stress-strain behavior for soils”, v (1), pp. 3-90.

Ishibashi, I., Zhang, X. (1993): “Unified dynamic shear moduli and damping ratios of sand and clay”, Soils and Foundations, 33 (1), pp. 182-191.

Ishihara, K., Tatsuoka, F., Yasuda, S. (1975): “Undrained deformation and liquefaction of sand under cyclic stresses”, Soils and Foundations, 15 (1), pp. 29-44.

Iwan, W.D., Yoder, P.J. (1983): “Computational aspects of strain-space plasticity”, Journal of Engineering Mechanics, 109 (1), pp. 231-243.

Kramer, S.L. (1996): “Geotechnical earthquake engineering”, Prentice-Hall.

Krieg, R.D., Krieg, D.B. (1977): “Accuracies of numerical solution methods for the elastic-perfectly plastic model”, Journal of Pressure Vessel Technology, Transactions of the ASME, 99 Ser J (4), pp. 510-515.

Ladd, C.C., Foott, R., Ishihara, K., Schlosser, F., Poulos, H.G. (1977): “Stress-deformation and strength characteristics”, Proceedings of the Ninth International Conference on Soil Mechanics and Foundation Engineering, 2, pp. 421-494.

Marti, J., Cundall, P. (1982): “Mixed discretization procedure for accurate modelling of plastic collapse”, International Journal for Numerical and Analytical Methods in Geomechanics, 6 (1), pp. 129-139.

Nemat-Nasser, S., Tobita, Y. (1982): “Influence of fabric on liquefaction and densification potential of cohesionless sand”, Mechanics of Materials, 1 (1), pp. 43-62.

Ortiz, M., Popov, E.P. (1985): “Accuracy and stability of integration algorithms for elastoplastic constitutive relations”, International Journal for Numerical Methods in Engineering, 21 (9), pp. 1561-1576.

Ortiz, M., Simo, J.C. (1986): “Analysis of a new class of integration algorithms for elastoplastic constitutive relations”, International Journal for Numerical Methods in Engineering, 23 (3), pp. 353-366.

Papadimitriou, A. (1999): “Elastoplastic simulation of the monotonic and cyclic behaviour of soils”, PhD Thesis, National Technical University of Athens, School of Civil Engineering, Geotechnical Department (in Greek).

Papadimitriou, A.G., Bouckovalas, G.D. (2002): “Plasticity model for sand under small and large cyclic strains: a multiaxial formulation”, Soil Dynamics and Earthquake Engineering, 22 (3), pp. 191-204.

Papadimitriou, A.G., Bouckovalas, G.D., Dafalias, Y.F. (2001): “Plasticity model for sand under small and large cyclic strains”, Journal of Geotechnical and Geoenvironmental Engineering, 127 (11), pp. 973-983.

Popescu, R., Prevost, J.H. (1993): “Centrifuge validation of a numerical model for dynamic soil liquefaction”, Soil Dynamics & Earthquake Engineering, 12 (2), pp. 73-90.

Popescu, R., Prevost, J.H (1994): “Numerical class A predictions for Models No 1, 2, 3, 4a, 4b, 6, 7, 11 & 12”, Proceedings of the International Conference on Verification of Numerical Procedures for the Analysis of Soil Liquefaction Problems, Davis, CA, 17-20 October, Vol. 1, pp. 1105-1207.

Popescu, R., Prevost, J.H. (1995): “Comparison between VELACS numerical "class A' predictions and centrifuge experimental soil test results”, Soil Dynamics & Earthquake Engineering, 14 (2), pp. 79-92.

Prevost, Jean H. (1985): “Simple plasticity theory for frictional cohesionless soils”, Soil Dynamics and Earthquake Engineering, 4 (1), pp. 9-17.

Ramberg, W., Osgood, W.R. (1943): “Description of stress-strain curves by three parameters”

Schofield, A.N., Wroth C.P. (1968): “Critical state soil mechanics”, London: McGraw Hill

Schreyer, H.L., Kulak, R.F., Kramer, J.M. (1979): “Accurate numerical solutions for elastic-plastic models”, Journal of Pressure Vessel Technology, Transactions of the ASME, 101 (3), pp. 226-234.

Seed, H.Bolton, Booker, John R. (1977): “Stabilization of potentially liquefiable sand deposits”, Journal of Geotechnical Engineering, ASCE, 103 (7), pp. 757-768.

Simo, J.C., Taylor, R.L. (1986): “Return mapping algorithm for plane stress elastoplasticity”, International Journal for Numerical Methods in Engineering, 22 (3), pp. 649-670.

Sloan, S.W., Abbo, A.J., Sheng, D. (2001): “Refined explicit integration of elastoplastic models with automatic error control”, Engineering Computations (Swansea, Wales), 18 (1-2), pp. 121-154.

Vucetic, M., Dobry, R. (1991): “Effect of soil plasticity on cyclic response”, Journal of geotechnical engineering, 117 (1), pp. 89-107.

Yang, Z., Elgamal, A., Parra, E. (2003): “Computational model for cyclic mobility and associated shear deformation”, Journal of Geotechnical and Geoenvironmental Engineering, 129 (12), pp. 1119-1127.

Youd, T.L., Idriss, I.M., Andrus, R.D., Arango, I., Castro, G., Christian, J.T., Dobry, R., Liam Finn, W.D., Harder L.F., Jr., Hynes, M.E., Ishihara, K., Koester, J.P., Liao, S.S.C., Marcuson III, W.F., Martin, G.R., Mitchell, J.K., Moriwaki, Y., Power, M.S., Robertson, P.K., Seed, R.B., Stokoe II, K.H. (2001): “Liquefaction resistance of soils: Summary report from the 1996 NCEER and 1998 NCEER/NSF workshops on evaluation of liquefaction resistance of soils”, Journal of Geotechnical and Geoenvironmental Engineering, 127 (10), pp. 817-833.